DIGITAL ACCESS TO SCHOLARSHIP AT HARVARD
DASH.HARVARD.EDU

HARVARD LIBRARY
Office for Scholarly Communication

Electrode-Electrolyte Interfaces in Solid Polymer Lithium Batteries

Citation
Hu, Qichao. 2012. Electrode-Electrolyte Interfaces in Solid Polymer Lithium Batteries. Doctoral dissertation, Harvard University.

Permanent link
http://nrs.harvard.edu/urn-3:HUL.InstRepos:9637868

Terms of Use
This article was downloaded from Harvard University's DASH repository, and is made available under the terms and conditions applicable to Other Posted Material, as set forth at http://nrs.harvard.edu/urn-3:HUL.InstRepos:dash.current.terms-of-use#LAA

Share Your Story

The Harvard community has made this article openly available.
Please share how this access benefits you. Submit a story .

Accessibility

© 2012 – Qichao Hu
All rights reserved.

Electrode-Electrolyte Interfaces in Solid Polymer Lithium Batteries

by

Qichao Hu

Submitted to Harvard School of Engineering and Applied Sciences
On May 1st, 2012 in partial fulfillment of the
Requirements for the Degree of Doctor of Philosophy in Applied Physics

Abstract

This thesis studies the performance of solid polymer lithium batteries from room temperature to elevated temperatures using mainly electrochemical techniques, with emphasis on the bulk properties of the polymer electrolyte and the electrode-electrolyte interfaces.

Its contributions include: 1) Demonstrated the relationship between polymer segmental motion and ionic conductivity indeed has a Vogel-Tammann-Fulcher (VTF) dependence, and improved the conductivity of the graft copolymer electrolyte (GCE) by almost an order of magnitude by changing the ion-conducting block from poly(oxyethylene) methacrylate (POEM) to a block with a lower glass transition temperature (T_g) poly(oxyethylene) acrylate (POEA). 2) Identified the rate-limiting step in the battery occurs at the cathode-electrolyte interface using both full cell and symmetric cell electrochemical impedance spectroscopy (EIS), improved the battery rate capability by using the GCE as both the electrolyte and the cathode binder to reduce the resistance at the cathode-electrolyte interface, and used TEM and SEM to visualize the polymer-particle interface (full cells with $LiFePO_4$ as the cathode active material and lithium metal as the anode were assembled and tested). 3) Applied the

solid polymer battery to oil and gas drilling application, performed high temperature (up to 210 °C) cycling (both isothermal and thermal cycling), and demonstrated for the first time, current exchange between a solid polymer electrolyte and a liquid lithium metal. Both the cell open-circuit-voltage (OCV) and the overall GCE mass remained stable up to 200 °C, suggesting that the GCE is electrochemically and gravimetrically stable at high temperatures. Used full cell EIS to study the behavior of the various battery parameters as a function of cycling and temperature. 4) Identified the thermal instability of the cell was due to the reactivity of lithium metal and its passivation film at high temperatures, and used Li/GCE/Li symmetric cell EIS to study the thermal stability of the anode-electrolyte interface, which was responsible for the fast capacity fade observed at high temperatures. 5) Proposed a new electrolyte material and a new battery design called polymer ionic liquid (PIL) battery that can dramatically improve the safety, energy density, and rate capability of rechargeable lithium batteries.

Acknowledgement:

I entered graduate school an ambitious but confused individual. After countless defeats and frustrations, I began to crystallize. I don't remember the exact date, but it was in the spring of 2011, a few days after the ice on the Charles River had melted, when all of a sudden, the path became crystal clear to me.

First, I want to thank my thesis advisor Prof. Donald Sadoway for giving me the opportunity and tolerating me until now. He provided me the freedom to work and think independently, and the mentoring to guide me in the right direction. When I was getting lost in the jungle of lithium battery research, he encouraged me to think differently. I am also grateful for his support and encouragement when I wanted to commercialize the solid polymer lithium battery technology.

I want to thank the other members of GroupSadoway, especially Dr. Luis Ortiz, Dr. Antonio Caputo, Dr. Sebastian Osswald, Dr. Xuhui Mao, Dr. Weifeng Wei, Dr. Lee Moshurchak, Dr. Gangqin Shao, and Hilary Sheldon for their patience and support.

I want to thank Prof. Michael Aziz, Prof. Shriram Ramanathan, and Susan Wieczorek at Harvard School of Engineering and Applied Sciences for their guidance and for allowing me to cross-register at MIT. Whatever I become in the future, I promise to never forget the Harvard Alumni Association.

I want to thank the MIT entrepreneurs' community, especially the Sloan Energy Ventures class, the Trust Center, and the Venture Mentoring Service for their guidance through the tumultuous days of starting my company.

I want to thank Weatherford International for their generous financial support. It not only allowed me to finish my PhD and exposed me to exciting new opportunities in the energy industry, it restored confidence and hope to me and my project.

Finally, I want to thank my parents for their unyielding love in the past 26 years.

"I didn't see it then, but it turned out that getting fired from Apple was the best thing that could have ever happened to me. The heaviness of being successful was replaced by the lightness of being a beginner again, less sure about everything. It freed me to enter one of the most creative periods of my life."

-Steve Jobs
2005 Stanford Commencement Address

Table of Contents

List of Figures

Executive Summary

Batteries are bombs. The bigger the battery, the more powerful the explosion. Across the board, as the need for energy storage becomes greater, and the size of battery becomes bigger, battery safety is a ticking time bomb that causes property damage, reduces revenues, and even costs human lives.

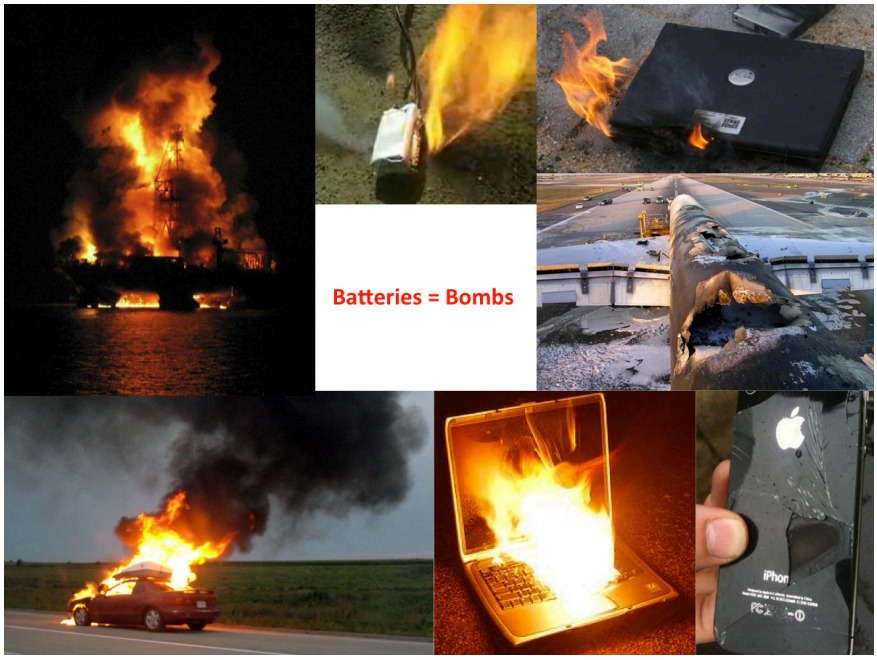

Figure ES.1 Examples of exploding batteries

Already, battery-related failures have led to exploding laptops, glowing iPhones, plane crashes, and the BP oil spill. As we move towards electric vehicles, are exploding cars next? In certain applications such as electric vehicles and grid storage, the safety risk can be reduced but not eliminated with expensive and bulky cooling systems. The recent report of Chevy Volt fires demonstrated this point all too well. But in other applications such as consumer electronics and oil drilling, where a cooling system is not an option, the only thing preventing an explosion is very often just luck.

In addition, battery safety concerns prevent the use of the most efficient and highest energy density materials in lithium batteries; for example, lithium metal, which has the highest storage capacity of any material that can serve as the negative electrode, is not used in today's rechargeable lithium-ion batteries because of safety risks. Our solid polymer lithium battery can potential hit two birds with one stone, by dramatically improving both the *safety* and *energy density* of rechargeable lithium batteries.

The vast majority of research in the lithium battery community focuses on the cathode, and there have been many materials developed over the years (shown in Figure ES.2). This is a fast-paced but short-lived environment, where new cathode materials are quickly eclipsed by newer materials with incrementally higher energy density. Our work focuses on the electrolyte, the lithium anode, and the anode-electrolyte interface (green checks in Figure ES.2). All are fundamental to a battery's *safety* and *energy density*.

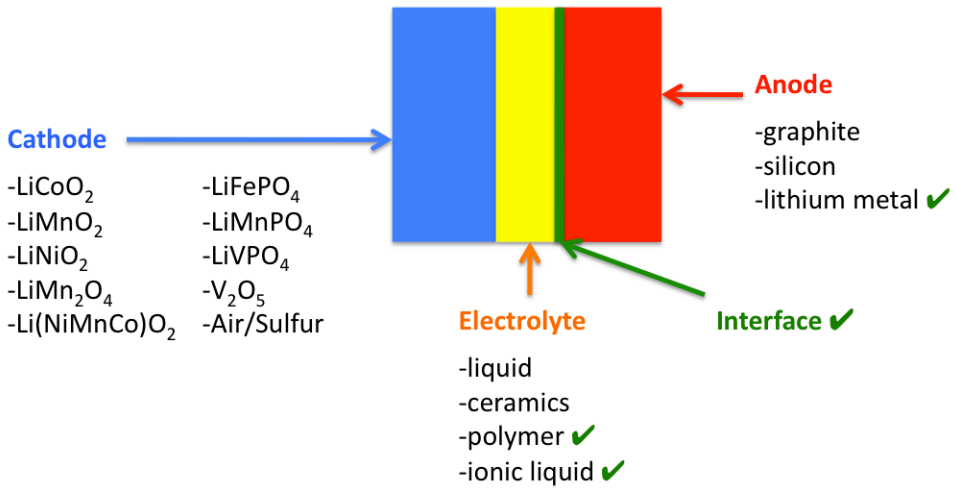

Figure ES.2 Areas of research interest in lithium batteries

The unique properties of lithium and the increasing global demand for energy storage mean that lithium batteries are here to stay. Also the need for higher energy densities suggests that future lithium batteries will use lithium metal as the anode providing that the safety issue can be properly addressed. Focusing on the electrolyte and the anode confers generality to our work, first, because we can benefit from advances in cathode materials, and second, be a key enabler not just for the solid polymer lithium battery but emerging technologies such as the lithium air battery, which has 100 times higher energy density that today's lithium-ion [1].

1. State of Lithium-ion Batteries

Lithium-ion batteries deserve a special place in the world of electrochemical systems. Their high volumetric and gravimetric energy densities have already made them ubiquitous in consumer electronics and portable power tools for decades. And now with the ongoing global effort to electrify vehicles in order to reduce greenhouse gas emission and dependence on foreign oil, lithium-ion batteries are again the batteries of choice. They are also being used in large-scale grid storage for load leveling, especially when the electricity comes from intermittent renewable sources. Lithium-ion batteries will play a key role in future urban designs where transportation and the grid are integrated into one (Figure 1.1).

Figure 1.1 Applications of lithium-ion batteries

The potential battery markets for electric vehicles and grid storages are orders of magnitude larger than for consumer electronics. Lithium-ion batteries won the fight in consumer electronics, and now have entered the broader energy

storage arena. Will Li-ion be able to compete with fossil fuels that have 100 times the energy density and are backed by companies with multi hundred billion dollar annual profits, and engine technologies that took a century to perfect? Lithium-ion batteries, first invented to power small gadgets, now have much bigger shoes to fill.

1.1 Overview of Electrode Development

Lithium is both the most electropositive metal (−3.04 V relative to standard hydrogen electrode), and the lightest metal (equivalent weight of 6.94 g/mol, and specific gravity of 0.53 g/cm^3). This makes it attractive as a choice for the active material in the negative electrode, and ideal for portable energy storage devices where size and weight matter. Figure 1.2 shows that lithium-based batteries (Li ion, Polymer Li on or PLiON, and Li metal) have higher energy densities than lead-acid, nickel-cadmium and nickel-metal-hydride batteries [2].

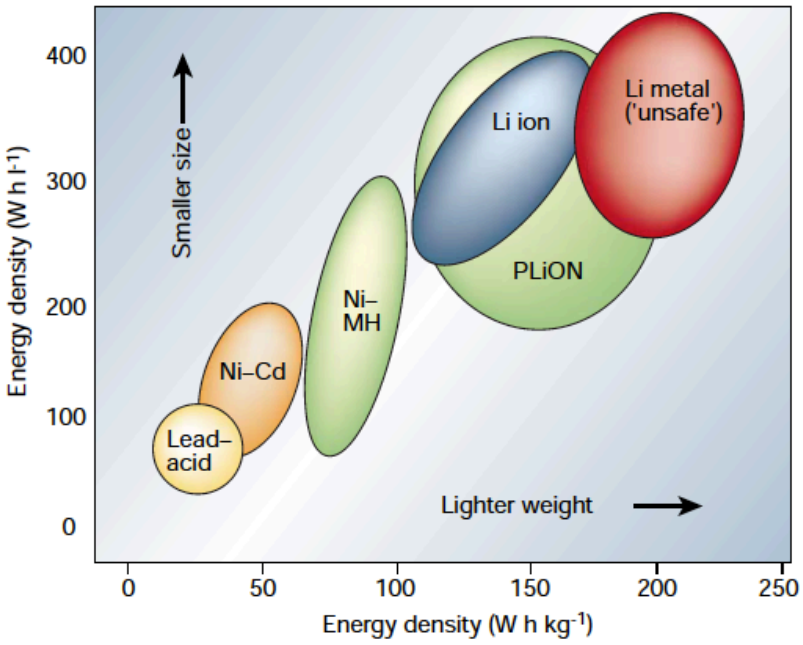

Figure 1.2 Energy densities for various batteries [2]

A full lithium-ion cell consists of a cathode (positive), an anode (negative), an electrolyte, and a separator (Figure 1.3). Both the cathode and the anode are intercalation compounds, where lithium-ions can intercalate or deintercalate reversibly (if the anode is carbon, lithium intercalates as neutral Li). The electrolyte provides ionic conduction and insulates electronic conduction between the electrodes. The separator is permeable to ions but mechanically rigid to keep the two electrodes from shorting. When the cell is in fully charged state, all of the lithium has intercalated in the anode, and when the cell is in fully discharged state, all of the lithium-ions are intercalated in the cathode. On the spontaneous reaction, or discharging, electrons flow from the anode to the cathode through an external circuit to power a device, while the ions flow from the anode to the cathode through the electrolyte. The ions and electrons recombine at the cathode to maintain charge neutrality. On charging the flows are reversed.

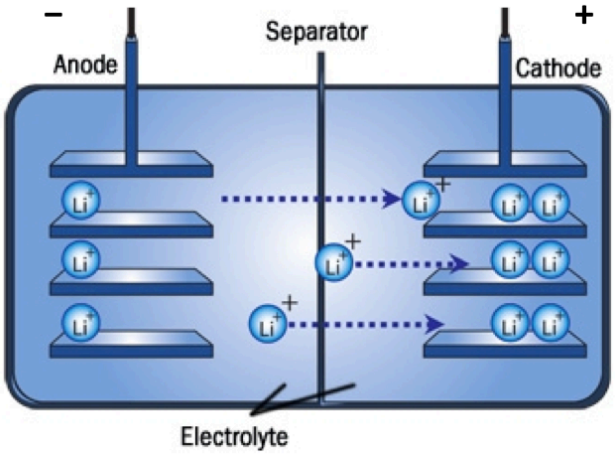

Figure 1.3 A full lithium-ion cell during discharging

Stanley Whittingham developed the world's first rechargeable half-lithium-ion battery in 1972 while working for Exxon Research and Engineering Company.

He used titanium disulfide (TiS_2) as the cathode (a very well studied intercalation compound at the time), lithium metal as the anode, and lithium perchlorate dissolved in dioxolane as the electrolyte. Although it was only a half-lithium-ion battery (intercalation only occurring in one electrode), it was an improvement in safety, cycling and rechargeability compared to early lithium-based primary batteries. Several other sulfides and chalcogenides were also studied as cathode intercalants, but they all had a low cell voltage of less than 2.5 V versus metallic lithium [2-7].

The issue with using lithium metal in liquid electrolyte is uneven dendrite growth on lithium metal during charging, where lithium is electrodeposited from the electrolyte. The organic carbonate liquid electrolyte also reacts exothermically with lithium metal to form layers on the anode surface. This leads to short circuit dendrites and explosion under an exothermic reaction. This problem increases upon cycling due to an increase in the surface area and morphological instability.

One solution to this safety problem is to replace lithium metal with an intercalation compound. The reversible intercalation of lithium into graphite anode (LiC_6) was developed at Bell Labs in the 1980s. The surface area and morphology of graphite do not change substantially during repeated charging, thus making it safer compared to a lithium metal anode [8, 9].

The shortcoming of graphite is its low lithium-ion storage capacity, only 380 mAh/g, compared to 3,800 mAh/g for lithium metal. The tradeoff between capacity and safety motivated the search for high-capacity intercalation compounds such as Sn (1,000 mAh/g) and Si (3,000 mAh/g) for the anode. However, large volume

change upon lithium-ion intercalaction and deintercalation causes the particles of Sn and Si to facture, lose electrical contact with the current collector, and result in poor cycle life. In 2008, Yi Cui's lab at Stanford demonstrated that using silicon nanowires ($Li_{4.4}Si$) could provide facile strain relaxation and short diffusion length, maintain electrical contact, and prevent electrode pulverization [10-16].

In parallel to the anode development, there has also been significant advancement in higher voltage, higher capacity, safer, and cheaper cathode materials. The focus shifted from metal disulfides to metal oxides because the M-O bonds are more ionic than the M-S bonds, thus making them more oxidizing (higher potential). In 1979, John Goodenough demonstrated a 4 V battery using $LiCoO_2$ as the cathode and lithium metal as the anode. $LiCoO_2$ has an average potential of 3.6 V relative to Li/Li^+ in carbon, and a specific capacity of 140 mAh/g, giving it an energy density of about 0.5 kWh/kg [17].

In 1985, Akira Yoshino demonstrated a battery using $LiCoO_2$ as the cathode and a carbon-based anode. This was the world's first full lithium-ion battery or the "rocking-chair" battery, where an intercalation compound was used for both electrodes and lithium only exists in its ionic form instead of metallic form (Recently, it has been found while lithium intercalates into the positive electrode as lithium-ion, and the compensating electron goes to the transition metal in the host; lithium intercalates into graphite negative electrode as neutral lithium, the bonding in LiC_6 is partially covalent rather ionic, and the charge transfer occurs at the electrode-electrolyte interface) [18]. This dramatically improved the safety of the battery. Subsequently in 1991, Sony released the first commercial full lithium-ion

battery, and the $LiCoO_2$/graphite combination is still found in most consumer electronic devices today.

In addition to $LiCoO_2$, other layered oxide compounds including $LiNiO_2$, $LiMnO_2$, and the recent $Li(Ni_{1/3}Mn_{1/3}Co_{1/3})O_2$ (NMC) have also been studied. NMC has one of the highest energy densities (4.2 V, 220 mAh/g, and almost 1 kWh/kg), and is used in high-energy and high-power applications such as electric vehicles today [6, 19-22].

In 1997, John Goodenough and Akshaya Padhi [23]demonstrated the olivine $LiFePO_4$ and other lithium transition-metal phosphates, including vanadium, as possible cathode materials. $LiFePO_4$ has a voltage of 3.3 V, a specific capacity of 150 mAh/g, and an energy density of 0.5 kWh/kg, comparable to $LiCoO_2$. The PO_4 structure is more stable than the MO_2 at high temperatures, reducing the likelihood of oxygen-evolution and improving safety. Also iron is cheaper, more earth-abundant and environmentally friendly than cobalt, nickel, or manganese. But the major drawback was the poor electronic conductivity of $LiFePO_4$ (10^{-9} S/cm), making it unrealistic for a practical battery.

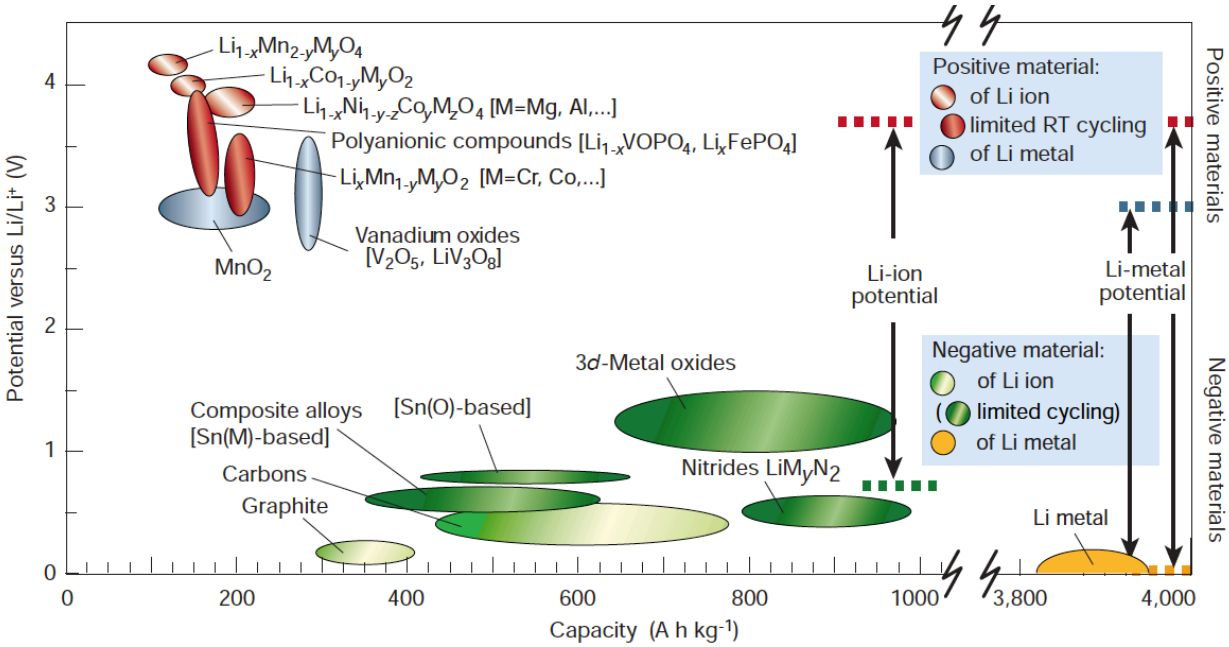

Figure 1.4 Energy densities of various cathode and anode materials [2]

In the early 2000s, Yet-Ming Chiang of MIT demonstrated that the electronic conductivity of $LiFePO_4$ could be improved by a factor of almost 10^8 through a combination of supervalent cation doping, carbon coating and nano-sized particles [24-27]. The voltages and capacities for various electrode materials are listed in Figure 1.4.

1.2 Overview of Electrolyte Development

Most of lithium-ion battery development focuses on the electrodes, because they determine the energy density of the battery, rather than on the electrolyte, which has remained mostly the same for decades. But the electrolyte is a key piece of the battery, as it affects the overall power capability, due to impedance both through the electrolyte itself and at the electrode-electrolyte interfaces.

The electrolyte used in lithium-ion batteries generally consists of a salt of the type LiX, and a non-aqueous solvent. Compared to the aqueous electrolytes used in other electrochemical systems, the disadvantages of Li-ion electrolytes are lower conductivity, higher cost, flammability, and environmental problems, but their advantages include wide temperature range (over which the electrolyte remains a liquid) from −150 °C to 300 °C, wide voltage window (up to 5 V versus Li/Li^+), and better compatibility with electrodes (aqueous electrolyte would react violently with lithium metal and form LiOH and hydrogen) [4, 7, 28-30].

The main non-aqueous electrolytes include organic carbonate-based liquid, polymer, ionic liquid, and ceramics. These electrolytes need to meet certain benchmarks to be used in practical lithium-ion batteries. They include a conductivity of at least 10 mS/cm, large electrochemical window (> 4.5 V for high voltage cathodes), low vapor pressure, good thermal and chemical stability, low toxicity and cost, and for certain stringent applications such as the electric vehicles, all of these benchmarks must be met over a wide temperature range, typically from −20 °C to 60 °C. Different applications have different temperature requirements on the electrolyte (Figure 1.5).

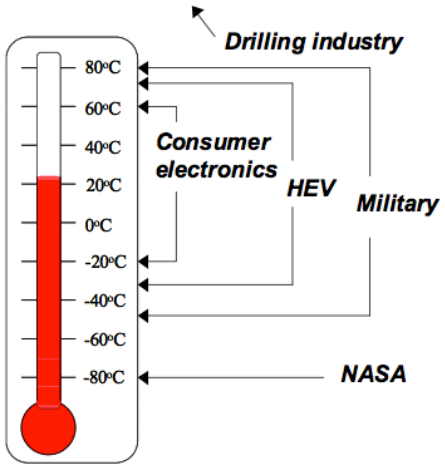

Figure 1.5 Temperature range for various applications

1.2.1 Carbonate-Based Liquid

Most electrolytes consist of a lithium salt dissolved in an organic carbonate-based solvent. However, it is difficult for any one solvent to meet all of the requirements. For example, solvents with low vapor pressure, such as ethylene carbonate (EC) and propylene carbonate (PC), tend to have higher viscosities, leading to lower conductivity. Also EC is a solid at room temperature; this requires it to be combined with another solvent. Generally the electrolyte is a combination of several solvents. The commons solvents and some of their physical properties are listed in Table 1.

Name	Melting T (°C)	Boiling T (°C)	Viscosity (mPa*s)
Dimethyl carbonate (DMC)	4.6	90	0.5902 (25 °C)
Diethyl carbonate (DEC)	−43	126.8	0.7529 (25 °C)
Ethylene carbonate (EC)	36.5	238	1.9 (40 °C)
Propylene carbonate (PC)	−54.53	242	2.512 (25 °C)

Table 1 Common carbonate solvents [6]

The common lithium salts include lithium hexafluorophosphate ($LiPF_6$), lithium bisoxalatoborate (LiBOB), and lithium bistrifluoromethane sulfonimide ($LiN(CF_3SO_2)_2$) or LiTFSI. $LiPF_6$ is the most widely used salt in commercial lithium-ion batteries. It has a conductivity of 10 mS/cm in a 1 M solution of EC and DMC at room temperature. But its disadvantage is its thermal stability; decomposition starts at 50 °C and increases dramatically from 70 °C to 130 °C. In comparison, LiBOB has a slightly lower conductivity of 8 mS/cm in the same solvent. But it is thermally stable up to 300 °C. It is also capable of forming stable passivation layer on aluminum, which is used as the current collector, and on graphite anodes, inhibiting exfoliation of the intercalant material by the solvent. This improves the cycling stability of the overall battery. LiTFSI is a new promising salt. It has conductivity comparable to that of $LiPF_6$, good thermal stability up to 250 °C, and forms stable passivation layer on graphite and lithium metal. These salts are also extremely sensitive to the presence of impurities such as water. The presence of water decreases cycling efficiency and increases capacity fade; it can also react with lithium metal and release hydrogen gas [31].

The electrolyte needs to be stable at both the anodic (0 V vs. Li) and cathodic (typically > 4.2 V vs. Li) potentials in a lithium-ion battery. However, none of these carbonate solvents is thermodynamically stable with lithium at 0 V vs. Li. Both the solvent and the salt participate in reactions to form a passivation layer on the anode surface. This passivation layer is ionically conductive, but spatially separating the electrolyte from the anode. In the case of a graphite anode, this passivation layer is also referred to as the Solid Electrolyte Interphase (SEI) [32-34]. A stable

passivation layer imparts stability to the battery, and allows it to be recharged thousands of cycles and to have many years of shelf life. However, the formation of this passivation layer consumes lithium, and the process is irreversible. This is shown as a loss of capacity typically in the first cycle. In addition to the salt choice, alkyl and esters carbonate solvents such as EC and EMC have been shown to form a stable passivation layer with minimum capacity loss [35-42].

In addition to the solvent and salt, a small amount (< 10%) of additives is also added to the electrolyte. Additives help improve the performance at extreme temperatures, forming a stable passivation layer, and reducing the irreversible capacity. One common additive in commercial lithium-ion battery electrolyte is vinylene carbonate (VC).

1.2.2 Ionic Liquids

The other class of liquid electrolyte is ionic liquids, which are molten salts with melting temperature lower than 100 °C. Among them, some have melting temperature even below room temperature, hence referred to as room temperature ionic liquids (RTIL). RTILs are a promising candidate for lithium-ion batteries, because they have low vapor pressure (nonflammable and nonvolatile), have high thermal stability (typically above 250 °C), and have good room temperature conductivity (ranging form 0.1 to 18 mS/cm). RTILs are more viscous than the carbonate solvents, with viscosities ranging from 10 to 50 mPa*s, leading to poor wetting with the electrodes [43-49].

The melting temperature of a salt is related to its lattice energy. The easier it is for thermal energy to overcome the lattice energy, the lower the melting temperature. The cations in RTILs typically have large organic structural groups, and low electrical charges. Also both the cations and anions tend to be bulky and have asymmetrical shapes, leading to poor crystallization, which also reduces the melting temperature. The common RTILs have anions including $(F_3CSO_2)_2N^-$, $F_3CSO_3^-$, BF_4^-, $AlCl_4^-$, and PF_6^-, and cations including butyl-methyl-pyrrolidinium and ethyl-methyl-imidazolium.

The size of the cations, mainly the alkyl chain length, greatly affects the physical chemical properties of the RTILs. Bigger cations with long alkyl chains have higher viscosity and lower conductivity. The addition of lithium salt also decreases the conductivity. One challenge for RTILs is anode compatibility. Most RTILs are reduced at potential higher than 0 V versus lithium deposition or intercalation. This makes the anode passivation film unstable, and greatly reduces the cycling efficiency and cycle life of the battery. It was recently shown that by combining methyl-butyl-pyrrolidinium (PYR_{14}), bis(trifluoromethane sulfonyl)imide (TFSI), and poly(ethylene glycol) dimethyl ether (PEGDME), the electrochemical widow, viscosity and conductivity can be tuned [49, 50].

1.2.3 Solid Inorganic (Ceramics and Glass)

Ionic transport can also occur in solids due to atomic disorder in crystal structures. Both vacancy and interstitial defects are present in large numbers in solid ion conductors. The conductivity is inversely related to the activation enthalpy of the ionic interaction between the lattice and the mobile ions, and the mobility is correlated to the ionic radius. The conductivity reaches maximum for the optimum ion size, which is neither too small nor too big for the transport pathways. Multivalent ions, which carry larger charge, have lower conductivities, because they have higher activation enthalpy.

Most solid ion conductors were developed for monovalent ions, such as lithium, sodium and potassium. For sodium and potassium, they include NASICON (10 mS/cm) and β-alumina (100 mS/cm to 1 S/cm), both have very high conductivity at room temperature, and are thermally stable above 200 °C. For lithium, the most studied is lithium phosphorus oxynitride (LiPON). LiPON has a room temperature conductivity of 10^{-6} S/cm, which is about 40 times higher than the nitrogen-free Li_3PO_4, a unity lithium cation transference number, an electrochemical window of more than 5 V versus Li/Li^+, and is stable at elevated temperatures and with lithium metal. Another solid electrolyte is Li_3N, which has the highest room temperature conductivity (6 mS/cm), but a low cathodic decomposition potential preventing it from being used with high-voltage cathodes. Other solid conductors such as thio-LISICON $Li_{3.25}Ge_{0.25}P_{0.75}S_4$, perovskite $Li_{0.29}La_{0.57}TiO_3$, and sulfide glass Li_3PO_4-Li_2S-SiS_2 all have lower room temperature

conductivities (< 1 mS/cm). Recently, $Li_{10}GeP_2S_{12}$ was demonstrated to be a lithium superionic conductor with a conductivity of 12 mS/cm at room temperature [51].

Since most of these solid electrolytes have much lower conductivity than carbonate liquids, they are limited to thin-film batteries, where the electrolyte is less than 1 μm thick, reducing the electrolyte impedance. These solid electrolytes are mainly produced through thin-film deposition techniques such as RF magnetron sputtering. There are also other techniques including powders and pellets. These techniques are difficult to implement at commercial scale, and the contact between the solid electrode and solid electrolyte is poor. The main application is in biomedical devices such as pacemakers, where there is a requirement for safety, high energy density, but less on power density.

1.2.4 Polymer (Solid and Gel)

Compared to the inorganic solid electrolyte above, solid polymer electrolyte has the same advantages including thin-film, non-volatility, non-flammability and safety, and additionally it is flexible thus can be roll-to-roll printed on large commercial scale. Wright et al. first demonstrated ion conduction in poly(ethylene oxide)-salt complexes (PEO) in 1973. It was later discovered that the safety concern associated with dendrite growth on lithium metal in liquid electrolyte could be resolved by using PEO-based solid polymer electrolyte, which suppressed the growth of dendrites [52-62].

The three main polymer electrolytes are:

1. Solvent-free dry solid polymer (Figure 1.6a): salt dissolved in a high-molecular-weight polymer. Lithium ion conduction is assisted by the segmental motion of the polymer chains (more will be discussed in Chapter 3). It has a low conductivity of 10^{-5} S/cm at room temperature.
2. Gel (Figure 1.6b): salt dissolved in a liquid electrolyte (high liquid content at more than 40% loading level), and a non-conducting solid polymer is used to provide mechanical support and to retain the liquid. This gel system has comparable conductivity (> 10 mS/cm) as liquid electrolyte, which is the only ion conductor, but the same safety and thermal stability issues remain.
3. Plasticized polymer: a small amount of liquid electrolyte is added to a conducting solid polymer to enhance its conductivity. There are two lithium ion conductors in this hybrid system, the liquid and the solid polymer. Its conductivity is in between solid polymer and gel, and has better safety and thermal stability because the amount of liquid electrolyte is small.

(a) 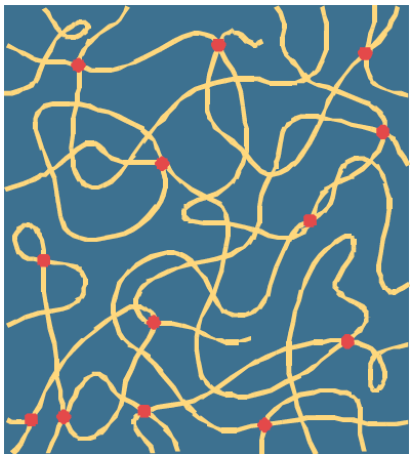 (b) 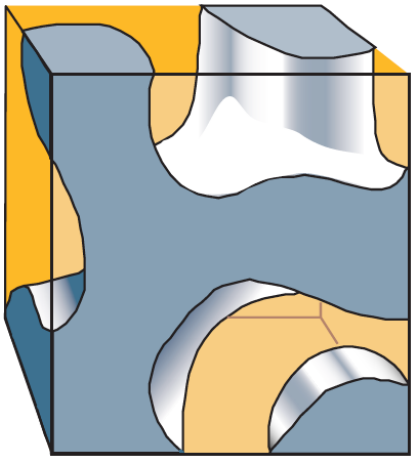

Figure 1.6 Solid polymer (a) and gel electrolyte (b) [2]

Solid polymer electrolytes have room temperature conductivities 2 to 3 orders of magnitudes lower than carbonate liquids or the best inorganic solids. It needs to be heated to above 60 °C to achieve good rate capability. PEO $-(CH_2CH_2O)_n-$ is the most studied solid polymer host, it has a melting temperature of 65 °C, and is chemically and electrochemically stable because of its strong covalent bonds such as C–O, C–C, and C–H. However PEO has a high affinity for crystallization, and lithium ion transport has been shown to occur predominantly in the amorphous phase. Addition of nanoparticles such as silica and alumina can suppress crystallinity, and enhance interfacial and mechanical stability [53]. Comb-branched and block copolymer architectures using short PEO brushes (less than 10 units) can also disrupt crystallinity, produce all-amorphous polymer host at room temperature, and improve the conductivity by an order of magnitude ($< 10^{-4}$ S/cm).

The other approach to improving the conductivity is to incorporate a liquid electrolyte and form a hybrid system, either a gel or plasticized polymer host. But this reintroduces the same undesirable mechanical instability, flammability, volatility, toxicity, and dendrite growth as liquid electrolyte. The common polymer used in these hybrid systems include PEO, poly(methyl methacrylate) (PMMA), polyacrylonitrile (PAN), poly(vinylidene fluoride) (PVdF), polystyrene (PS), and polyethylene (PE). Because the presence of liquid electrolyte, these hybrid systems cannot be used with lithium metal anode, they can only be used in lithium-ion batteries, where graphite is used as the anode [2, 42, 49, 63-67].

Companies such as Bellcore have commercialized hybrid electrolyte-based lithium-ion batteries for consumer electronics. They have the same energy density

as liquid electrolyte-based lithium-ion batteries using the same electrodes (120 Wh/kg), but better safety and fewer electrolyte leakage issues. Also companies such as Avestor and Seeo commercialized the solid polymer lithium metal battery, which uses a liquid-free solid polymer electrolyte and lithium metal anode. This allows the battery to have more than twice the energy density (350 Wh/kg) than lithium-ion. But because the operating temperature is above 60 °C, it is limited to applications such as stationary storage and electric fleet vehicles, where the batteries can be preheated before operation. The conductivities at different temperatures for various electrolytes discussed in this section are shown below (Figure 1.7).

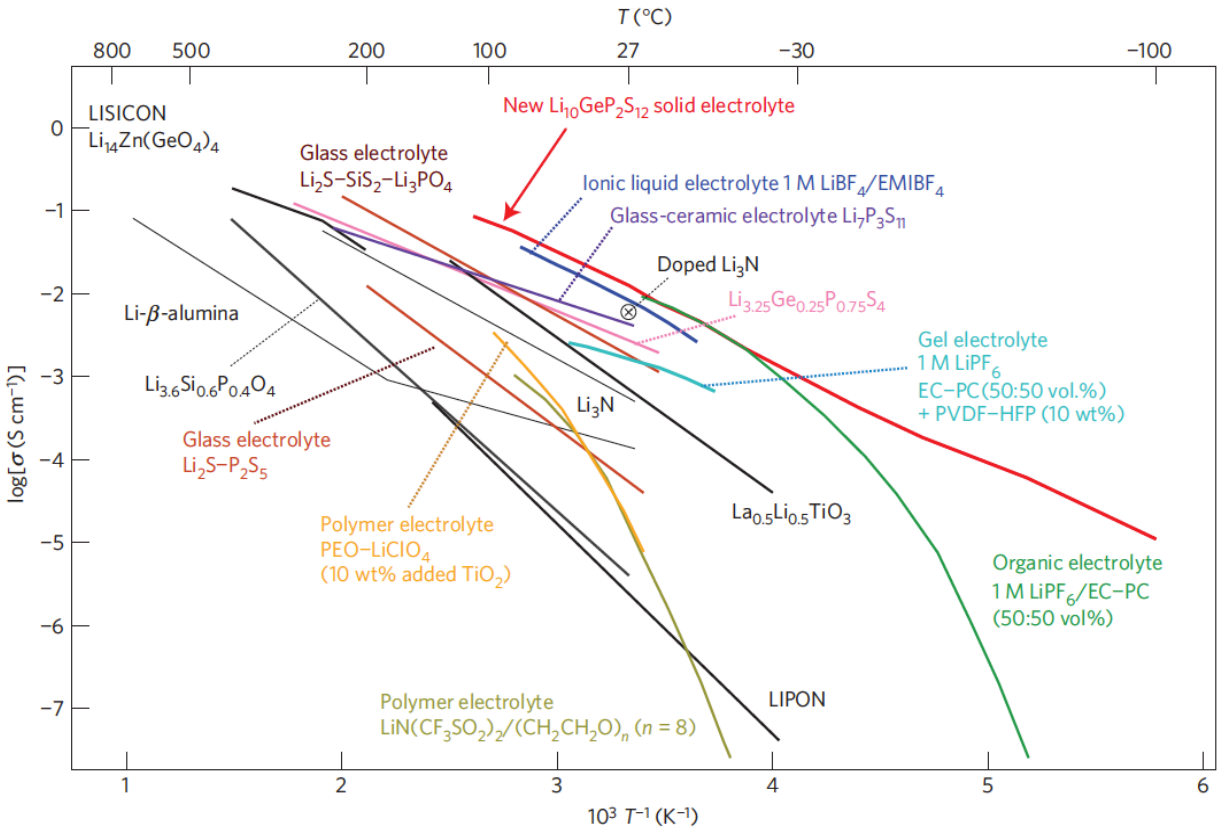

Figure 1.7 Conductivity as a function of temperature for various electrolytes [51]

1.3 Structure of this Thesis

It opens with a general overview of the current state of research and development in the lithium battery community (Chapter 1), and the fundamental thermodynamics and electrochemistry necessary to understand how a lithium battery works (Chapter 2). It progresses to discussing the solid polymer electrolyte (Chapter 3), including its ion conduction mechanism with emphasis on the graft copolymer electrolyte (GCE) that was originally developed in our lab. It then discusses the room temperature performance of a full lithium battery with the solid polymer electrolyte incorporated (Chapter 4), and its dependence on the cathode-electrolyte interfacial impedance.

Chapter 5 is the most important contribution of this thesis, and covers the high temperature performance of the solid polymer lithium battery, which has game-changing implications for the oil and gas drilling industry. In Chapter 6, the thermal stability of the anode-electrolyte interface is discussed to explain the observations made in Chapter 5. Finally in Chapter 7, this thesis closes by going beyond solid polymer and discussing the prospects of a new electrolyte material called polymer ionic liquid (PIL) that combines solid polymer and ionic liquid.

2. Fundamental Thermodynamics

This chapter introduces the fundamental thermodynamics and electrochemistry necessary to understand how a battery works. It will discuss issues that influence the battery voltage, the energy and power density, and other battery terminologies.

2.1 Cell Voltage

In a typical lithium-ion battery, which uses $LiCoO_2$ as the cathode and graphite as the anode, the electrochemical reactions are shown in Figure 2.1.

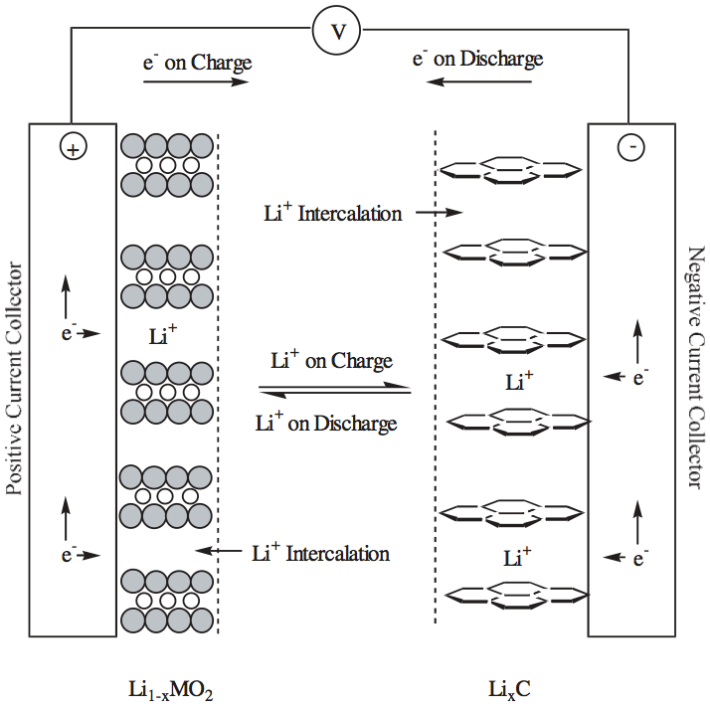

Figure 2.1 Reactions in a lithium-ion battery [68]

$$\text{Cathode (+)}: \ LiCoO_2 \Leftrightarrow CoO_2 + Li^+ + e^-$$

$$\text{Anode (-)}: \ Li^+ + 6C + e^- \Leftrightarrow LiC_6$$

The chemical driving force in these electrochemical reactions is the difference in the chemical potential of the ionic species between the two electrodes ($\Delta\mu$). It is also the difference between the standard Gibbs free energy of formation of the products and reactants (ΔG).

$$\Delta\mu = \Delta G$$

The electrostatic energy of the charged species is given by $-zFE$, where z is the charge number of the mobile ionic species involved in the reaction, E is the voltage between the electrodes, and F is the Faraday's constant (96,500 Coulombs per mol). Under open-circuit equilibrium state, there is no current flowing, and the chemical driving force is balanced by the electrostatic driving force.

$$\Delta G = -zFE$$
$$E = -\frac{\Delta G}{zF} = -\frac{\Delta\mu}{zF}$$

The equilibrium cell voltage is given by the difference in the chemical potentials of the half-cells. In the case of the $LiCoO_2/LiC_6$ lithium-ion battery, the reduction potentials are 0.7 V and −2.9 V respectively compared to standard hydrogen electrode (H_2/H^+), and the overall cell voltage is [68]

$$E = -(-2.9 - 0.7) = 3.6 \text{ V}$$

The chemical potential is also related to the activity or concentration (a) of the ionic species, where R is the gas constant (8.314 J/mol*K).

$$\mu = \mu_0 + RT \ln a$$

The difference in the chemical potential between the two electrodes is given by

$$\mu_+ - \mu_- = RT \ln\left(\frac{a_+}{a_-}\right)$$

and under equilibrium condition, balancing with the electrostatic energy, the cell voltage is related to activity through the Nernst equation

$$E = -\left(\frac{RT}{zF}\right)\ln\left(\frac{a_+}{a_-}\right)$$

The equilibrium cell voltage is also dependent on temperature through the Gibbs-Helmholtz equation, because the entropy changes at different temperatures

$$\Delta G = \Delta H - T\Delta S$$

$$\frac{dE}{dT} = -\frac{1}{zF}\left(\frac{d\Delta G}{dT}\right) = -\frac{1}{zF}\left(-\Delta S\right) = \frac{\Delta S}{zF}$$

So far, we have only considered equilibrium cell voltage with no current flow. The equilibrium cell voltage represents the maximum theoretical energy of the cell. When current *I* starts flowing, there are losses due to polarizations effects that lead to overpotentials. These losses include:

(1) *Charge transfer* polarization at the electrode-electrolyte interphase.

(2) *Concentration polarization* arising from the concentration difference in the reactants and products at the electrode surface and in the bulk electrolyte as a result of *mass transport* or diffusion limitation.

(3) *Ohmic drop* due to internal impedance of the cell. The overpotential is proportional to the applied current, given by *IR*. The total internal impedance is the sum of the impedance of the electrolyte, the electrodes, at the electrode-electrolyte interphase, and the contacts with current collectors. *IR* drop gives rise to Joule heating.

In a redox reaction involving reduced (*R*) and oxidized (*O*) species,

$$O + ne \Leftrightarrow R$$

the current-voltage characteristics is given by the Tafel equation, where a and b are constants, and η is the overpotential [69, 70]

$$\eta = a + b\log i \quad \text{or} \quad i = \exp\left(-\frac{a}{b}\right)\exp\left(\frac{\eta}{b}\right)$$

the current of the forward and backward reactions can be related to the concentration of the electroactive species through a geometric factor (A is the electrode surface area) and rate constants k_f and k_b

$$i_f = nFAk_f C_O$$
$$i_b = nFAk_b C_R$$

the rate constants have Arrhenius form

$$k_f = k_f^0 \exp\left(\frac{-\alpha nF\eta}{RT}\right)$$
$$k_b = k_b^0 \exp\left(\frac{(1-\alpha)nF\eta}{RT}\right)$$

where η is the overpotential relative to a general reference point, k_f^0 and k_b^0 are constants related to the activation barrier for oxidation and reduction respectively, α is the transfer coefficient (ranging from 0 to 1), related to the asymmetry in the activation barrier of the standard free energies in oxidation and reduction.

The rate constants can be calculated by considering the special case of equilibrium (η=0), there is no net current flow (i_f=i_b), and the equilibrium concentrations of the oxidized (C_O^*) and reduced (C_R^*) species are equal

$$k_f^0 C_O^* = k_b^0 C_R^* \quad \text{or} \quad k_f^0 = k_b^0 = k^0$$

where k^0 is the standard rate constant. Under non-equilibrium conditions, the net current is given by the Butler-Volmer equation [70]

$$i = i_f - i_b$$

$$i = nFAk^0\left(C_O \exp\left(\frac{-\alpha nF\eta}{RT}\right) - C_R \exp\left(\frac{(1-\alpha)nF\eta}{RT}\right)\right)$$

The concentrations (C_O and C_R) depend on mass transport, which can occur through convection, migration due to electric potential gradient, and diffusion in concentration gradient. The most important mass transport process in practical batteries is diffusion, and is governed by Fick's second law [70]

$$\frac{\delta C}{\delta t} = D\frac{\delta^2 C}{\delta x^2}$$

where D is the diffusion coefficient.

The final cell voltage, considering the overpotentials at both electrodes due to charge transfer and mass transport limitations and ohmic drop, differentiates from the maximum theoretical voltage E_0 by

$$E = E_0 - \left(\eta_{cat} + \eta_{ano}\right)_{ct} - \left(\eta_{cat} + \eta_{ano}\right)_{mt} - IR$$

The effect of the three different overpotentials is shown in Figure 2.2. Charge transfer or activation overpotential is most prominent at low current, ohmic drop is linear and most important at intermediate current, and concentration polarization due to mass transport is most important at high current.

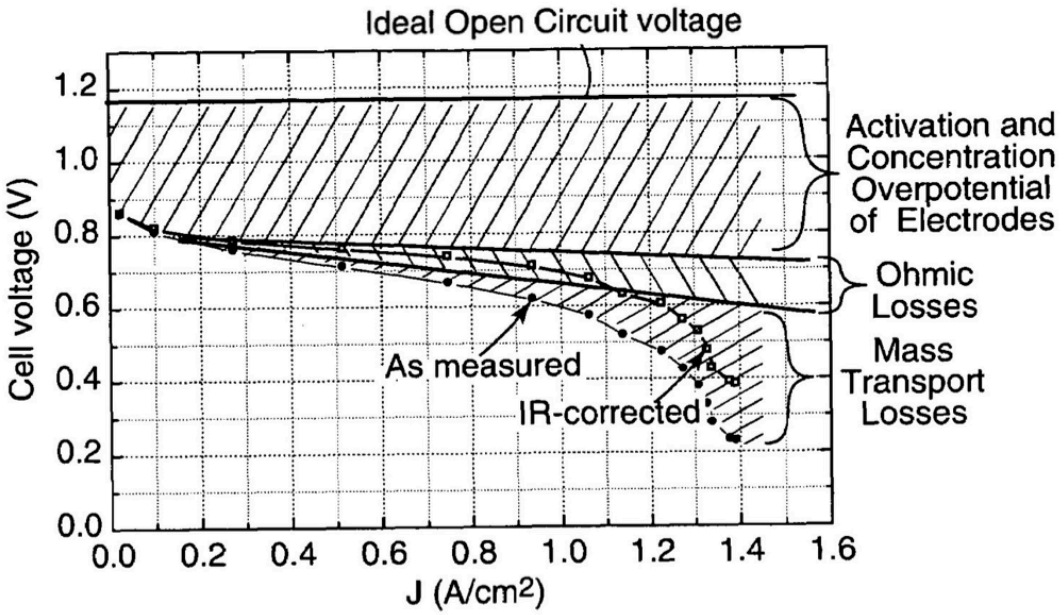

Figure 2.2 Cell polarization as a function of current [69]

In real lithium-ion batteries, the cathode is a porous matrix consisting of binder, intercalant active material, and carbon. The electrolyte penetrates the void space. The porosity and conductivity of the matrix (both electronic and ionic) greatly affect the current density distribution and other electrochemical processes.

2.2 Energy Diagram of a Lithium-ion Battery

To understand electrode-electrolyte compatibility, it is instructive to study the energy diagram. Figure 2.3 shows the schematic for the energies of the electrodes and the electrolyte. Φ_C and Φ_A are the work functions of the cathode and anode respectively, and μ_C and μ_A are their chemical potentials (Fermi energy) of the electroactive species. These are referenced to a general energy level, typically Li/Li^+. E_g is the voltage window or "bandgap" between the lowest unoccupied molecular

orbit (LUMO) and the highest occupied molecular orbit (HOMO) of the electrolyte. V_{OC} is the open circuit voltage of the battery, and determined by the difference between the chemical potentials of the electrodes [6, 7, 71].

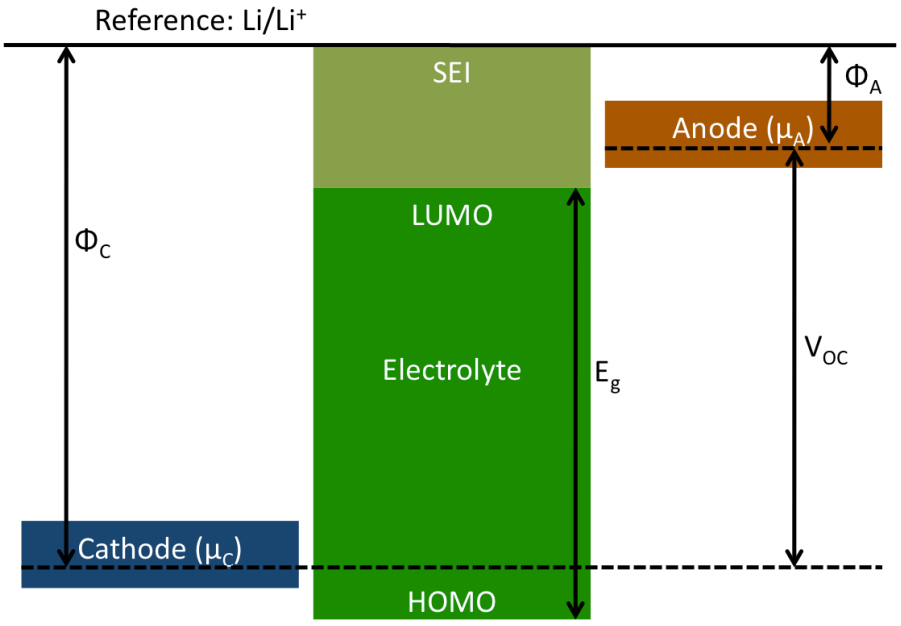

Figure 2.3 Energy diagram of a lithium-ion battery

On the anode side, the chemical potential is typically very close to the reference energy level (Li/Li^+), 0.1 V for graphite, and 0 V for lithium metal. On the cathode side, the chemical potential generally ranges from 3.3 V ($LiFePO_4$) to 4.2 V ($Li(Li_aNi_xMn_yCo_z)O_2$) relative to Li/Li^+. Stable cycling requires the electrolyte to have its LUMO at 0 V versus Li/Li^+, and HOMO higher than 4.2 V versus Li/Li^+. In an ideal battery, the voltage window of the electrolyte (E_g) should be wider than the open-circuit voltage (V_{OC})

$$V_{OC} = \Phi_C - \Phi_A \leq E_g$$

Most electrolyte satisfy the HOMO requirement, their cathodic limit is more than 4.5 V versus Li/Li^+. But the LUMO of most electrolyte is close to 1 V below

Li/Li^+, thus the chemical potential of the anode (μ_A) lies above the LUMO of the electrolyte, and reduces the electrolyte. This continuous reaction between the electrolyte and the anode consumes lithium ions, leads to electrolyte depletion, deposits thick reaction products on the anode surface, and results in high impedance at the interface and capacity fade.

Some solvents such as EC undergo limited reactions to form an amorphous ion-conducting passivation film (SEI) on the anode. From the energy diagram, the SEI effectively widens the voltage window of the electrolyte on the anode side. The reduction of the electrolyte by the anode is suppressed because the anode chemical potential now lies below the LUMO of the SEI. The SEI has been shown to consist primarily of $Li_2(OCO_2(CH_2)_2OCO_2)_2$, Li_2CO_3, and $LiOCH_3$. The stability of the SEI layer greatly affects the safety of the overall battery. During fast charging, there might be enough lithium deposited on the SEI, resulting in lithium plating and dendrite formation, and leading to safety hazards [35, 72-74].

High energy density and high voltage lithium-ion batteries require the difference between the electrode work functions to be as high as possible. This demands electrolytes with even wider voltage window, and the formation of stable and fast healing passivation films.

2.3 Performance Metrics

2.3.1 Energy and Power Density

The charge capacity stored in a battery can be calculated using

$$Q = \int I dt$$

where *I* is the current either applied to or produced by the battery, and integrated over time. Energy is calculated by integrating the cell voltage, which is dependent on the state of charge, over all charge capacity

$$\text{Energy} = \int Vdq$$

Power is calculated by integrating the cell voltage, which is also dependent on current, over current [68]

$$\text{Power} = \int VdI$$

The specific capacity of lithium-ion battery cathodes ranges from 100 mAh/g ($LiMn_2O_4$) to 220 mAh/g ($Li(Li_aNi_xMn_yCo_z)O_2$), and the specific energy density ranges from 400 Wh/kg to 920 Wh/kg. The specific energy density decreases from pure cathode material to battery, and then to pack, as more inactive materials are added. On the battery level, the specific energy density ranges from 100 Wh/kg to 150 Wh/kg, and the specific power density ranges from 300 W/kg to 1500 W/kg. In comparison, the energy density of lithium-metal battery is 350 Wh/kg, gasoline is 13,000 Wh/kg, and uranium-235 is almost 6 billion Wh/kg [75].

2.3.2 Current Rate

The current rate, or "C-rate", is defined as the current needed to fully charge/discharge a battery's nominal capacity in a certain amount of time.

$$\frac{C}{n} = \frac{\text{Full capacity (Ah)}}{\text{hours}} = \text{current (A)}$$

For example in a battery with 1Ah capacity, a C/20 rate is to charge/discharge the battery in 20 hours, or at a 50 mA current; a 20C rate is to charge/discharge the

battery in 1/20 hours (3 minutes), or at a 20 A current. 20C is a much higher current than C/20.

2.3.3 Efficiency

The amount of energy needed to charge a lithium-ion battery is always higher than the amount of energy released by the battery on discharge. This is due to overpotentials, and side reactions such as passivation film formation on anode. The coulometric efficiency can be much closer to 1, since it does not take into account the cell voltage.

$$\text{Coulometric eff.} = \frac{Q_{dis}}{Q_{cha}}$$

$$\text{Energy eff.} = \frac{\int V_{dis} dq_{dis}}{\int V_{cha} dq_{cha}}$$

2.3.4 Cycle and Shelf Life

When a battery is charged and discharged repeatedly, it undergoes capacity fade, mainly due to mechanical deterioration in the electrode structures. A battery is considered a “failure” once its capacity is below 80% of its initial capacity. Many factors can influence cycle life, including temperature, charging current, and depth of discharge. Even when a battery is in open-circuit condition, undesirable chemical reactions could also reduce its storage shelf life [68].

3. Polymer Electrolyte

This chapter introduces ion conduction mechanism in a polymer electrolyte, with emphasis on the microphase separating graft copolymer electrolyte originally developed in our lab. It also covers background information on two experimental techniques extensively used throughout this thesis, electrochemical impedance spectroscopy (EIS) and differential scanning calorimetry (DSC).

3.1 Conduction Mechanism

3.1.1 Thermodynamics of Salt Dissolution in Polymer

At constant temperature and pressure, the dissolution of salt in any solvent, whether liquid or polymer must be accompanied by a reduction in the Gibbs free energy, $\Delta G = \Delta H - T\Delta S$. The change in enthalpy is influenced by the lattice energy of the salt (high lattice energy for ions with high charges and small radii), and the creation of coordinating sites in the polymer, both lead to positive ΔH, making the dissolution less favorable; and the interaction between polymer coordinating group and cation, and the electrostatic interaction between the dissolved ions, both lead to negative ΔH, favoring the dissolution.

The change in entropy has competition from two components. The entropy increases as the salt crystalline lattice is broken and ions are dissolved in the polymer. The entropy decreases as the polymer chains stiffen due to coordination with ions. This reduces the segmental motion of the polymer. It will be shown later in this chapter that the glass transition temperature of the polymer (T_g) increases

with increasing salt concentration. It has been reported that the decrease in entropy due to the pinning of polymer chains is larger than the increase in entropy due to lattice breaking, and the net change in entropy is typically negative, disfavoring dissolution especially at high temperatures, in which case the salt precipitates out.

Polyethers, polyesters, and polyimines have shown strong coordinating groups for solvating cations, which mainly depends on the number of molecules that can pack around the cations without excessive strain. Poly(ethylene oxide) PEO $(CH_2CH_2O)_n$ has just the right spacing between coordinating ether oxygen atoms for maximum ion solvation, while PMO $(CH_2O)_n$ and PPO $(CH_2CH_2CH_2O)_n$ are much weaker solvents, even though they have the same coordinating atoms [76-79].

The oxygen spacing in PEO (2.88 Å) is close to that in water (2.85 Å). This allows PEO to have comparable solvating properties and polarizability as water, and makes it an ideal solvent for alkali metal, alkaline-earth metal, and transition metal cations. According to the hard-soft acid-base theory, the strongest interaction is between hard-hard and soft-soft matches. The strongest solvation in PEO, which can be considered as a hard base, is with a hard acid or cation such as Li^+, Na^+, Mg^{2+}, and Ca^{2+}. However, unlike water, PEO is a weak solvent for anions. The most soluble anions are large, polarizable, and have monovalent delocalized charge. The common anions include ClO_4^-, $CF_3SO_3^-$, $(CF_3SO_2)_2N^-$, and PF_6^- [80-83].

In water, which has a high dielectric constant of 78, the dipoles associated with the H_2O molecules surround the ions and reduce their association and mutual interaction. But in PEO, which has a much lower dielectric constant between 5 and 8, the ions interact strongly and re-associate to form ion clusters, or contact ion

aggregates, especially at high salt concentrations. This reduces the effect of ion dissociation during lattice breaking, decreases the entropy, and disfavors salt dissolution. In PEO/salt complexes, the cations fit within the PEO helix, and leave empty sites around the cations to be occupied by anions.

Figure 3.1 shows the coordination of $LiCF_3SO_3$ in PEO. The Li^+ cation is in the center, coordinated by two oxygen atoms (O4 and O7) from two $CF_3SO_3^-$ anions on each side, and three oxygen atoms (O1, O2, and O3) from the PEO helix.

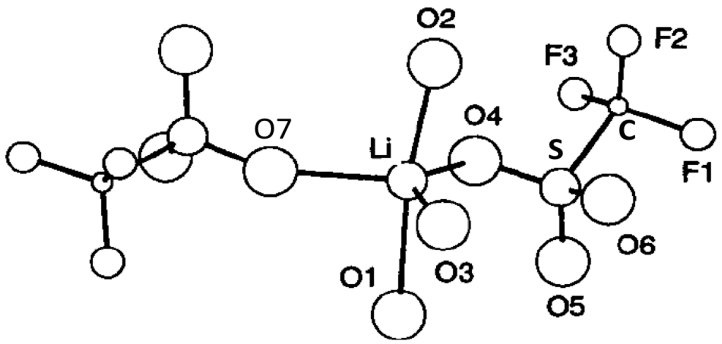

Figure 3.1 Coordination of $LiCF_3SO_3$ salt in PEO [84]

3.1.2 Ion Conduction in Polymer

X-ray diffraction data have shown that Li^+ cations, which have radii of 0.76 Å, are located within the PEO helix. Each turn of the helix contains one Li^+ cation coordinated by three oxygen atoms from the PEO chain. The PEO chain forms a one-dimensional coordination complex. The motion of the Li^+ cations can be both assisted by polymer chain segmental motion, shown as intra and inter-chain movement in Figure 3.2, and influenced by ion cluster, shown as intracluster and intercluster movement in Figure 3.2.

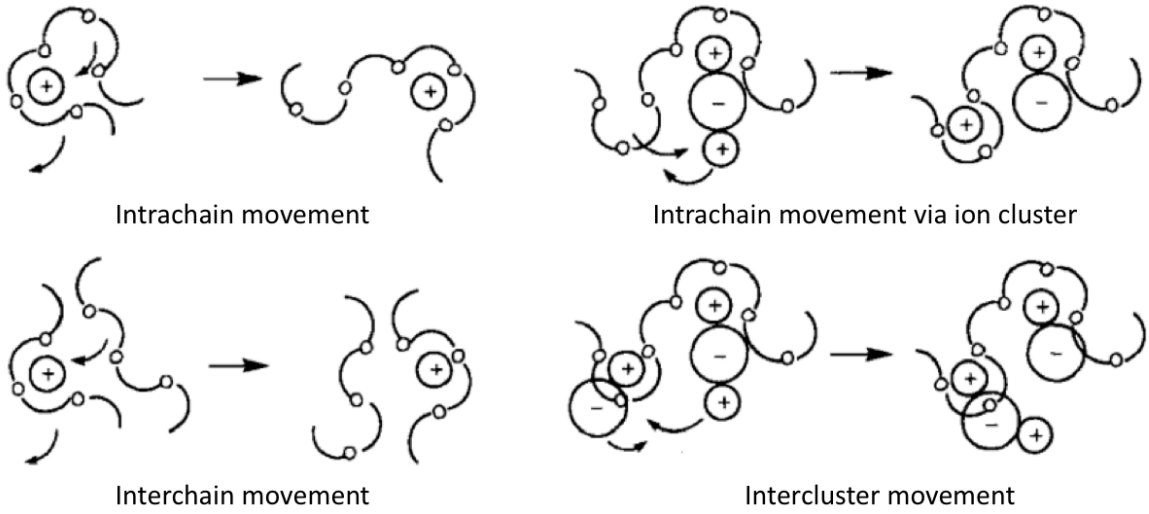

Figure 3.2 Cation motion in polymer [84]

The PEO segmental motions are typically associated with the torsion around C–C, and C–O bonds. The semi-random segmental motion assists ion conduction by forming and breaking coordination sites for the solvated ions and providing free volume for the ions to diffuse under the influence of the electric field. The onset of the segmental motion occurs in the vicinity of the glass transition temperature T_g, and becomes more facile as the temperature increases further beyond the T_g. At higher temperatures, local voids are produced by the polymer expansion, allowing polymer segments to move into the free volume [85].

Since the segmental motion is far more rapid in the amorphous phase above the T_g than in the crystalline phase, ion transport in polymer occurs predominantly in the amorphous phase. However, recently Li^+ conduction in crystalline PEO_6:$LiAsF_6$ was demonstrated, although the conductivity is more than two orders of magnitude lower than in amorphous PEO. The crystalline or amorphous phase of

the PEO/salt complex depends on the composition, temperature and preparation method [52, 54, 86].

Unlike in liquid, where ions move with their solvent sheath intact and the transport is related to the macroscopic viscosity of the solvent; in solid polymer, where the polymer chains are increasingly entangled and cannot move over long distances, the ion transport is related to the microscopic viscosity of the segments of the polymer chains. The transport of ions along polymer chains needs to overcome two activation barriers, both are illustrated in Figure 3.3. One is the solvation of the ions by the coordinating EO units. This process involves the forming and breaking of chemical bonds, has Arrhenius dependence, and the conductivity is given by

$$\sigma = A\exp\left(\frac{-E_a}{kT}\right)$$

where σ is the conductivity, A is a constant, and E_a is the activation energy associated with the bonds. Because ions must dissociate from the coordination sites in order to move in the solid polymer, if the bonds are too strong, the cations become immobile. The cation-polymer bonds need to be strong enough for salt dissolution, but weak enough to allow for cation mobility.

The other is associated with the transport of ions from one coordination site to another. This process is related to the segmental motion of the polymer, has Vogel-Tammann-Fulcher (VTF) dependence [87-89], and the conductivity is

$$\sigma = \frac{A}{\sqrt{T}}\exp\left(\frac{-E_a}{k(T-T_0)}\right)$$

where T_0 is a reference temperature generally chosen to be 50 K below T_g. This equation suggests that thermal motion above T_0 contributes to transport process, and faster motion is expected for polymer with low T_g.

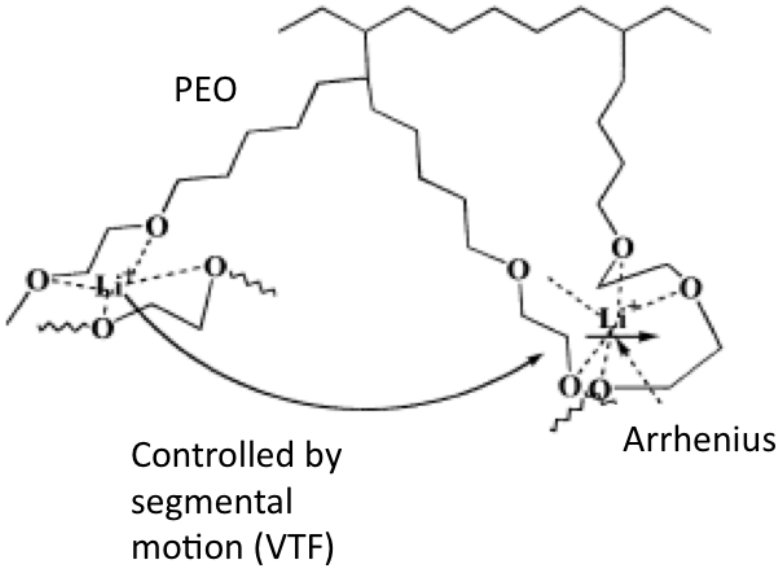

Figure 3.3 Contributions to ion mobility [85]

The VTF process is related to the T_g, thus rate-limiting at low temperatures. At high temperatures, the segmental motion becomes facile enough that the Arrhenius process becomes rate limiting.

At constant pressure and temperature, the conductivity can be also related to the ion concentration through

$$\sigma(T,P) = qc(\mu_+ + \mu_-)$$

where q is the charge, c is the concentration, and μ is the mobility for the cations and anions. The mobility is related to the diffusion coefficient D through the Nernst-Einstein relation

$$\mu = \frac{qD}{kT}$$

The effect of high ion concentration is similar to the effect of high temperature on ion diffusion, where the process is controlled by an Arrhenius-like thermally activated mechanism. For anion diffusion mechanism, because they do not form strong bonds with the polymer hosts, the anion transport principally depends on free segmental motion, or a VTF-type dependence at all temperatures and concentrations.

3.2 Development of Graft Copolymer Electrolyte

In solid polymer lithium batteries, the polymer acts as both the electrolyte and the separator, and needs both good ionic conductivity and mechanical stability. If the goal is to maximize conductivity, then amorphous polymers with low T_g are desired. Because the larger the difference between the operating temperature and the T_g, the faster the segmental motion. However, polymers with high crystallinity and T_g generally have good mechanical properties such as shear modulus and tensile strength. There is a compromise between ionic conductivity and mechanical property.

In the design of polymer electrolytes, it is important to decouple the ion transport from the mechanical properties. One approach is to alter the polymer architecture to introduce irregularity and suppress crystallinity. Amorphous comb-branched block copolymers are generally based on short PEO chains supported by a backbone. The backbone is typically more rigid and has a higher T_g to enhance the mechanical stability. The common backbones include polymethacrylate and polystyrene. The optimum PEO chain length is found to be between 5 to 10 EO units,

enough to solvate Li^+ ions, but too short for it to fold on itself and pack into regular forms, favoring high segmental motion and bulk conductivity. It has been found that if the chain length is longer, crystallinity increases, and conductivity decreases. If the chain length is shorter, the stiffness of the backbone has a greater influence and the conductivity decreases too [90, 91].

In general the T_gs of the comb-branched polymers are lower than linear polymers, and their mechanical properties are more liquid-like. Chemical or radiation crosslinking can be used to enhance the mechanical stability after the polymer electrolyte film is formed into the desired shape and thickness. However, once the polymer is crosslinked, it can no longer be reformed, and the synthesis process is complicated.

Another approach is using microphase separation [62, 80, 92-97]. A diblock copolymer consists of two low-T_g, amorphous, and immiscible polymer blocks covalently bonded end-to-end. At high temperatures, above the order-disorder transition (T_{ODT}), or dissolved in a common solvent, the polymer segments are mixed, and the copolymer behaves as a liquid. At low temperatures, below the T_{ODT}, the repulsion between the blocks induces local segregation, or microphase separation, but since the blocks are covalently bonded, they form periodically spaced nanoscale domains. This gives the block copolymer a solid-like property, as illustrated in Figure 3.4. The microphase separation is reversible by controlling the temperature or the solvents.

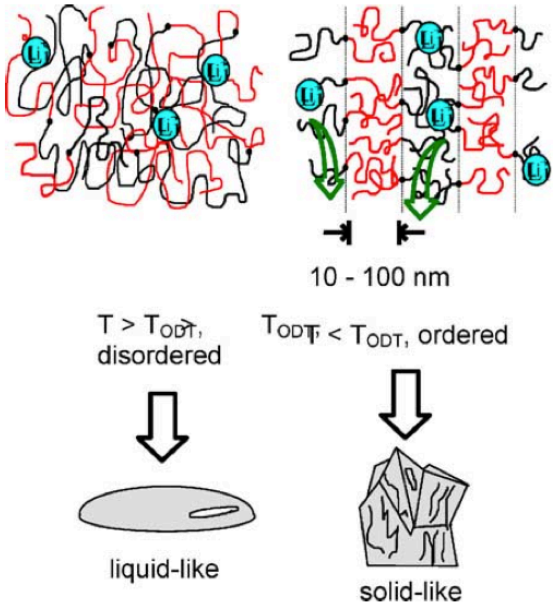

Figure 3.4 Microphase separation in block copolymer [94]

Generally only one of the two blocks is exclusively responsible for Li^+ ion conduction. One of the most studied blocks is the hydrophilic poly(oxyethylene)$_9$ methacrylate (POEM), which has a methacrylate backbone and short 9-units long PEO brushes. The amorphous POEM has a low T_g of −60 °C, and behaves as a viscous liquid at room temperature, giving it great segmental motion and Li^+ conductivity.

The other block, although non-ion conducting, because it is covalently bonded to POEM and forming a contiguous copolymer, its segmental motion is coupled with that of POEM, and its T_g greatly affects the conductivity of the entire copolymer. Philip Soo demonstrated that using hydrophobic blocks with decreasing T_g, poly(methyl methacrylate) PMMA, poly(butyl methacrylate) PBMA, and poly(lauryl methacrylate) PLMA, whose T_gs are 100 °C, 40 °C, and −35 °C respectively, the conductivity of the copolymer increased monotonically as the T_g of the non-conducting block decreased. All of these block copolymers were

mechanically stable due to microphase separation between the hydrophilic POEM and hydrophobic P-alkyl-MAs, and when complexed with lithium triflate ($LiCF_3SO_3$) salt, demonstrated a room temperature conductivity on the order of 10^{-6} S/cm. A TEM image of the POEM-b-PLMA (at 50:50 weight ratio) is shown in Figure 3.5, where the darker domains represent the hydrophilic POEM stained with RuO_4, providing the Li^+ pathways [62].

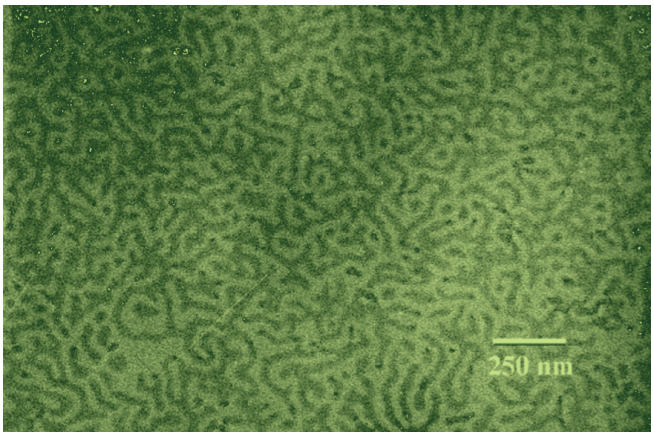

Figure 3.5 TEM of microphase separation in block copolymer [94]

Philip Soo and Patrick Trapa also showed that by forming a graft copolymer between POEM and poly(dimethyl siloxane) PDMS, which has an even lower T_g of −123 °C, substantially lower than that of the alkyl methacrylates, the room temperature conductivity exceeded 10^{-5} S/cm. Because the segmental motion of PDMS is much more facile than that of POEM, the ion conduction of the copolymer is limited by POEM, and the conductivity of POEM-g-PDMS (at 70:30 weight ratio) was close to that of pure POEM homopolymer, which is a liquid at room temperature.

A comparison of the architectures of the block and graft copolymers is shown in Figure 3.6, where the short brushes represent the Li^+ ion-conducting POEM, and

the red side chains represent the non-ion conducting supporting block. The domain spacing of POEM-g-PDMS was determined to be 25 nm using small-angle neutron scattering (SANS). The copolymer showed no significant thermal decomposition at temperatures above 250 °C using thermal gravimetric analysis (TGA).

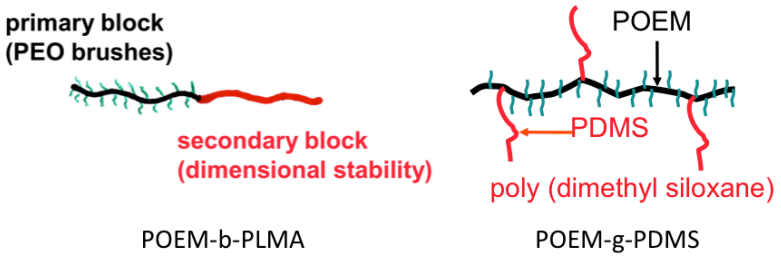

Figure 3.6 Comparison between block and graft copolymers [94]

Atom transfer radical polymerization (ATRP), which is a controlled radical polymerization technique, was used to synthesize the block copolymer (POEM-b-PBMA). Its utility marked a major improvement over the laborious anionic methods that were traditionally used in synthesizing novel microphase separated polymers. ATRP involved the use of an alkyl halide, methyl-2-bromopropionate, as the initiator, and a transition metal-based catalyst, CuCl, and a ligand (L) to provide an equilibrium between the propagating or active polymer and the dormant or inactive polymer. During initiation, the initiator places the halogen atom (Cl) on the monomer chain end. During propagation, the Cl atom is transferred back and forth between the chain end and the metal catalyst, creating sites for monomer insertion. Upon completion, the halogen atom caps the polymer chain end, and the metal catalyst is removed using ion exchange. Although there were always vestiges of metal catalysts present in the polymer, the Cu impurity did not show adverse effect

on the battery performance. ATRP allowed for controlled and uniform chain growth, and resulted in polymers with low polydispersity [97].

Free radical polymerization, on the other hand, is one of the simplest and most versatile polymerization techniques, and is widely used in industrial-scale chemical manufacturing plants. In fact more than 70% of the commercial polymers are produced using this technique. While the random nature of free radical polymerization makes it unusable for block copolymers, where precise control of the architecture is needed, this is not a problem for the random graft copolymer, and was used to synthesize POEM-g-PDMS. During the polymerization process, a thermally-activated initiator, azoisobutylnitrile (AIBN) cleaves the C=C double bonds in the metharylate backbone of the monomers, leading to C−C single bonds and free radicals allowing monomers to add during propagation. The process ends when it runs out of free radicals, either through the combination of two polymer chain ends or between a polymer chain and an initiator radical [97].

3.3 Experimental

3.3.1 Polymer Electrolyte Synthesis

The graft copolymers (POEM-g-PDMS and POEA-g-PDMS at 70:30 weight ratio) were synthesized using the free radical polymerization technique described in Patrick Trapa's thesis. Both the POEM monomer (poly(ethylene glycol) methyl ether methacrylate) and the POEA monomer (poly(ethylene glycol) methyl ether acrylate) have 8 repeating EO units were purchased from Sigma Aldrich, as shown in Figure 3.7. Their average molecular weights are M_n=475 g/mol and 480 g/mol respectively.

They both have a density of 1.09 g/mL and are liquid at room temperature. The PDMS macromonomer (monomethacryloxypropyl-terminated polydimethylsiloxane asymmetric) was purchased from Gelest and has a molecular weight of M_n=10,000 g/mol, n=145). Both the initiator, 2,2'-Azobis(2-methylpropionitrile) (AIBN) and the salts, lithium bis(trifluoromethane)sulfonimide (LiTFSI) were purchased from Sigma Aldrich and have a purity of 98% and 99.95% respectively. All solvents including ethyl acetate (EA), petroleum ether (PE) and tetrahydrofuran (THF) were purchased from Sigma Aldrich, and all chemicals were used as received.

26 mL of POEM (or POEA) monomers, 12 mL of PDMS macromonomers, and 12 mg of AIBN (monomer:initiator=825:1) were mixed in 160 mL of EA. The flask containing the solution was sealed with a rubber septum and purged with argon for 45 minutes. The solution was then heated to 72 °C (AIBN has a decomposition rate of 3.2×10^{-5} s^{-1}) in an oil bath under constant stirring for 24 hours. The initially clear solution typically became visibly milky within 2 hours. The final solution was precipitated in an immiscible solvent, PE. The polymer was dried at 80 °C under less than 5 milliTorr vacuum for 5 days to remove the residual moisture. It was found that if the polymer were not dried properly, the excessive moisture would lead to crack formation when the polymer was casted into thin films. The final graft copolymer (shown in Figure 3.8b) had a molecular weight of 500,000 g/mol using gel permeation chromatography with polystyrene calibration standard.

The graft copolymer was complexed with LiTFSI at a Li:EO ratio of 1:20 (1 g of POEM-g-PDMS (70:30) with 170 mg of LiTFSI) in a common solvent of THF to form the electrolyte.

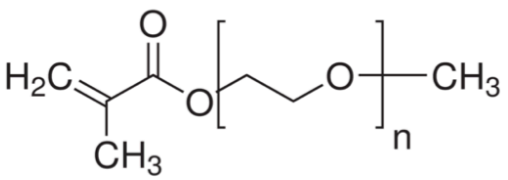

Poly(ethylene glycol) methyl ether methacrylate (POEM)

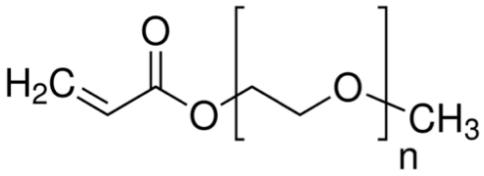

Poly(ethylene glycol) methyl ether acrylate (POEA)

Figure 3.7 POEM and POEA

3.3.2 Conductivity Measurement Setup

The conductivity of the graft copolymer electrolyte was measured in a planar geometry shown in Figure 3.8a, where two stainless steel blocking electrodes (MTI Corp) were used as current collectors (working and counter electrodes), and a Teflon spacer (McMaster Carr) with known dimension was used to confine the polymer film. The entire setup was assembled inside an argon-filled glovebox and sealed in a CR2032 coin cell (Figure 3.8c Pred Materials) to be tested outside. The temperature dependence of the conductivity was measured by inserting the coin cell in a high temperature holder (up to 280 °C from Digi Key), and heating it using a resistive heating tape (McMaster Carr). The resistance was measured through electrochemical impedance spectroscopy, and using a Solartron Electrochemical Interface 1286 coupled with a Solartron Frequency Response Analyzer 1260. The frequency scan ranged from 1 MHz to 100 mHz at 10 mV voltage fluctuation with 0 bias voltage. The conductivity was extracted from the dimension of the spacer and the measured resistance values.

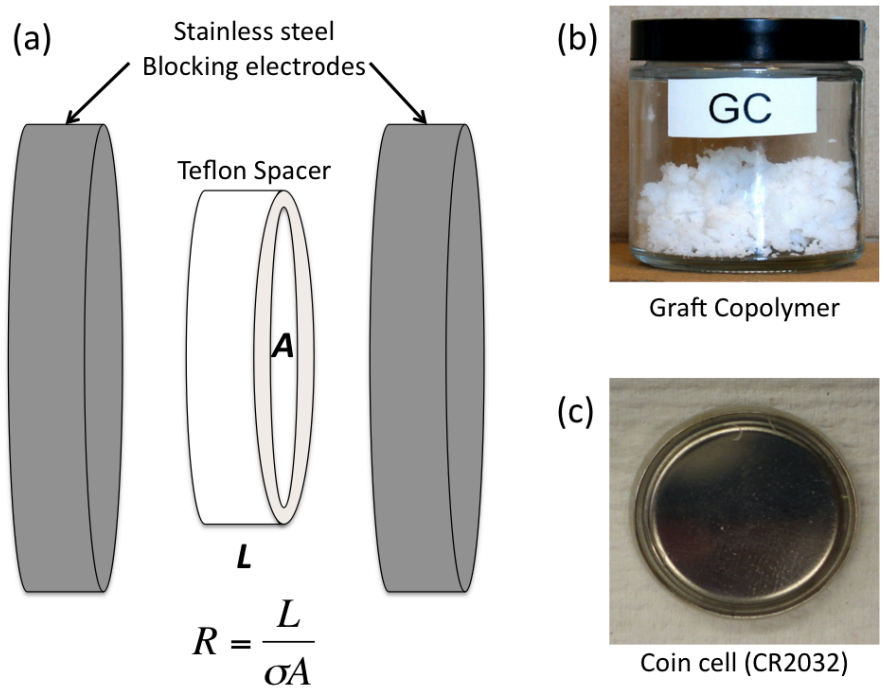

Figure 3.8 Polymer electrolyte conductivity measurement setup

3.4 Characterization Techniques

The relation between the polymer segmental motion and conductivity was studied using mainly two techniques: differential scanning calorimetry (DSC) to measure the T_g and crystallinity of the polymer, and electrochemical impedance spectroscopy (EIS) to measure the resistance. Since these are used extensively throughout the thesis, especially EIS, this section covers the basic background principles.

3.4.1 Differential Scanning Calorimetry (DSC)

DSC records the difference in the amount of heat required to raise the temperatures of the sample and reference (inert over the temperature range,

typically an empty aluminum pan) at a constant rate as a function of temperature and time. Since the chamber is at constant pressure, the heat flow corresponds to enthalpy change. Nitrogen gas flow is used to create a moisture-free environment (Figure 3.9). A Perkin Elmer Pyris 1 DSC capable of liquid nitrogen cooling down to −180 °C was used, about 10 mg of polymer was placed in each sample pan, and the temperature scan rate (both cooling and heating) was 10 K/min.

$$\left(\frac{dq}{dt}\right)_P = \frac{dH}{dt}$$

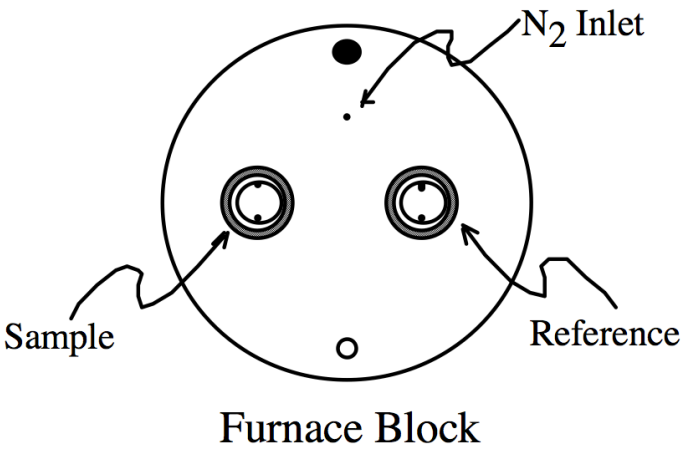

Figure 3.9 Differential scanning calorimetry sample and reference holder

When the sample undergoes phase transformation, the amount of heat flowing to it can be greater or less than the reference to maintain the same temperature. In an endothermic process such as melting, the heat flow to the sample is positive compared to the reference. In an exothermic process such as crystallization, the heat flow to the sample is negative compared to the reference. The heat capacity can be calculated from the heat flow and temperature scan rate.

$$C_P = \left(\frac{dq}{dT}\right)_P = \left(\frac{dH}{dT}\right)_P = \frac{dH}{dt}\frac{dt}{dT}$$

When the amorphous polymer sample undergoes glass transition, it converts from a brittle glass to a flexible rubber. This transition greatly affects the polymer segmental motion. The specific heat, the coefficient for thermal expansion, and the dielectric constant of the polymer all change rapidly. On the DSC curve, the T_g is manifested as a shift in the baseline (Figure 3.10). On a second order transition (T_g), the heat capacity changes, but there is no heat transfer to the surrounding, and the volume changes smoothly accommodating the greater segmental motion. On first order transitions (T_c and T_m), there is heat transfer between the system and the surrounding, and the volume changes abruptly.

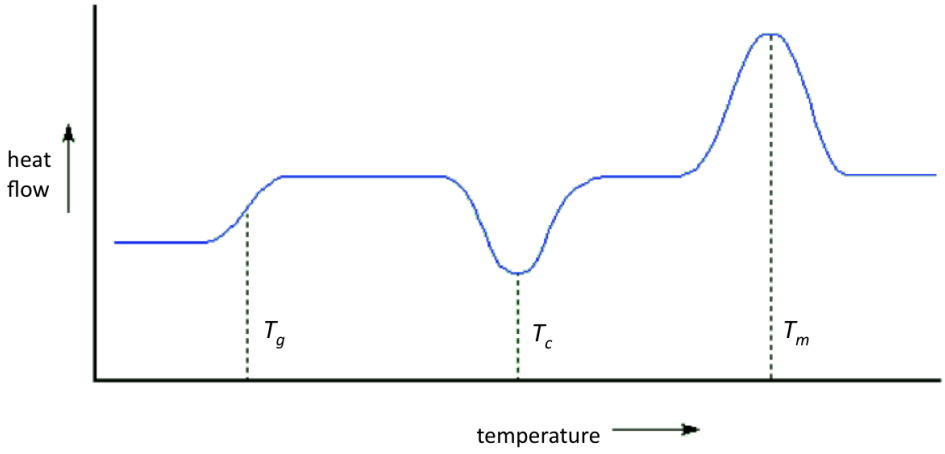

Figure 3.10 A DSC scan with common features

3.4.2 Electrochemical Impedance Spectroscopy (EIS)

In the anecdote of the blind men and the elephant, the blind men touched only small parts of the elephant and made false assumptions about what the overall elephant looked like (Figure 3.11). EIS is similar in that it measures the macroscopic quantities such as current and voltage of an electrochemical system, but the values are influenced by every process involved, and the final interpretation is often

controversial and ambiguous. EIS is a sensitive in-situ technique, but it alone is not enough to provide a direct measurement for the physical properties of the system. EIS must be combined with understanding of the physical and chemical characteristics of the system in order to develop an accurate model. Other techniques include in-situ and ex-situ surface analysis, chemical analysis, and microscopy. The final model should be consistent with all experimental observations [98].

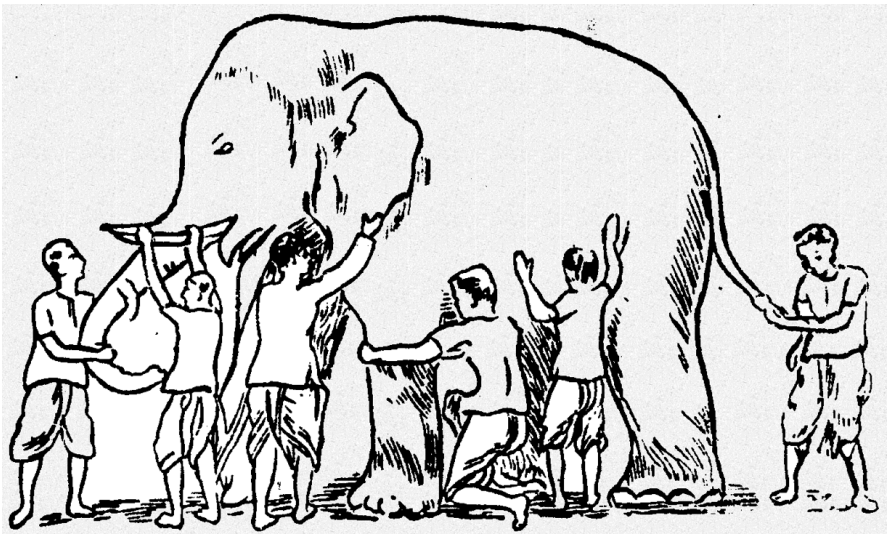

Figure 3.11 The blind men and the elephant

EIS is a linear transfer function that inputs a frequency-dependent small-amplitude sinusoidal voltage perturbation and measures the current response. Because the entire electrochemical system can be modeled using simple circuit elements such as resistors, capacitors and inductors, and their current-voltage characteristics have different frequency dependence, varying the frequency can disentangle the different reactions and extrapolate the contributions from the

various elements. The circuit elements used to model the system, and their current-voltage characteristics and impedances are shown in Figure 3.12.

Resistor		$V = I \times R$	$Z_R = R$
Capacitor	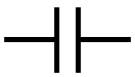	$I = C\frac{dV}{dt}$	$Z_C = \frac{1}{j\omega C} = -\frac{j}{\omega C}$
Inductor	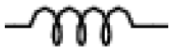	$\mathrm{V} = \mathrm{L}\frac{\mathrm{dI}}{\mathrm{dt}}$	$\mathrm{Z_L} = \mathrm{j}\omega\mathrm{L}$

Figure 3.12 Current-voltage characteristics and impedances

Under steady-state conditions (*dV/dt=0*), the current through the resistor is proportional to the applied voltage, the capacitor is equivalent to an open circuit, and the inductor is equivalent to a short circuit. When elements are in series, the current flowing through them is the same, and the overall voltage is the sum of voltages across individual elements. When elements are in parallel, the voltage is the same for all elements, and the overall current is the sum of current flowing through each element. Impedance contributions are additive in series and inverse-additive in parallel.

$$\text{in series}: \; Z = \sum Z_n$$

$$\text{in parallel}: \; Z = \left(\sum \frac{1}{Z_n} \right)^{-1}$$

When a sinusoidal voltage signal is applied

$$V(t) = |\Delta V| \cos(\omega t)$$

the current response is given by

$$I(t) = |\Delta I| \cos(\omega t + \phi)$$

The impedance response has both real and imaginary parts

$$Z = Z_{re} + jZ_{im} = |Z|\exp(j\phi)$$

where /*Z*/ is the amplitude and given by

$$|Z| = \sqrt{Z_{re}^2 + Z_{im}^2}$$

and Φ is the phase angle given by

$$\phi = \tan^{-1}\left(\frac{Z_{im}}{Z_{re}}\right)$$

The representation of the imaginary and real part of impedance is called the Nyquist plot. The representation of the magnitude and phase of impedance as a function of frequency is called the Bode plot.

EIS equivalent circuit models consisting only of Voigt elements such as the resistor, capacitor, and inductor, are based on assumptions that the electrodes have perfectly smooth and uniform active surface and the reactions involved have only a single-valued time constant. These assumptions are generally invalid due to surface heterogeneities such as grain boundaries, surface roughness, electrode porosity, oxide layers, non-uniform current distribution and mass transfer, and other variations in surface properties. These all lead to distributions in the time constants, both along and normal to the surface of the electrode.

The time constant or frequency dispersion is often modeled using a constant phase element (CPE). The CPE is used to provide a better fit to a depressed Nyquist semicircle, although it does not necessarily describe real physical phenomena. While the use of CPE is controversial, it reflects the difference between theoretical models and practical systems, and the assumption that the time constant has a distribution is more practical than assuming it is a single value. The impedance of CPE is given by

$$Z = \frac{1}{(j\omega)^{\alpha} Q} = \frac{1}{(j\omega\tau_0)^{\alpha}}$$

where Q is the CPE coefficient and proportional to the active area, and τ_0 is the characteristic time constant. The constant phase is (90°α). It is important to note that when $\alpha=1$, the CPE behaves as a capacitor; when $\alpha=0$, the CPE behaves as a resistor; when $\alpha=-1$, the CPE behaves as an inductor; and when $\alpha=1/2$, the CPE behaves as the Warburg impedance, which describes a semi-infinite linear diffusion through a large planar electrode. In all cases, both α and Q are independent of frequency.

For an ideally polarized blocking electrode, the equivalent circuit model is shown in Figure 3.13. It consists of a distribution of RC serial circuits connected in parallel, and each with the time constant of $(R_eC_0)_i$. CPE behavior could arise from the 2D radial distribution of both R_e and C_0 along the electrode surface. The overall impedance needs to be summed over all time constants τ_i.

$$\frac{1}{Z} = \frac{1}{R_e + \frac{1}{(j\omega)^{\alpha} Q}} = \sum_i \frac{1}{\left[R_{ei} + \frac{R_{ei}}{(j\omega\tau_i)}\right]}$$

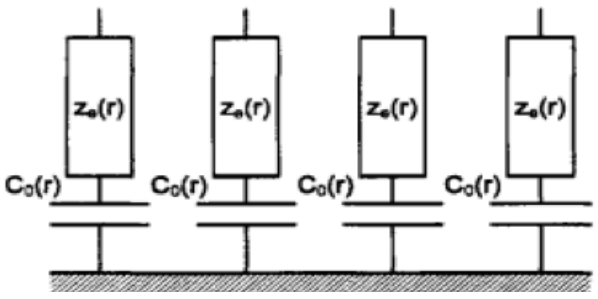

Figure 3.13 Impedance distribution for a blocking electrode [99]

This summation suggests that the CPE or a depressed semicircle can be modeled with multiple *RC* elements or smaller perfect semicircles. The CPE can be treated as an imperfect capacitor for the interfacial capacitance, and for a blocking electrode the effective capacitance is given by

$$C_{eff} = \left[Q R_e^{(1-\alpha)} \right]^{1/\alpha}$$

Another special case is porous electrodes, which are used often in electrochemical systems because of the high effective surface area and greater reactivity with the electrolyte. The cathode in a solid polymer lithium battery is generally a conductive porous electrode consisting of intercalation particles and active carbon, as shown in Figure 3.14a.

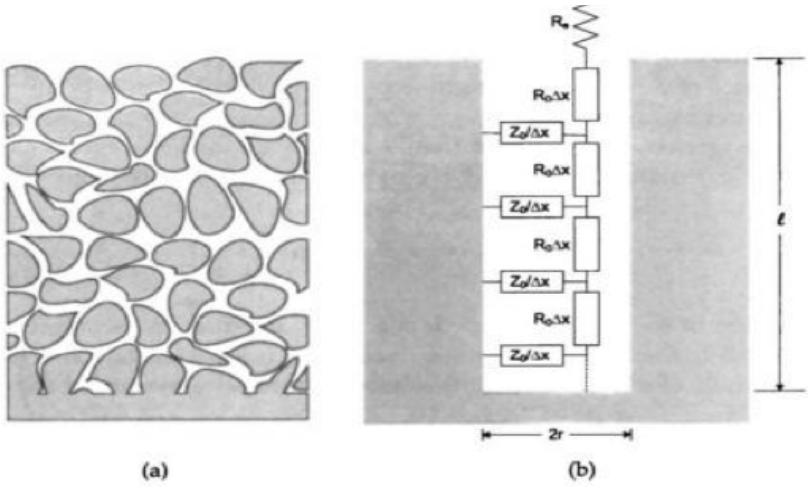

Figure 3.14 Impedance modeling for a porous electrode [99]

The impedance of a porous electrodes, with a distribution of pore diameters and lengths, can be represented using a transmission line, as shown in Figure 3.14b, where R_0 is the resistance of the bulk electrolyte, and Z_0 is the electrolyte-electrode interfacial impedance, which could have CPE behavior. In general both R_0 and Z_0 are

dependent on the distance to the pore wall, and are affected by the presence of any concentration or potential gradient, and the impedance can only be numerically calculated. But in the special case that R_0 and Z_0 are independent of position, the overall impedance of an ensemble of n pores is given by the de Levie impedance

$$Z = R_e + \frac{\sqrt{R_0 Z_0}\coth\left(l\sqrt{\frac{R_0}{Z_0}}\right)}{n}$$

EIS was performed using a frequency response analyzer (FRA), typically a Solartron 1250, 1255, or 1260, to generate a sinusoidal excitation signal (10 mV). This ac signal was superimposed on a dc bias voltage signal generated by a wide-bandwidth potentiostat electrochemical interface (ECI), typically a Solartron 1286. The ECI was connected to the test cell. The response over the scanned frequency range was analyzed by the FRA, and the impedance values were recorded using the software Zplot and Zview. The hardware configuration is shown in Figure 3.15.

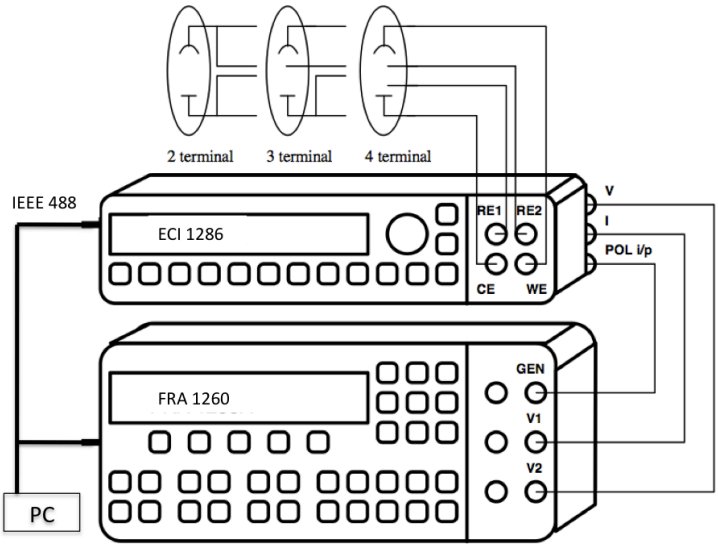

Figure 3.15 EIS hardware configuration [100]

3.5 Results and Discussion

The effect of the presence of lithium salt (LiTFSI) on the segmental motion and crystallinity of the graft copolymer (POEM-g-PDMS at 9:1) was studied, and the DSC plots are shown in Figure 3.16. The pure graft copolymer (GC) shows a T_g near −65 °C, which is from the POEM block, and T_c at −40 °C and T_m at −7 °C, which are the crystallization and melting points of the PDMS block. No crystallization or melting of the POEM was observed, suggesting the 8-unit long PEO brushes are completely amorphous.

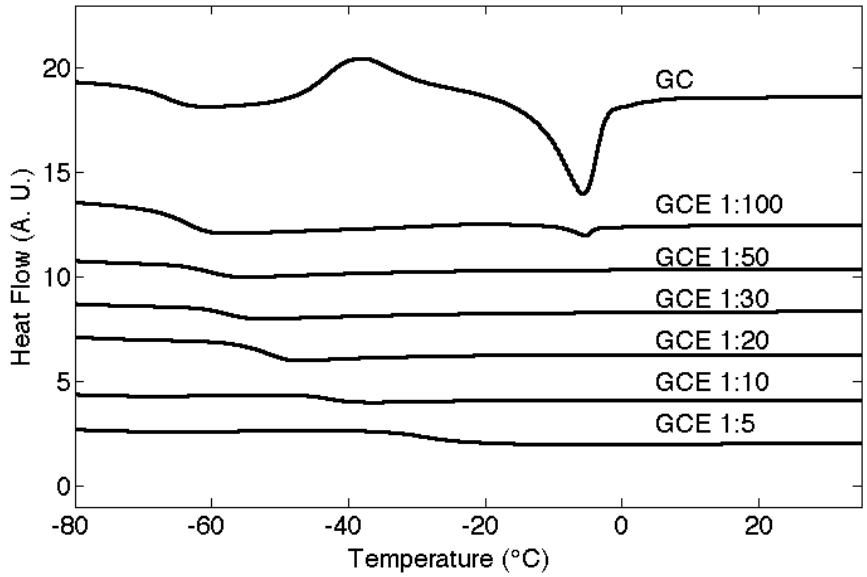

Figure 3.16 Effect of salt concentration on graft copolymer electrolyte (GCE)

As the salt concentration increased from 1:100 (salt : GC) to 1:5, the T_g of the POEM increased from −65 °C to −25 °C, suggesting that the salt interacts with the PEO, and at high concentrations the segmental motion of PEO is reduced. The disappearance of the PDMS crystallization and melting suggests the less flexible POEM block suppresses the crystallinity of the PDMS block. Because both blocks are tethered to the same backbone, the flexibility of one block affects that of the other.

The segmental motion of the PEO brushes is also related to the flexibility of the backbone. POEA and POEM (shown in Figure 3.7) with the same PEO brushes, but differ in one methyl group in the backbone, have different T_gs by 5 °C, as shown in their DSC scans in Figure 3.17. This suggests that having an extra methyl group in the backbone further disrupts the regularity in the graft copolymer and increases the segmental motion in the PEO-containing block.

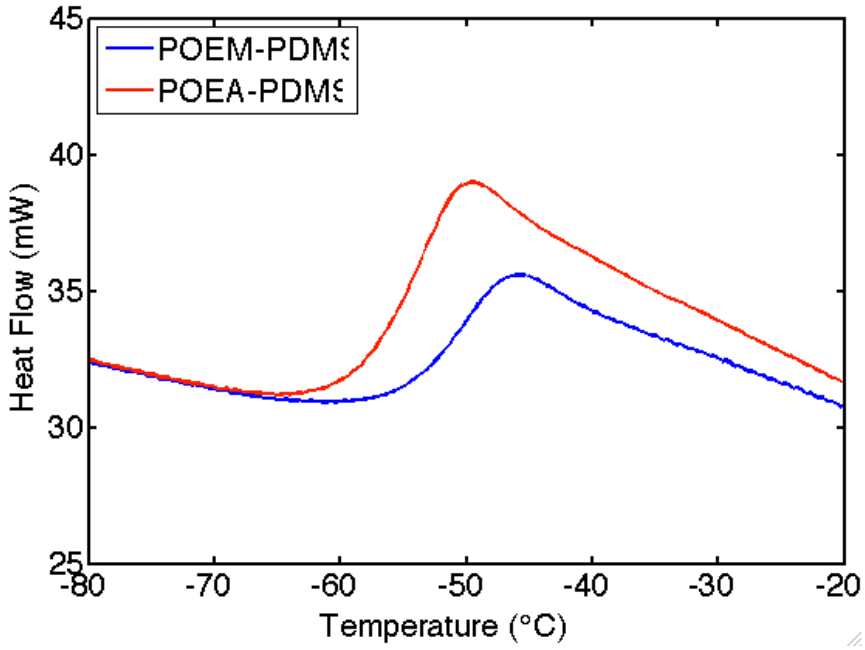

Figure 3.17 Tg of POEM and POEA

Since the PEO brushes in POEA-g-PDMS have a lower T_g than those in POEM-g-PDMS, they are expected to have a higher conductivity based on the VTF equation. The conductivity was measured using the setup in Figure 3.8. The corresponding Randle's equivalent circuit model and theoretical impedance Nyquist plots are shown in Figure 3.18. The semicircle at high frequency is related to properties of the bulk polymer electrolyte, and modeled with an R||C parallel circuit, where R_{elect} is the bulk electrolyte resistance, and C_{geom} is the geometric capacitance between two

metal blocking electrodes. The linear region at low frequency indicates a diffusion-controlled process such as the Warburg impedance (CPE with α=0.5) at the electrolyte-electrode interface, where there is a high charge-transfer resistance characteristic of a blocking electrode [74, 99-102].

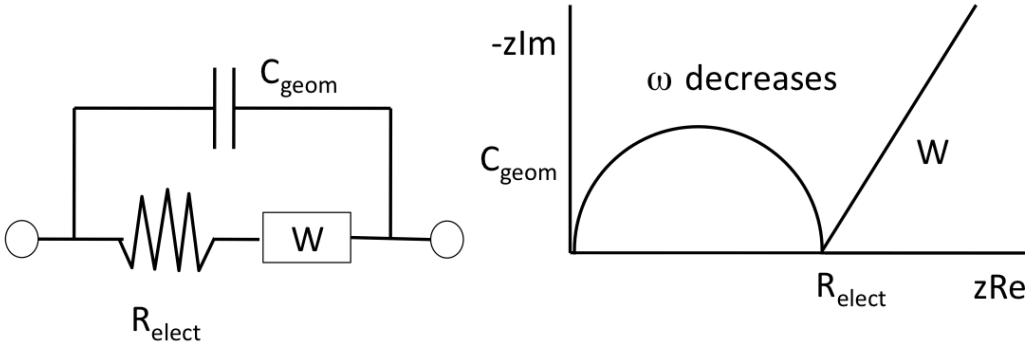

Figure 3.18 Equivalent circuit model for polymer conductivity measurement

Sample Nyquist plots from the two polymers are shown in Figure 3.19, and they agree well with the theoretical Nyquist plot in Figure 3.18. The radii of the semicircles at high frequency were taken as the bulk polymer electrolyte resistance.

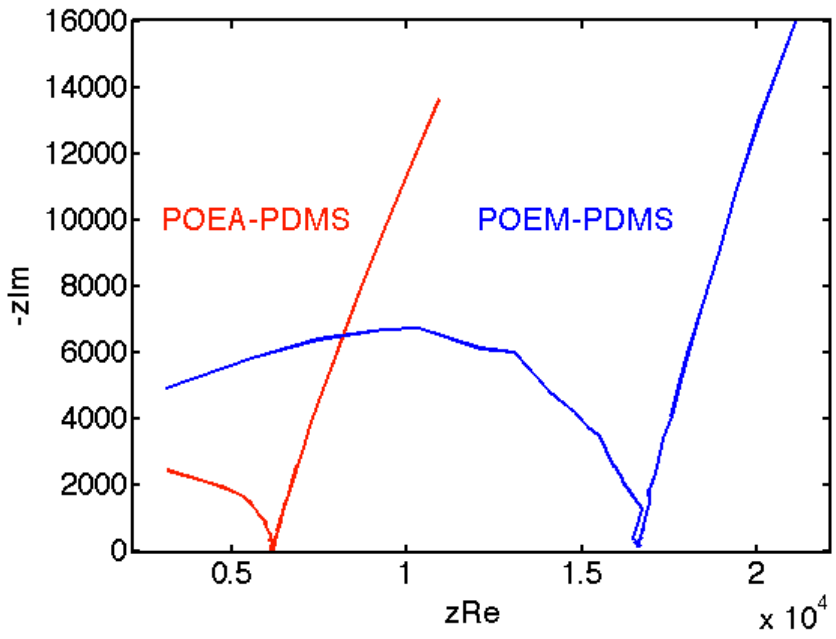

Figure 3.19 Sample Nyquist plots

The conductivity was calculated from the resistance values and the dimension of the spacers. The polymer electrolyte (with LiTFSI salt at Li:EO 1:20) conductivities from room temperature to 200 °C are plotted in Figure 3.20.

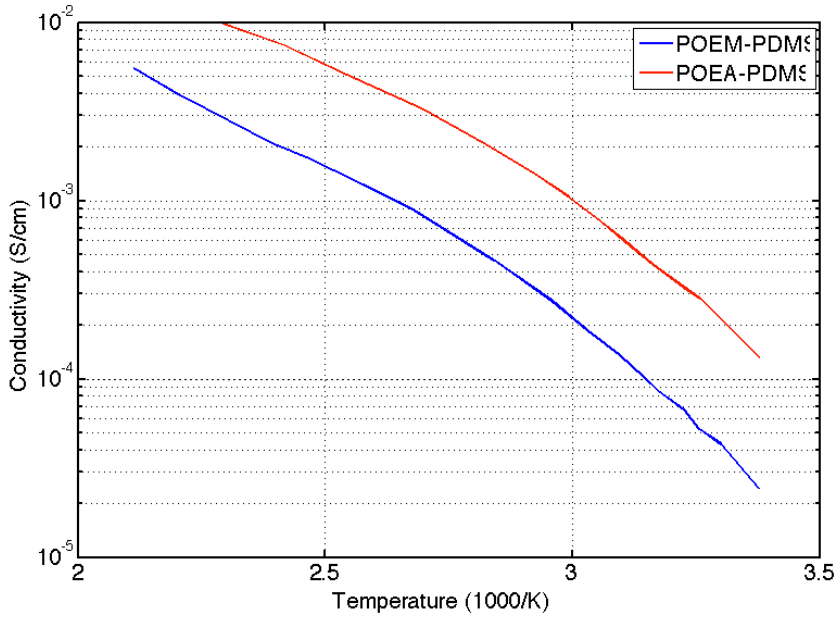

Figure 3.20 Conductivity of POEM and POEA at different temperatures

The convex conductivity curves indicate that the governing relation is VTF instead of Arrhenius. The POEA-based copolymer electrolyte has nearly an order of magnitude improvement in conductivity compared to the POEM-based copolymer electrolyte. Both the conductivity and DSC measurements indicate that the polymer with the lower T_g has greater segmental motion and higher conductivity.

4. Cathode-Electrolyte Interface

The poor wettability between the graft copolymer electrolyte and cathode particles leads to high impedance at the cathode-electrolyte interface, higher than that of the bulk polymer electrolyte and at the anode (lithium metal)-electrolyte interface. The cathode-electrolyte interface was found to be the rate-limiting step in the entire battery. The graft copolymer was used as both the electrolyte and cathode binder to improve the interfacial wetting. Electron microscopy techniques were used to visualize the interface.

4.1 Graft Copolymer as Electrolyte and Binder

In conventional lithium-ion batteries, where organic carbonate liquid electrolyte is used, the cathode binder is a non-conductive polymer, typically polyvinylidene fluoride (PVDF). But due to its low viscosity and high conductivity, the liquid electrolyte is able to penetrate the PVDF matrix, wet the cathode particles ($LiFePO_4$), and provide adequate ion conduction to access all of the cathode storage capacity (Figure 4.1 red). When the liquid electrolyte is replaced with the graft copolymer electrolyte, its solid-nature (infinitely high viscosity) prevents wetting of the PVDF binder matrix, and limits the amount of accessible capacity to only cathode particles near the interface (Figure 4.1 black). This is not a problem for thin binder-free sputtered cathodes, but for coated cathodes with high loading factor, this dramatically reduces the accessible energy density. If a solid polymer electrolyte is used, the cathode binder must also be ion-conductive. To access the full cathode

capacity, the solid polymer needs to be used as both electrolyte and binder (Figure 4.1 blue). Figure 4.1 shows the schematics for the various electrolyte-binder combinations, and their discharge specific capacity profiles. Both using solid polymer electrolyte and the current rate of C/30, but the blue curve exhibits more than 6 times higher capacity and less overpotential than the black curve.

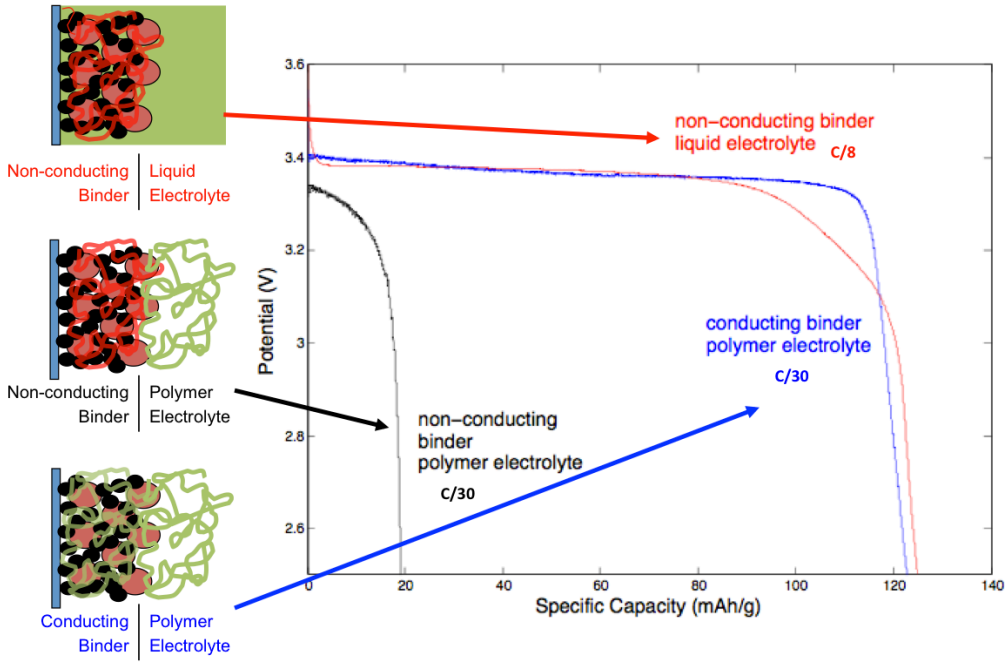

Figure 4.1 Accessible capacities for different electrolyte and binder combinations

The voltage plateau near 3.4V is due to the low miscibility between the $LiFePO_4$ and $FePO_4$ phases in the two-phase electrode.

4.2 Composite Cathode Preparation

To ensure ion conduction throughout the cathode, the graft copolymer electrolyte (GCE) was also used as the binder material replacing the non-ion-

conducting PVDF. The cathode was synthesized by mixing ball-milled $LiFePO_4$ powders (Linyi Gelon New Battery Materials) and carbon black (Super P), and dissolving the mixture in GCE solution at a weight ratio of 5:1:1. The resulting slurry was then sonicated, magnetically stirred to ensure proper mixing, and doctor-bladed at a loading factor of 10 mg/cm^2 onto aluminum foil. The slurry was heated to 80 °C (open-cap) while stirred right before doctor-blading, to ensure better lamination to aluminum. The composite cathode was dried in a vacuum oven at 80 °C overnight to remove the residual THF and moisture.

The composite cathode was then transported into an argon-filled glovebox, where it was punched into small discs (area=1.4 cm^2) using a high-precision electrode cutter EL-CUT (EL-CELL). Pure GCE solution (POEM-g-PDMS, LiTFSI, both dissolved in THF) was then drop-casted onto the electrode discs to form the electrolyte layer. The final cathode-electrolyte discs were heated on a hot plate inside the glovebox to evaporate the THF, and assembled into CR2032 coin cells along with equal-sized GCE-coated metallic lithium discs (Sigma-Aldrich, 0.75 mm thick) using a manual closing tool (Hohsen). The cell schematic is shown in Figure 4.2, where the gray particles represent $LiFePO_4$, the black particles represent carbon, the blue "spaghetti" represents the GCE, and the anode is lithium metal.

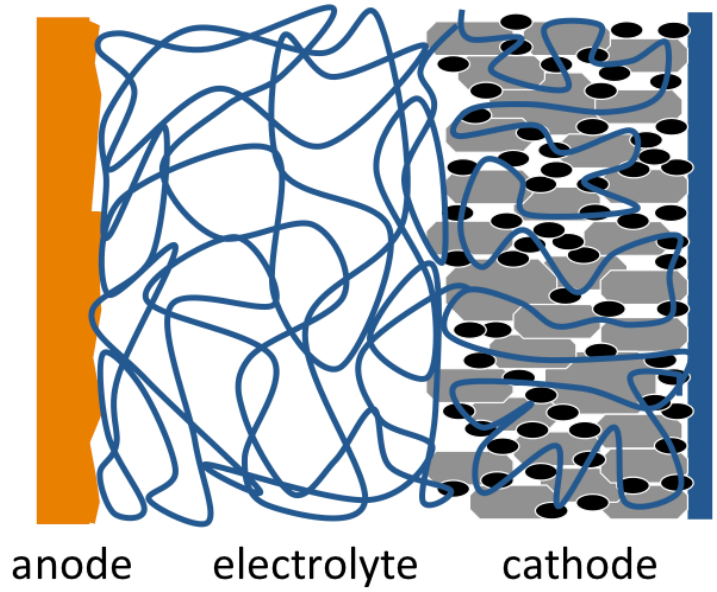

Figure 4.2 Schematic of a solid polymer lithium battery

A second set of cells comprised of the same $LiFePO_4$ powders and lithium metal anode, but PVDF binder resin (Kynar), PVDF separator (Celgard), and liquid electrolyte of 1 M $LiPF_6$ in EC:DMC at 1:1 ratio (LP30, Merck), was also assembled to compare the performance. All assembly were done in a glovebox with a dew point of −80 °C. A 32-channel Maccor 4000 battery tester was used for the cycling test.

4.3 Room Temperature Performance

The room temperature cell cycling performance is shown in Figure 4.3. The left plot shows the charge and discharge profiles of cells with conventional liquid electrolyte (LP30) at 15 mA/g, and graft copolymer electrolyte/binder (GCE) at 10 mA/g. The $LiFePO_4$/GCE/Li curves show greater overpotential than the $LiFePO_4$/LP30/Li curves on both charge and discharge, due to higher interfacial impedance and electrolyte ohmic resistance. Despite higher impedance, since the

GCE is used as both electrolyte and binder, ion conduction is provided to all of the cathode particles, and nearly the entire practical specific capacity (150 mAh/g) was accessible. The theoretical specific capacity of 170 mAh/g is not achieved since it is limited by lithium diffusion within $LiFePO_4$ particles, which is low at room temperatures. The cycling capacities for the first 50 deep cycles are shown in the right plot. The energy efficiencies during the first 5 cycles are low (large charge/discharge capacity ratio), possibly due to the reversible capacity loss related to the formation of passivation layer on lithium anode. The passivation film could result from reactions between lithium metal and residual THF solvent of the $CF_3SO_3^-$ anions, which are known to produce LiF species.

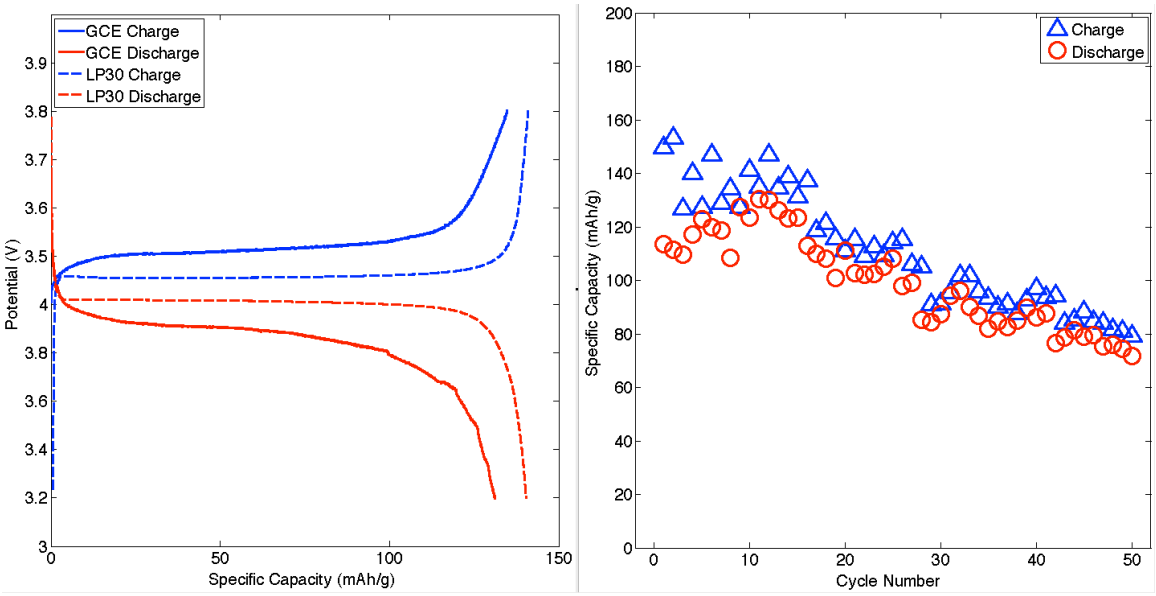

Figure 4.3 Room temperature cycling [103]

4.4 Full Cell and Symmetric Cell EIS Studies

Two-electrode EIS scans of the full cell (Li/$LiFePO_4$) and symmetric cells (Li/Li and $LiFePO_4$/$LiFePO_4$) are shown in Figure 4.4. The geometric dimension of the polymer electrolyte was kept the same throughout, and the $LiFePO_4$ cathodes employed graft copolymer binder. The Li/Li Nyquist plot (shown in red), because the electrodes are planar and polarizable, exhibits two semicircles. The one at high frequency is due to the bulk polymer electrolyte, and the second one at low frequency is due to faradaic charge transfer resistance and double layer capacitance.

In the Li/$LiFePO_4$ and $LiFePO_4$/$LiFePO_4$ Nyquist plots (shown in black and blue), because the $LiFePO_4$ cathode is a porous electrode, they exhibit two depressed semicircles (CPE behavior, a distribution of time constants) in both the high frequency electrolyte region and low frequency interface region. Even though the geometric dimension of the graft copolymer electrolyte layer is the same, the same polymer was also used as the cathode binder; the effective dimension is different, and leading to difference in the amplitudes of the semicircles. They also exhibit diffusion processes at low frequency, characteristic of porous electrodes.

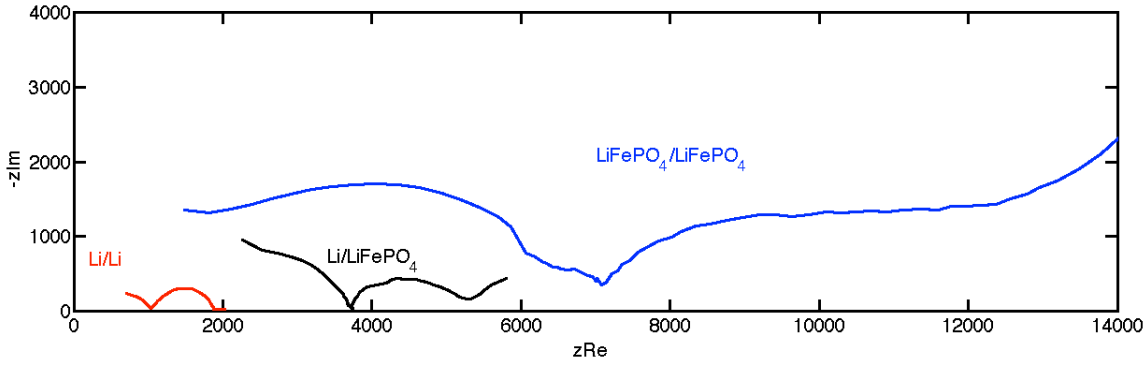

Figure 4.4 Full cell and symmetric cell impedance data

The overall impedance of a symmetric cell consisting of two porous cathodes is higher than that of a symmetric cell consisting of two planar anodes. Figure 4.4 points out that the dominant impedance contributor in a solid polymer lithium battery is at the interface between polymer electrolyte and cathode particles.

This cathode-electrolyte interface limit is related to lithium ion diffusion within the structure of $LiFePO_4$. The olivine $LiFePO_4$ (shown in Figure 4.5) is formed by FeO_6 octahedrons sharing O corners with PO_4 tetrahedrons, and LiO_6 forming a linear chain of edge-sharing octahedrons parallel to the *b* axis. Both $LiFePO_4$ and the deintercalated $FePO_4$ have Pmnb space groups, their lattice constants are (a=6.008 Å, b=10.334 Å, and c=4.693 Å) and (a=5.792 Å, b=9.821 Å, and c=4.788 Å), and their unit lattice volumes are 291.4 $Å^3$ and 272.4 $Å^3$ respectively [104-108].

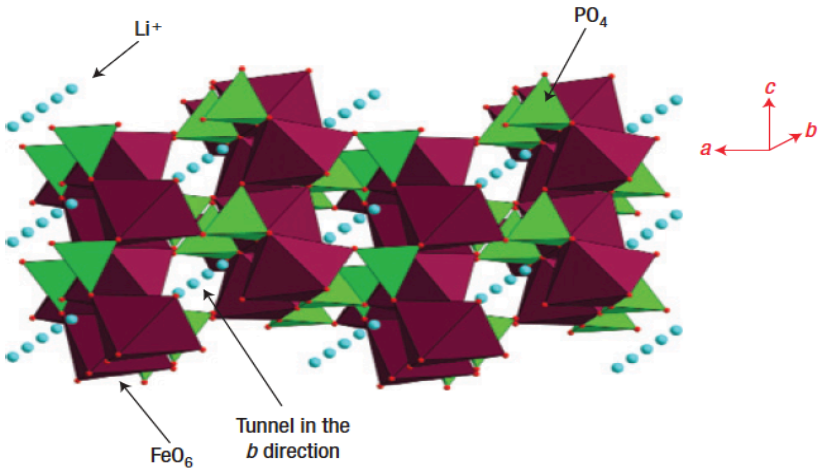

Figure 4.5 Structure of $LiFePO_4$ [104]

Unlike other $LiMO_2$ cathodes, where lithium ions have 2D or 3D diffusion pathways, lithium diffusion in $LiFePO_4$ only occurs in one-dimensional tunnels and proceeds through a two-phase reaction with the existence of a narrow solid solution in the vicinity of the endmembers $LiFePO_4$ and $FePO_4$, both are poor ionic (lithium

ion diffusion coefficient is 10^{-14} to 10^{-16} cm^2/sec) and electronic (10^{-9} S/cm, compared to 10^{-3} S/cm for $LiCoO_2$ and 10^{-5} S/cm for $LiMn_2O_4$) conductors. The 1D tunnels can also be blocked by defects or impurities. Both lithium ions and electrons need to move simultaneously during the intercalation of deintercalation processes. The low electron conductivity is a result of low mobility due to strong binding to lithium vacancies in $FePO_4$ or lithium ions in $LiFePO_4$, thus a thin carbon coating (5 nm) is applied to $LiFePO_4$ to improve the electronic conductivity [27, 30, 109-114].

In order to have fast charge transfer, it is not enough to have the polymer electrolyte be in contact with $LiFePO_4$ particles, but the lithium conduction pathway in the polymer must be aligned with the pathway in $LiFePO_4$. This is easily accomplished in liquid electrolyte, which wets the entire particle surface, whereas polymer electrolyte only partially wets the particle surface.

If polymers with higher conductivity and greater flexibility are used as cathode binder, they can reduce interfacial impedance. Figure 4.6 compares the impedances of two different $LiFePO_4$/$LiFePO_4$ symmetric cells. Both have the same POEM-g-PDMS electrolytes, but one has POEM-g-PDMS binder (blue), and another has POEA-g-PDMS binder (red). They have the same high frequency bulk electrolyte components, but the one with POEA-g-PDMS binder has much smaller low frequency interfacial components. Figure 4.6 shows that POEA-g-PDMS reduces cathode-electrolyte interfacial impedance by providing higher conductivity and better particle surface wetting, which increases lithium ion diffusion across the surface towards the (010) facet.

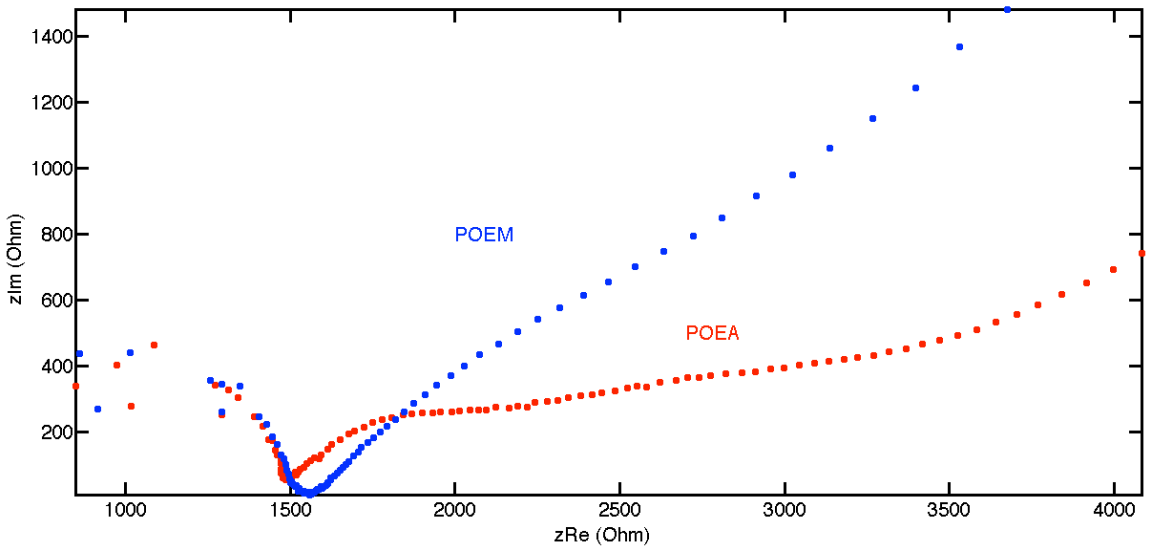

Figure 4.6 $LiFePO_4$/$LiFePO_4$ symmetric cells with different binder

4.5 Electron Microscopy of Composite Cathodes

4.5.1 SEM Images

The SEM of the full cell cross section ($LiFePO_4$/GCE/Li) was taken using a Zeiss Supra55VP field emission SEM. The layered structure in Figure 4.7 clearly shows the aluminum substrate, which was used as the current collector; the composite cathode, which consisted of the active material particles ($LiFePO_4$), binder (GCE), and conductive carbon; the GCE electrolyte; and the lithium metal anode. The "waterfall" lines on lithium metal are from the cutting.

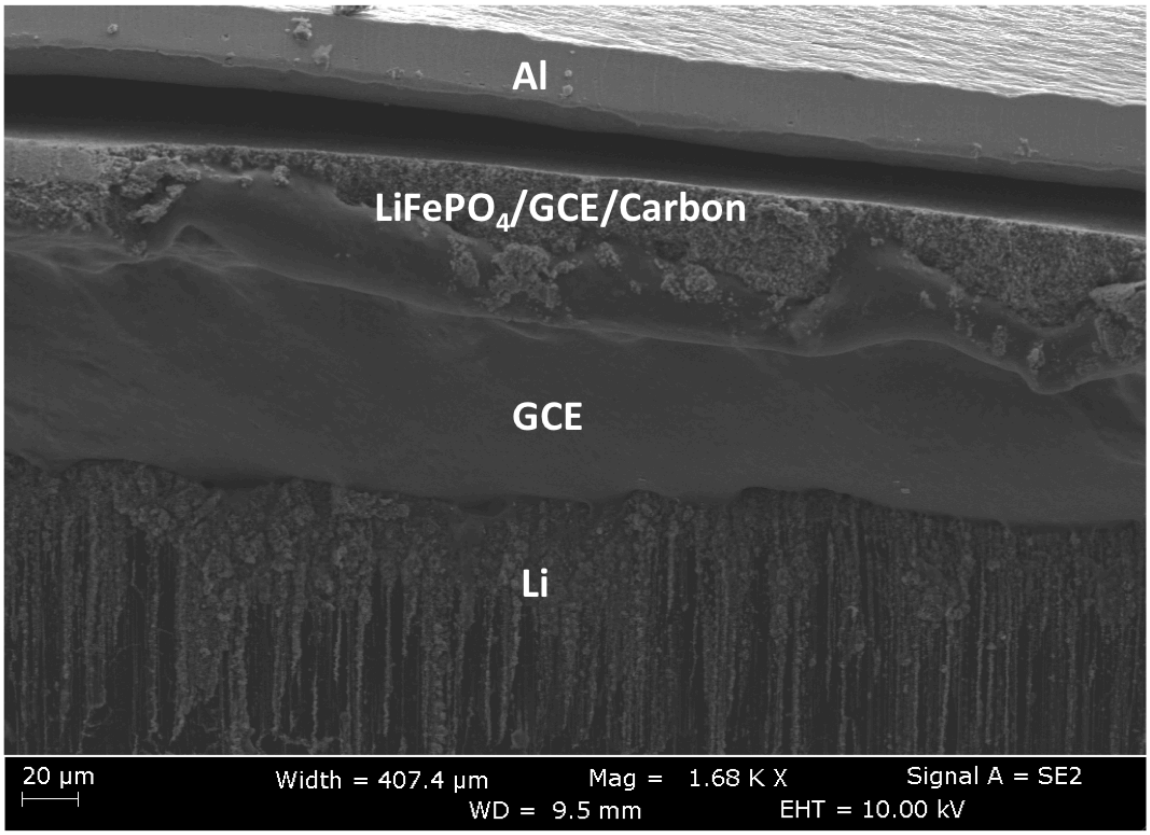

Figure 4.7 $LiFePO_4$/GCE/Li cross section SEM

A high-resolution SEM EDAX elemental analysis of the composite cathode was done using a Zeiss Ultra55 field emission SEM equipped with an EDS detector, and is shown in Figure 4.8. The SE2 image shows the cathode particles coated with the GCE binder, as indicated by the soft edges. The carbon signature is from the carbon particles, the carbon coating on $LiFePO_4$, and the carbon in the polymer. The iron and phosphorous are from the $LiFePO_4$, and the silicon is from the PDMS block of the GCE. This macroscopically shows that the particles are connected together through an ion-conducting matrix.

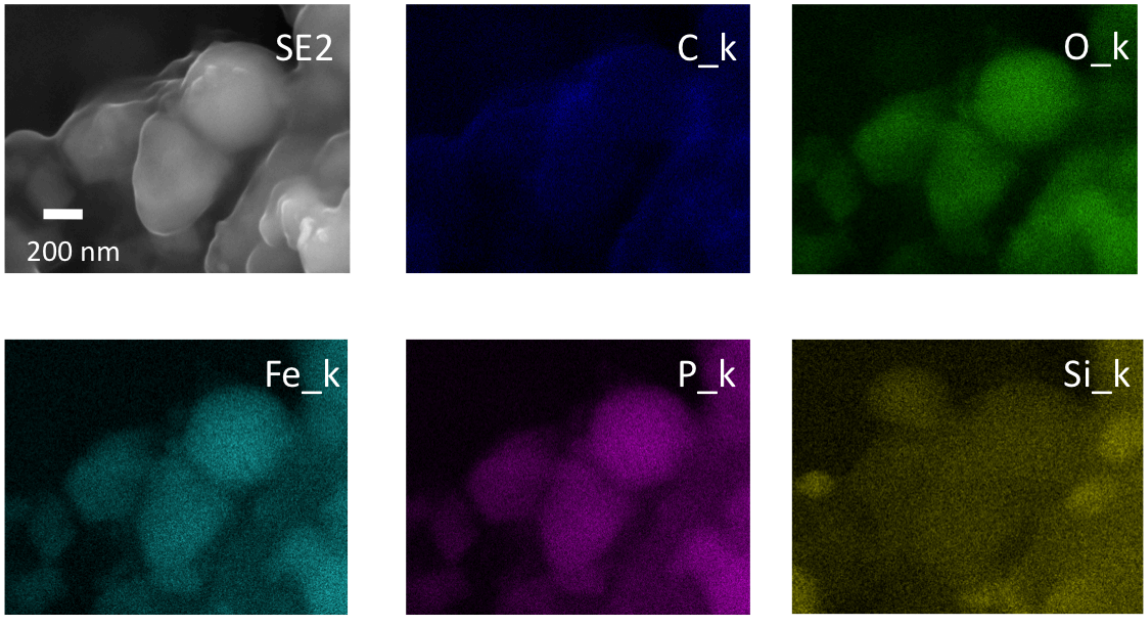

Figure 4.8 SEM EDAX of composite cathode

4.5.2 FIB TEM Sample Preparation

To further investigate the interface between the cathode particles and the electrolyte polymer, higher resolution microscopy was needed. HRTEM was performed on thin composite cathode samples. Several sample preparation techniques were experimented, including directly drop casting diluted cathode slurry onto copper grids, cryo ultramicrotome, and focused ion beam (FIB). Due to the unique mechanical property of the composite cathode, the $LiFePO_4$ particles are as hard as metallic and ceramic samples, the polymer binder is as soft as biological samples, and these two types of samples have very different TEM sample preparation techniques, finding one technique that is suitable for both was not straightforward. But FIB was eventually selected as it produced a sample thin and large enough for HRTEM.

The FIB sample preparation was done with a Zeiss NVision 40 Dual Beam FIB imaging system equipped with an Omniprobe Total Release system. The dual beam FIB comprises of a standard field emission SEM platform (like the Supra or Ultra); a FIB column providing a Ga ion beam (generated from a Ga liquid metal ion source) for milling and imaging; and a gas injection system for conductor deposition, insulator deposition or gas assisted etching, and the available sources include carbon, platinum, tungsten, and SiO_2 for deposition, and water and XeF_2 for etching. Both the SEM and FIB needed to be in focus and aligned, and the eucentric height and coincidence were calibrated. A special SEM holder for the cathode sample, TEM grid, and Omniprobe in-situ needle exchange cassette was used.

The in-situ FIB TEM sample preparation process is shown in Figure 4.9. Because the sample is sensitive to beam damage, a layer of carbon was deposited on the region-of-interest (target). A U-shaped cut that partially surrounds the target (less then 300 nm in thickness) was milled on the sample, and then a straight cut that intersects the first cut from underneath the target was milled and produced a wedge-shape target (Figure 4.9a), where the "waterfall" lines are clearly visible.

Then the target was attached to the Omniprobe's AutoProbe 200 chamber-mounted nanomanipulator by depositing tungsten at the target-nanomanipulator joint. The target was detached from the cathode sample by milling through the last target-cathode joint, carefully lifted out of the cathode sample and transported to an Omniprobe lift-out TEM grid, where the target was attached by depositing tungsten at the target-grid joint (Figure 4.9b-c). Once the target was attached to the grid, it was detached from the nanomanipulator by milling through the target-

nanomanipulator joint. The target was further thinned using FIB until its thickness was less than 100 nm (Figure 4.9d). The darker regions in Figure 8d are the $LiFePO_4$ particles and the lighter regions are the polymer binder. The layered tungsten deposition at the joint is also visible. The final grid was removed from the FIB chamber and mounted on a TEM grid holder for imaging.

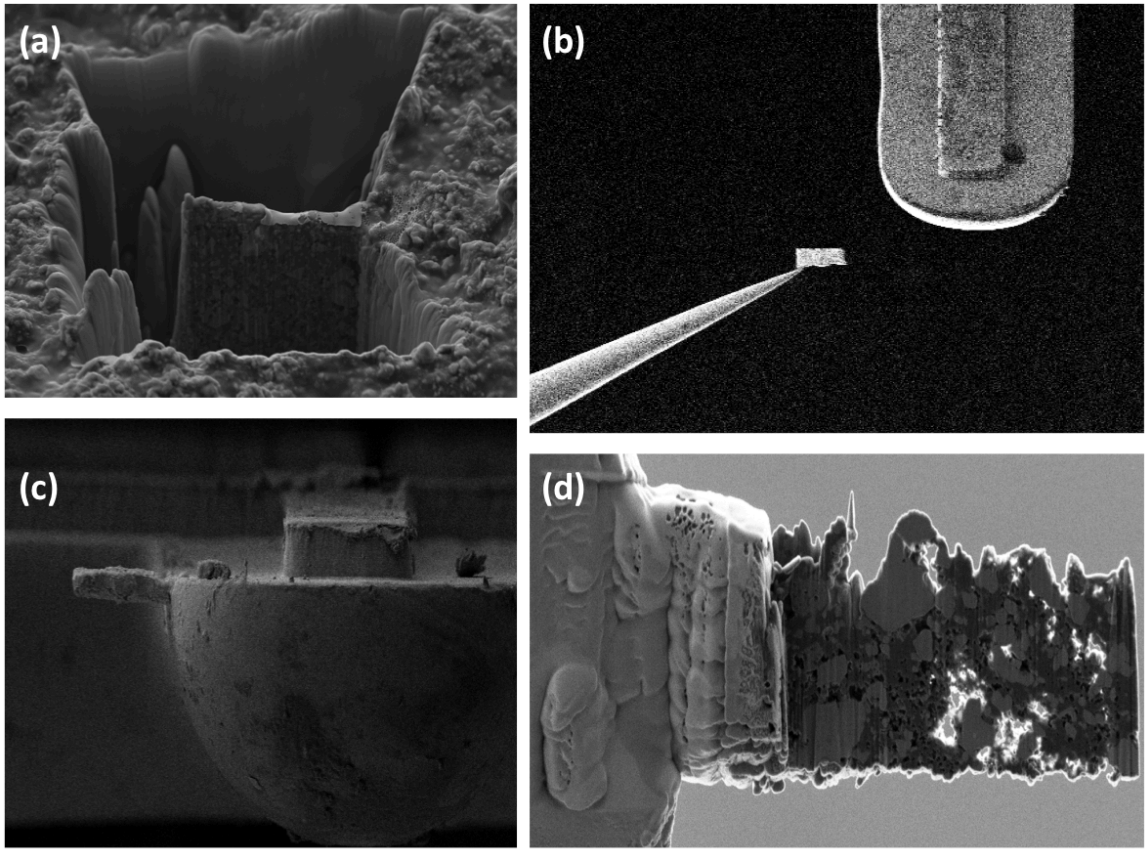

Figure 4.9 TEM sample preparation using FIB

There were some irradiation damage to the polymer due to the high energy Ga ion beam, it would have been better to cryogenically freeze the sample while performing FIB, but that was not available.

4.5.3 TEM Images

TEM images of $LiFePO_4$/C/GCE composite sample were collected using a JEOL 2010 with a field emission gun operating at 200 kV and capable of 0.19 nm lattice resolution (shown in Figure 4.10a, c, and d). High resolution TEM of $LiFePO_4$/C particles was collected with a Zeiss Libra 200 with aberration correction operating at 200 kV and capable of 0.7 Å resolution (shown in Figure 4.10b).

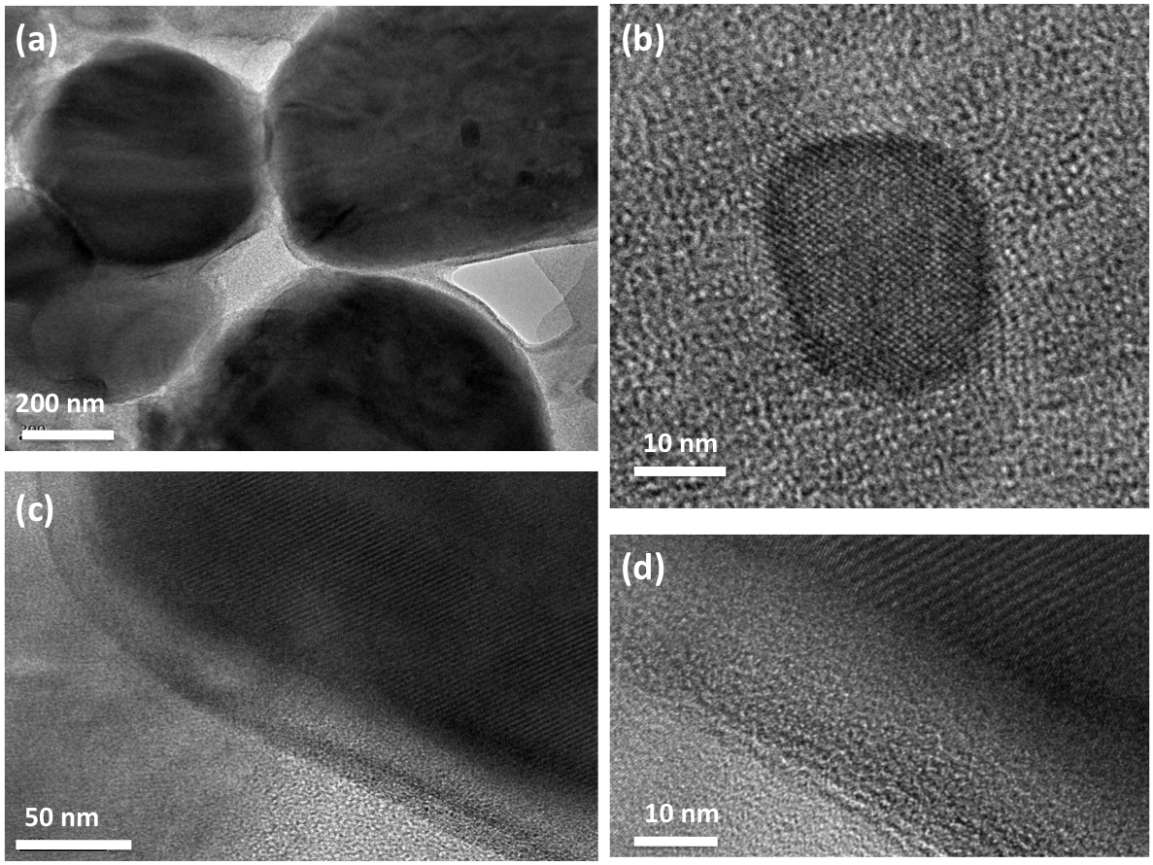

Figure 4.10 High-resolution TEM images of the composite cathode

Figure 4.10a clearly shows $LiFePO_4$ particles (average particle size 700 nm) embedded in a GCE polymer matrix, which appears as a lighter colored surface coating. Figure 4.10b shows a nanosized $LiFePO_4$ particle with its lattice structures and a 3 to 5 nm thick coating of amorphous carbon on the surface (carbon-coated

$LiFePO_4$ particles were purchased from the supplier). Figure 4.10c and d show the interface between the GCE surface coating and the $LiFePO_4$ particles. The surface coating is 20 nm thick, and the lithium ion diffusion channels (010) are clearly visible in Figure 4.10d.

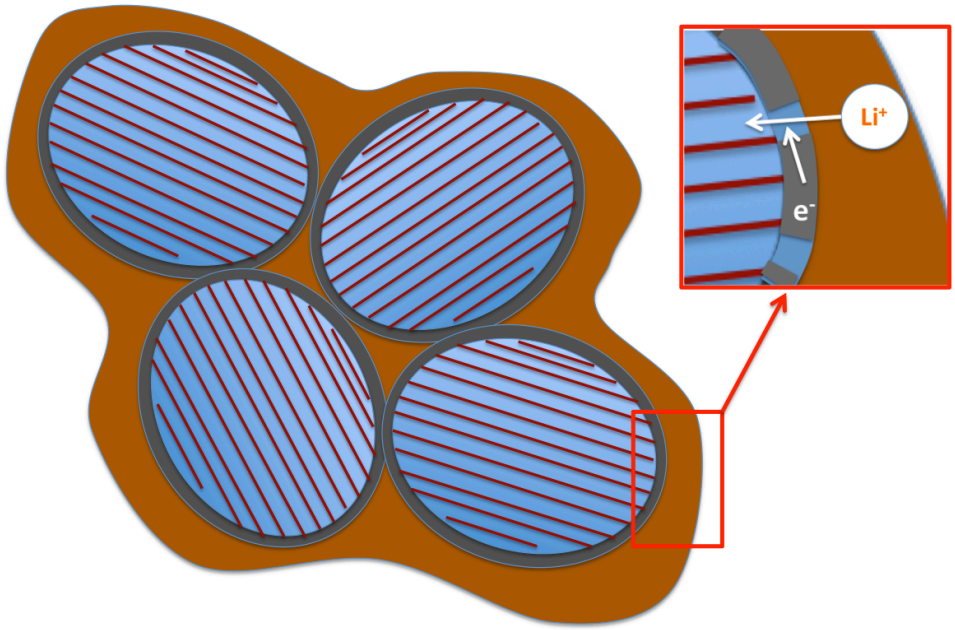

Figure 4.11 Conduction in GCE and carbon-coated $LiFePO_4$ particles

The TEM images confirm the surface coating of the particles by the GCE. We can extrapolate a schematic model (Figure 4.11) for lithium ion intercalation in the $LiFePO_4$/C/GCE composite cathode. GCE transports a lithium ion to the particle surface, and the ion meets with a compensating electron transported by the porous amorphous carbon coating. Using GCE as the cathode binder greatly reduces the charge transfer impedance at the cathode-electrolyte interface.

5. High Temperature Performance

In Chapter 3, we improved the polymer electrolyte conductivity by almost an order of magnitude. In Chapter 4, we reduced the cathode-electrolyte interfacial impedance. In both cases, we dramatically improved the rate capability of the battery. However, the main advantage of the solid polymer lithium battery is in high temperature performance. This chapter is the biggest and most important contribution of this thesis. This is the first time that anyone has ever demonstrated the cycling of a rechargeable lithium battery from room temperature up to 200 °C.

5.1 Introduction to Oil Drilling Batteries

One of the main applications for high temperature lithium battery is in oil drilling. This is a highly specialized field. While the total worldwide market for oil drilling batteries in 2011 was about $100 million, it is expanding fast due to growing global demand for oil and gas, rising oil price, increasing popularity of unconventional conventional fuels such as shale gas, and the emergence of new drilling technologies including horizontal and deep well drilling. Compared to batteries in the cutthroat and high-volume consumer electronics and electric vehicles markets, which are projected to be worth $56 billion by 2017 and $25 billion by 2020 respectively, the mission-critical oil drilling market has lower volume, much higher premium, and is more receptive to new battery technologies.

Near the drill tip (typically 30 to 50 feet away), there are electronics and sensors used for recording geological data, and these need to be powered by

batteries. The applications include measuring-while-drilling (MWD) and logging-while-drilling (LWD). A schematic of the drilling batteries is shown in Figure 5.1, and the inset shows the cylindrical-shaped batteries strung together in series and parallel and packed in a hollow pressurized stainless steel vessel along with other equipments. The center of the vessel is left hollow to allow for mudflow. These batteries must operate in the extremely hostile downhole environment, where there is high vibration and the temperature can reach up to 200 °C.

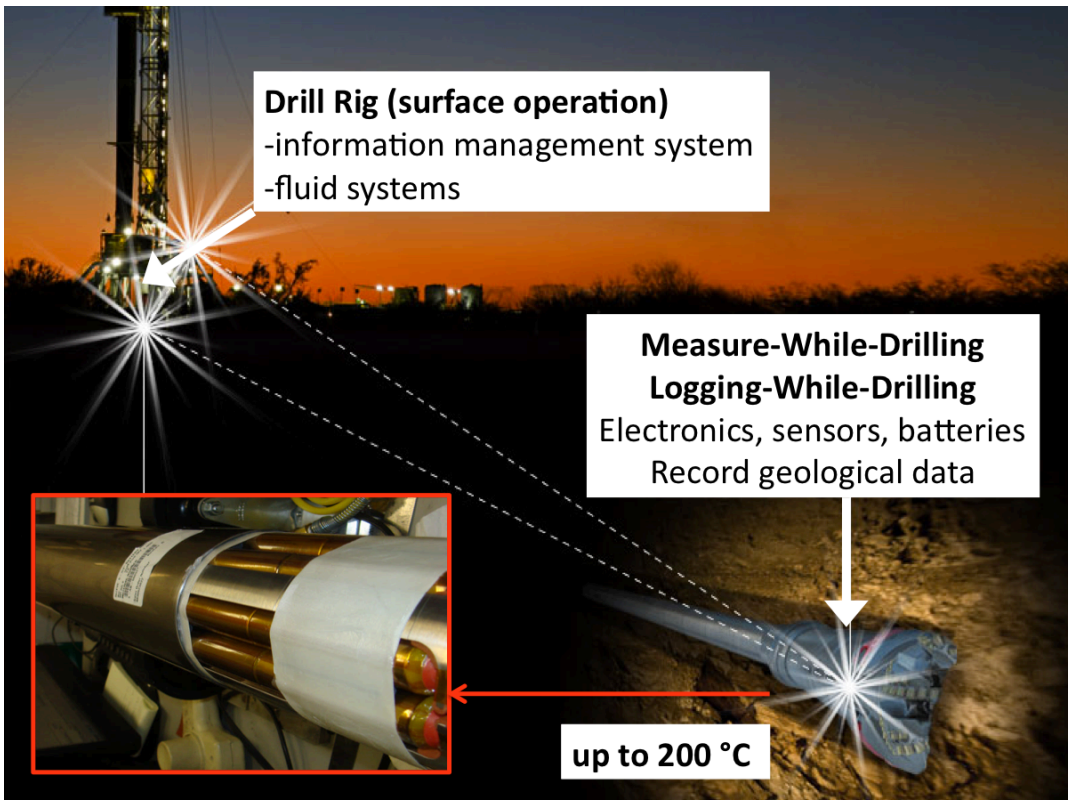

Figure 5.1 Batteries for downhole oil drilling

The battery that the industry currently uses is lithium thionyl chloride ($LiSOCl_2$), which is primary, contains explosive and corrosive materials that are prone to leaking, and is a HAZMAT item, which can only be transported using ships and requires special documents. In oil drilling, battery-related accidents are costly

and happen often. Generally, it costs $2 million to bring up the drill equipments to the surface to replace the battery. It costs $1 million a day to rent an onshore rig, and $10 million for an offshore rig. Damages to the equipments in the vicinity cost $3 million each, and the cleanup typically takes 30 manhours. If it disables the blowout prevention system, it could also lead to major disasters like the BP oil spill. In addition, there are also body injuries. These accidents happen 4 to 5 times a year, according to a Schlumberger field service engineer.

The solid polymer lithium battery can dramatically improve the safety and reliability in storage and transportation. In addition, it provides the bonus benefit of rechargeability. This is the future of oil drilling, where instead of bringing up the entire apparatus to the surface every time the battery needs to be replaced, the battery can be recharged downhole while drilling by harvesting the mud fluid motion using the generator at the drill tip, thus dramatically improving productivity.

Due to the limited real estate in downhole drilling equipment, there is a high requirement on the volumetric energy density of the battery. Like most primary batteries, $LiSOCl_2$ has a high energy density of 975 Wh/L, and the rechargeable solid polymer lithium battery ($LiFePO_4$/GCE/Li) only has an energy density of 354 Wh/L. While recharging-while-drilling downhole can potentially make up the difference, it is not yet the industry practice. However, the low energy density is due to the current cathode choice, and we can replace $LiFePO_4$ with higher energy cathodes such as $Li(Ni_xMn_yCo_z)O_2$, which has more than twice the energy density. Also $LiSOCl_2$ has a low useable energy density due to the difficulty with extrapolating its state of charge based on its cell voltage.

In this thesis, all of the experiments were performed with $LiFePO_4$ as the default cathode, with the understanding that the energy density can be improved by switching to other intercalation or conversion cathodes, but they are not investigated here. Also lithium metal was used as the default anode, with the understanding that the thermal stability can be improved by switching to lithium-aluminum or magnesium alloys or graphite, and they are not investigated here either. The objective is to demonstrate the high temperature capability of the solid polymer electrolyte, which is the limiting factor for most batteries.

5.2 Experimental Setup for High Temperature Testing

The high temperature testing setup is shown in Figure 5.2, where the coin cells were wrapped in a resistive heating tape, and the temperature of each cell was monitored using a type-K thermocouple.

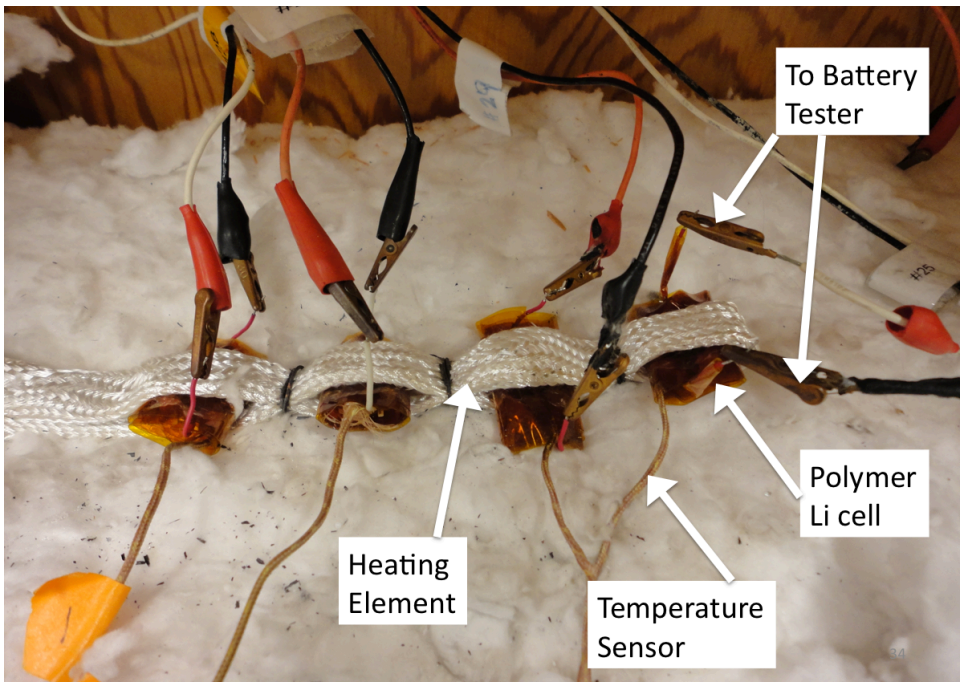

Figure 5.2 High temperature testing setup

In all high temperature experiments, the heating rate was less than 5 °C/min, and the temperature fluctuation was held at less than 2 °C using a Glas-Col temperature controller. Before the high temperature experiments, all cells were "conditioned" at room temperature by cycling them 3 times to form a passivation layer on lithium metal and allow the cells to equilibrate. The cycling was done using a Maccor 4000 battery tester. Regular coin cell casings could not be used for high temperature testing because of their polypropylene (PP) gasket, which is rated for a maximum temperature of 120 °C. Instead, special coin cell casings with Teflon gaskets, rated for 327 °C, were used. Also high temperature coin cell holders (rated for 280 °C), silicon-coated wire (rated for 210 °C), and high temperature solder with a Pd/Sn ratio of 6/4 (rated for 230 °C) were used (shown in Figure 5.3).

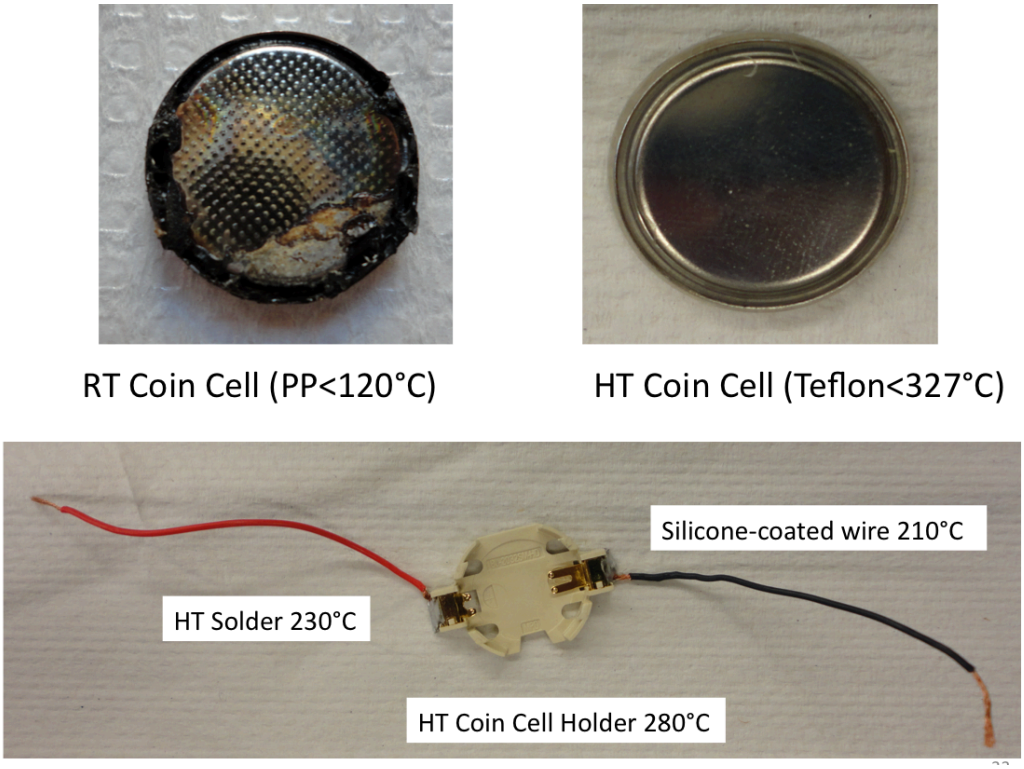

Figure 5.3 High temperature coin cell casings

5.3 Results and Discussion

The open circuit voltage of a fully charged cell was monitored during heating, and recorded in Figure 5.4, where the red is the OCV and the blue is the temperature.

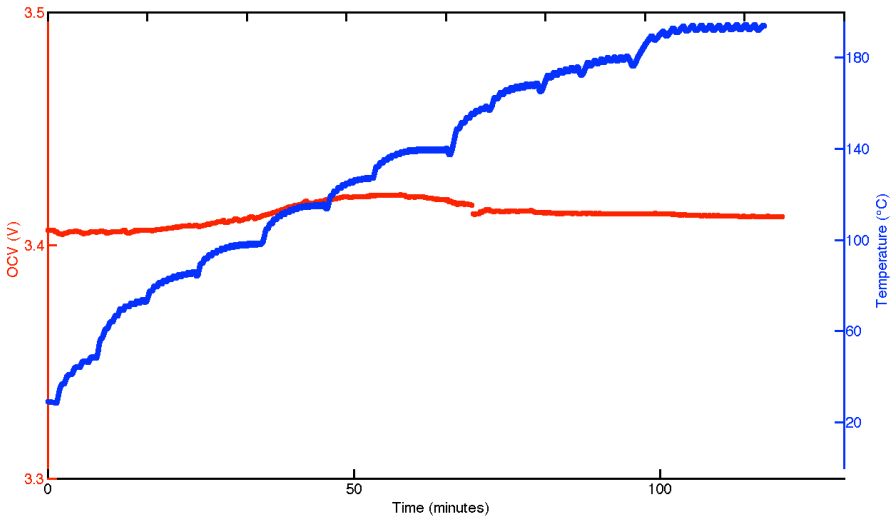

Figure 5.4 Cell voltage during heating

The temperature profile indicates that the heating was ramped incrementally and slowly enough to allow the thermal processes in the cell to equilibrate. The OCV remains constant during the heating, indicating that there is no self-discharge induced by thermal expansion.

5.3.1 Isothermal Cycling at High Temperatures

Figure 5.5 shows the isothermal cycling of the cell at 60 °C at 2 different c-rates, C and C/2. This is already the upper temperature limit of conventional lithium-ion batteries with carbonate liquid electrolytes. While the achievable specific capacity at C/2 is higher than at C, the gap is small, indicating good rate

capability of the solid polymer lithium battery at 60 °C. More than 100 cycles were achieved with little capacity fade at both c-rates. At C/2, almost all of the practical specific capacity (150 mAh/g) can be accessed, suggesting that it has the potential for automotive applications such as plug-in BEVs, where more than 90% charge and discharge must be achieved at C/2 current.

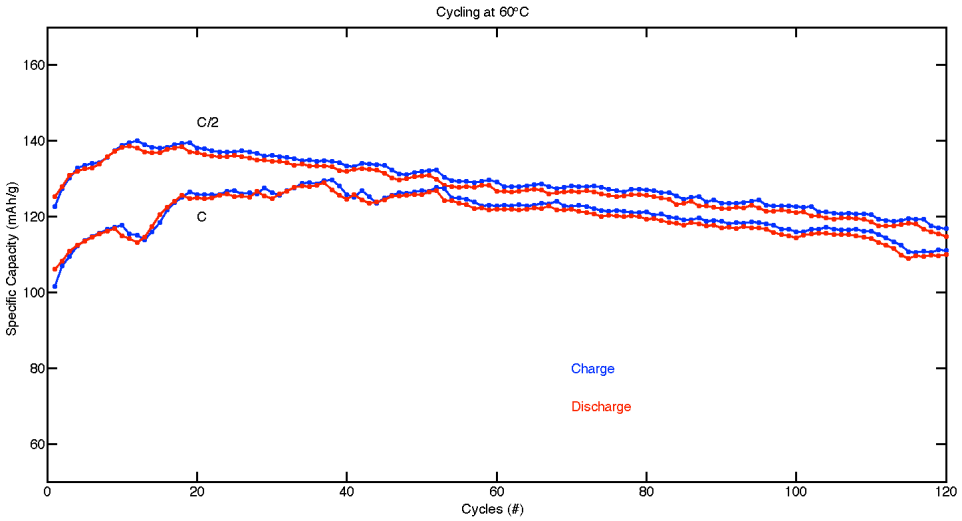

Figure 5.5 Isothermal cycling at 60 °C

Figure 5.6 shows the isothermal cycling of the cell at 120 °C at C/2. The charge and discharge voltage profiles in Figure 5.6a are comparable to that of the commercial $LiFePO_4$/LP30/Li cells at room temperature with low overpotential. Moreover, due to the increased lithium ion mobility in $LiFePO_4/FePO_4$ mixed phases at elevated temperature, nearly the full theoretical specific capacity of 170 mAh/g is achieved. Figure 5.6b shows the charge and discharge capacity at 120 °C with capacity retention exceeding 100 mAh/g for 30 cycles. In Figure 5.6b, we observe decreasing energy efficiency after the first few cycles due to an increasing charge capacity and steady fade in discharge capacity, consistent with the results reported

by Andersson el al [115]. Since the charge capacity of $LiFePO_4$ cannot exceed 170 mAh/g, the excessive capacity must be ascribed to other electron consuming reactions, such as the formation of a passivation layer. Temperature-induced volume expansion of metallic lithium may exert mechanical stress on the passivation film, leading to cracking and the exposure of fresh lithium to the electrolyte.

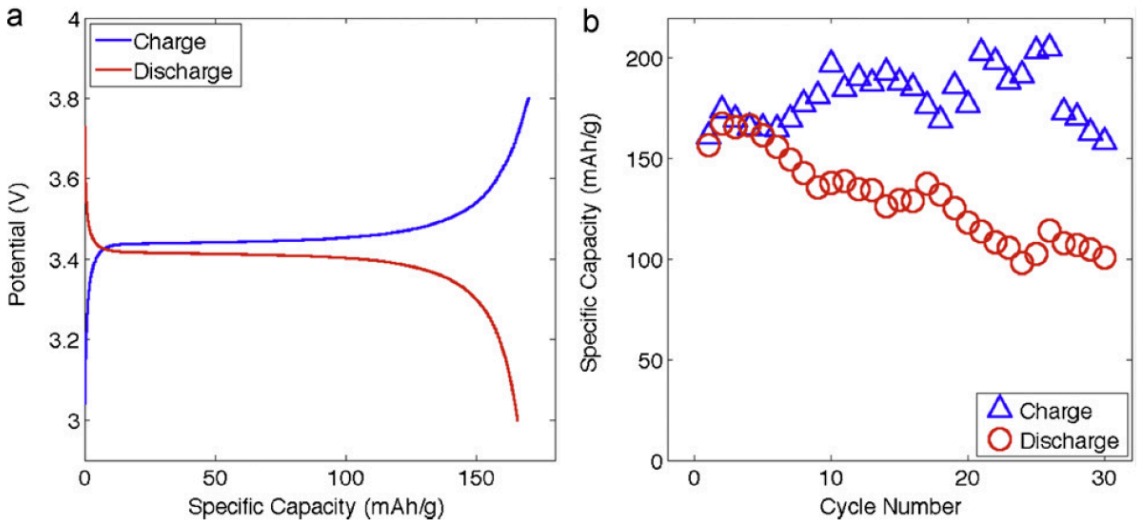

Figure 5.6 Isothermal cycling at 120 °C [103]

Figure 5.7 shows the isothermal cycling of the cell at 170 °C at C. This has never been demonstrated before based on our literature search [116-125]. This is very close to the melting point of lithium metal, which is 181 °C. The first two cycles are at room temperature at C/10, and they have much lower capacity due to the lower rate capability. The cycling capacities at 170 °C remain above the room temperature level for 7 cycles. We attribute the capacity fade to the reactivity of lithium metal and instability of the passivation film at this temperature (more discussion on this in Chapter 6).

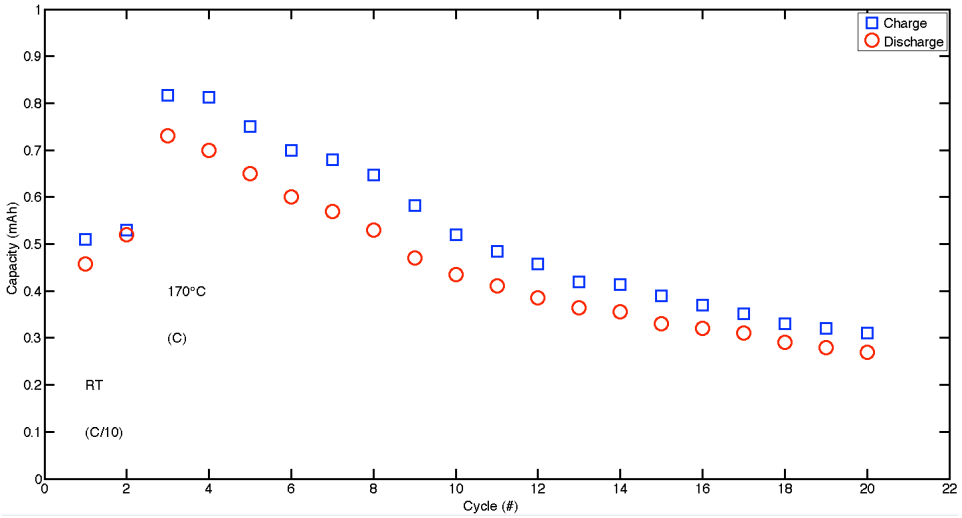

Figure 5.7 Isothermal cycling at 170 °C

Figure 5.8 shows the isothermal cycling of the cell at 200 °C at C. This is the first time that anyone has ever demonstrated the cycling of a solid polymer lithium battery above the melting temperature of lithium metal. We prove that it is possible to pass current between a solid polymer electrolyte and liquid lithium metal without a passivation film. However without a passivation film, the lithium metal is rapidly consumed, and results in rapid capacity fade.

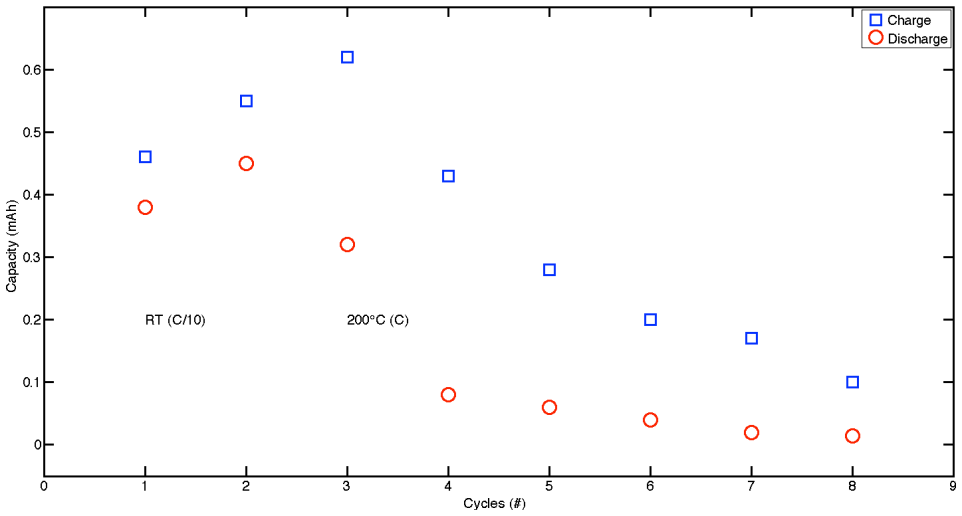

Figure 5.8 Isothermal cycling at 200 °C

5.3.2 Cycling from Room Temperature to High Temperatures

Figure 5.9 shows the cycling of the cell from room temperature up to 200 °C. This is also the first time that anyone has demonstrated the wide-temperature capability of the solid polymer lithium battery. This spans the entire downhole drilling temperature range, about 85% of which lies between 50 °C to 150 °C. After the cell was heated to a desired temperature, it was held at open-circuit for 2 hours before performing cycling tests.

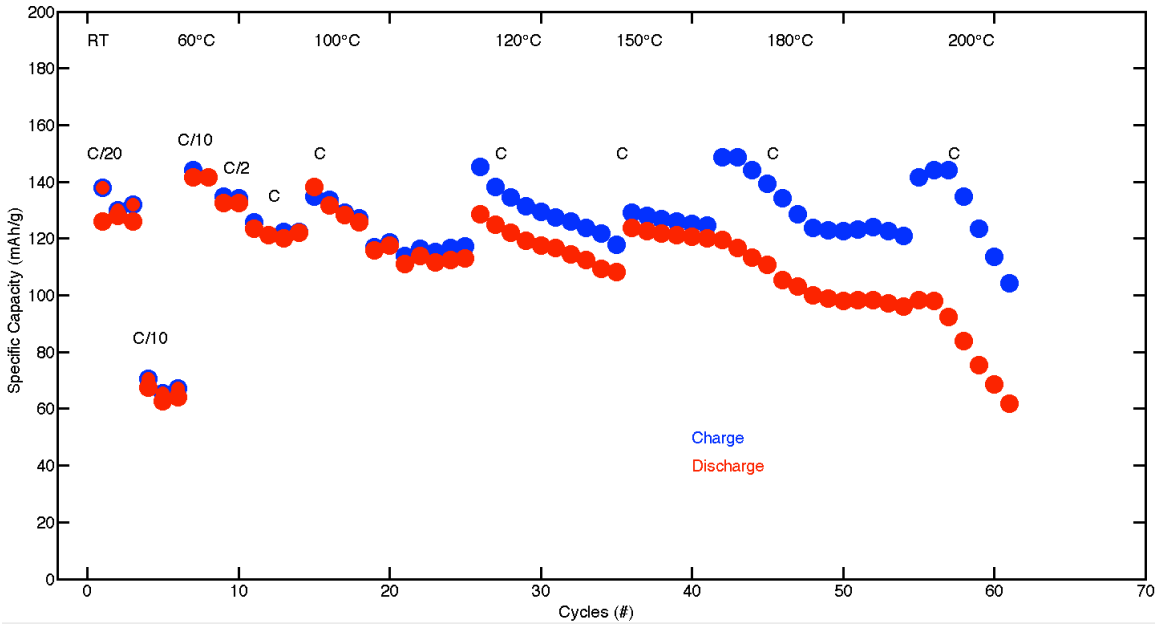

Figure 5.9 Cycling from room temperature to 200 °C

Figure 5.9 also illustrates that the rate capability of the battery improves as the temperature increases. At room temperature, very low current (C/20) was required to achieve the practical specific capacity; and the capacity dropped significantly if the current was doubled to C/10. At 60 °C, higher currents (C/10, C/2, and C) were used, and much higher specific capacities were achieved. And from

100 °C to 200 °C, a c-rate of C was used throughout, and almost the entire practical specific capacity is consistently achieved.

We observe in Figure 5.9 that the capacity fade increases as temperature increases. This is due to the increasing reactivity of lithium metal and the instability of the passivation film at elevated temperatures. Also there is a large increase in the charge capacity every time the cell is raised to a new temperature, indicating that excess current is needed to reform the passivation film, which is under mechanical stress due to the thermal expansion of the lithium metal.

5.3.3 Thermal Cycling

In addition to isothermal cycling, thermal cycling tests are also performed. This has interesting implications for oil drilling, where the battery is discharged downhole under high temperatures, and charged on the surface under room temperature.

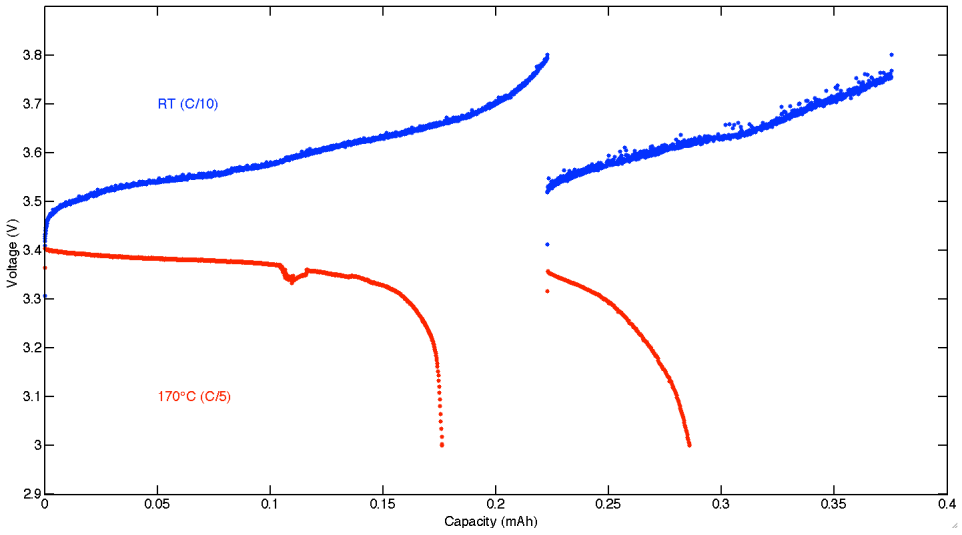

Figure 5.10 Thermal cycling between room temperature and 170 °C

Figure 5.10 shows the voltage profiles of thermal cycling between room temperature and 170 °C. The cell was charged at room temperature using a low current of C/10, heated to 170 °C and discharged using a higher current of C/5, and cooled back to room temperature and the cycling is repeated once.

Figure 5.11 shows the voltage profiles of thermal cycling between room temperature and various high temperatures from 60 °C up to 200 °C, where the cell was charged at room temperature at C/10 and discharged at high temperatures at C/5. The high temperature discharge voltage profiles have lower overpotentials compared to lower c-rate room temperature charge voltage profiles, indicating faster polymer electrolyte conductivity at high temperatures.

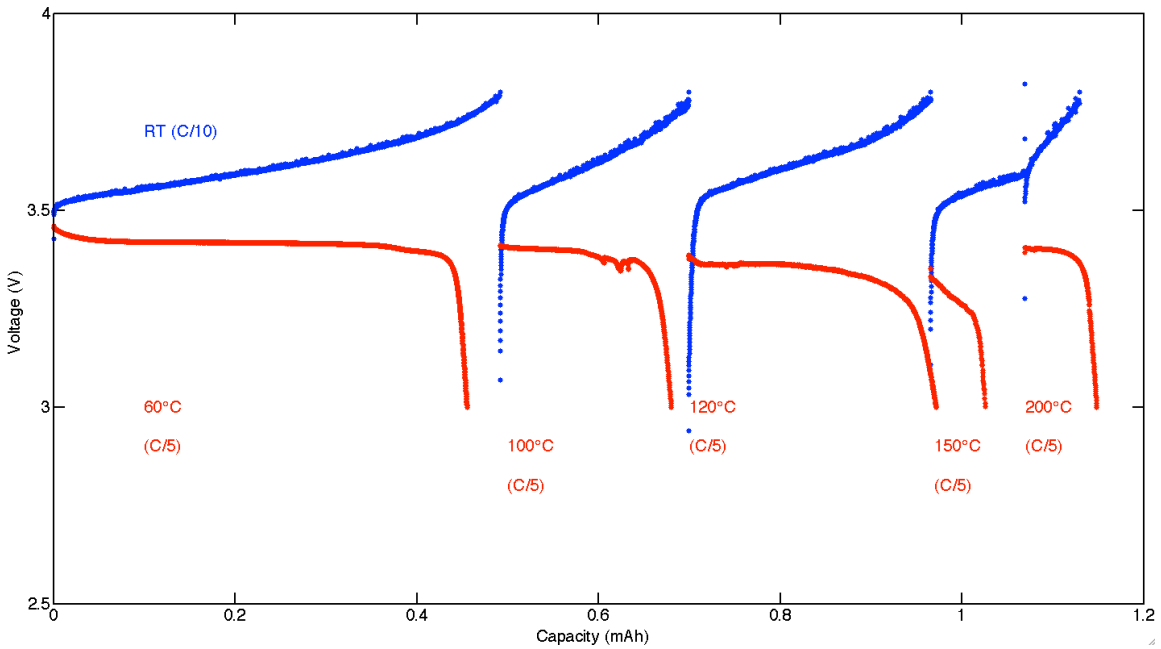

Figure 5.11 Thermal cycling between room and elevated temperatures

While we demonstrated the thermal cycling of the polymer electrolyte, we notice that the charge capacity fades with thermal cycling, suggesting that heating has an adverse effect on the polymer segmental motion and conductivity.

5.3.4 Comparison of Cell Performance at Different Temperatures

Figure 5.12 shows the discharge voltage profiles of the solid polymer cells at room temperature, 60 °C, and 120 °C using a low current of C/20. At both 60 °C and 120 °C, the cell exhibits low overpotential due to fast polymer electrolyte conductivity, and nearly the full theoretical specific capacity can be accessed.

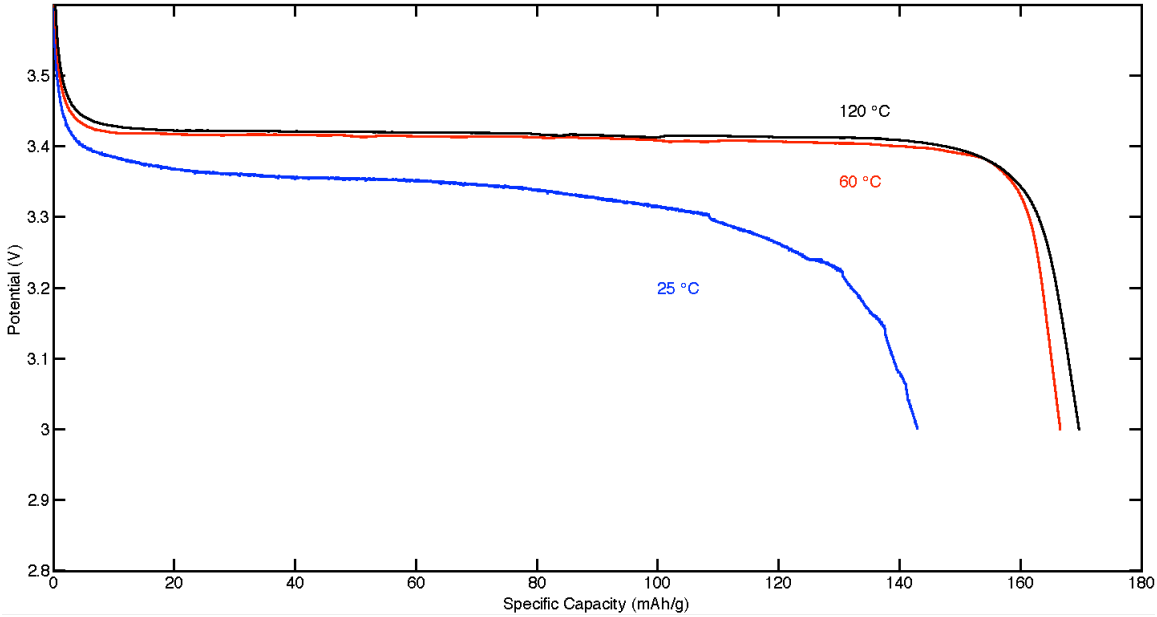

Figure 5.12 Discharge voltage profiles at different temperatures

Full rate capability test of the solid polymer cells were also performed at these three temperatures. At each temperature, the cells were charged at a constant current of C/20 (or 25 W/kg considering the cathode loading mass density) and discharged at higher currents. A fresh cell was used for each discharge current to isolate the effect of capacity fade. The discharge voltage profiles as functions of specific capacity are shown in Figure 5.13, where the discharge current is in μA and labeled next to the discharge curve. Figure 5.13 shows poor rate capability at room temperature, and much better rate capability at elevated temperatures.

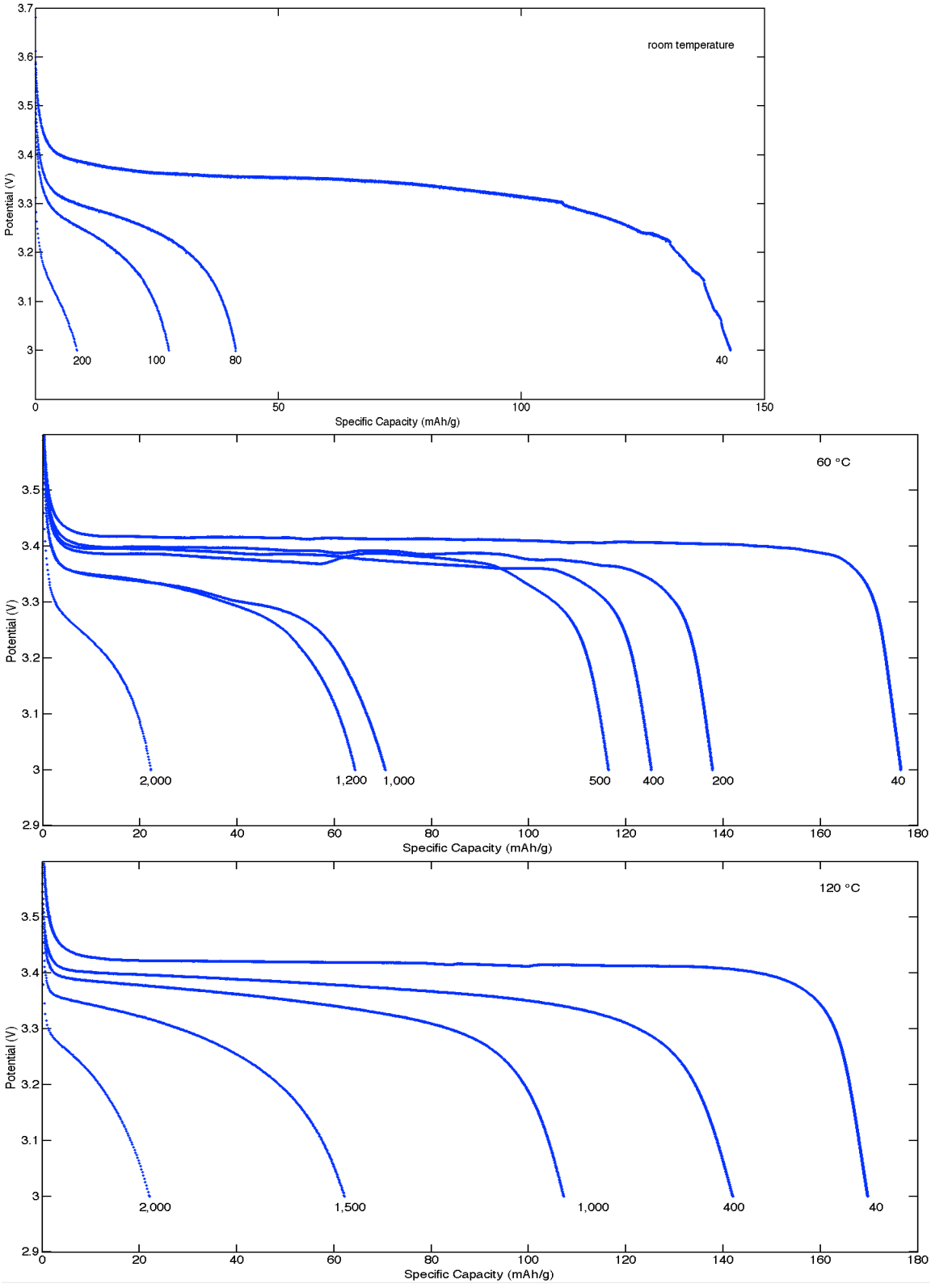

Figure 5.13 Discharge rate capability at different temperatures

The rate capability test of a cell with commercial liquid electrolyte (LP30) was also performed at room temperature. The energy densities (integrating the discharge voltage with respect to specific capacity) at different power densities (multiplying the constant current with discharge voltage) are shown in the Ragone plot in Figure 5.14 for the different temperatures.

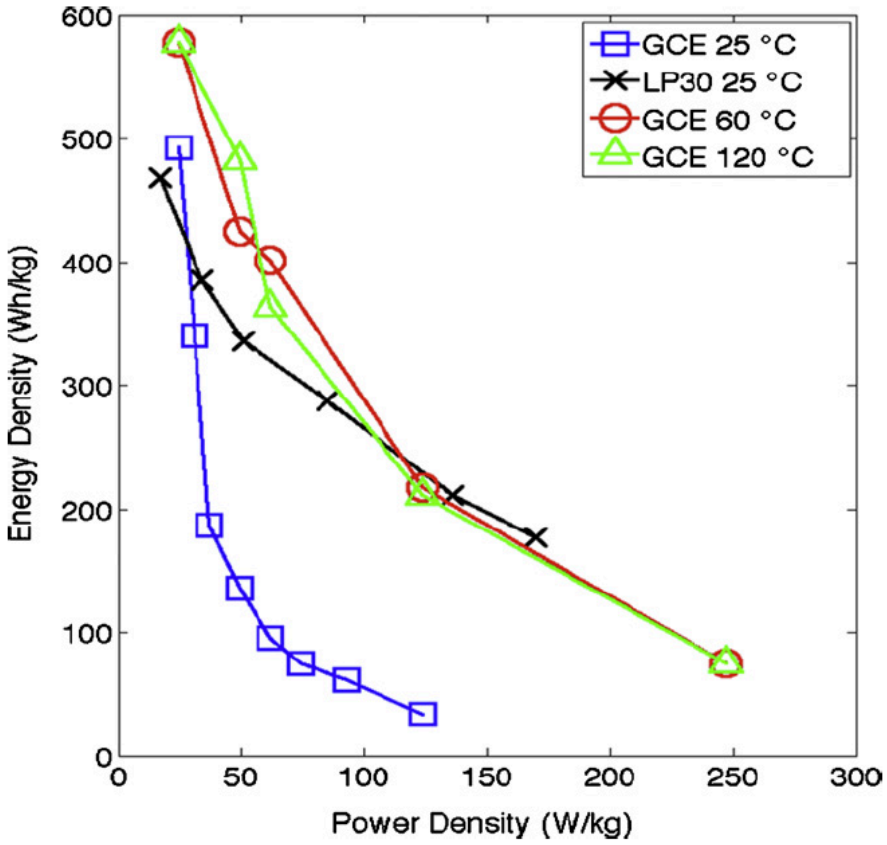

Figure 5.14 Ragone plot for polymer and liquid electrolyte batteries at different temperatures [103]

Figure 5.14 reflects the tradeoff between energy density and power density. At large currents, the cell performance becomes diffusion-limited and the cell capacity decreases. For the LP30-based cells, only room-temperature data were collected. In the case of the GCE-based cells, performance near 60 °C is of particular

interest since this temperature is in the range of the melting point of PEO. As indicated in Figure 5.14, at room temperature the energy densities of the GCE and LP30-based cells are comparable at low power densities. As the power density is increased from 25 to 50 W/kg, the energy density of the GCE-based cells falls drastically. However, at elevated temperatures (> 60 °C), the decrease in energy density of the GCE-based cells with increasing power density is significantly smaller due to the higher mobility of PEO chains. Above 60 °C, the performance of the GCE-based cell becomes less dependent on temperature and comparable to the room-temperature performance of the liquid electrolyte-based cells.

5.3.5 Effect of High Temperature on Polymer Electrolyte

In previous sections, we demonstrated the performance of the polymer cells at high temperatures; in this section we investigate the effect of heating on the polymer electrolyte itself using DSC, TGA and FTIR techniques.

Fourier transform infrared spectroscopy (FTIR) was performed with a Thermo Nicolet NEXUS 670 spectrometer equipped with a diamond attenuated total reflection (ATR) accessory. ATR-IR spectra were obtained at 1 cm^{-1} resolution and summed over 100 scans. Isothermal thermogravimetric analysis (TGA) was done under flowing nitrogen using a TA Instruments Q50. Differential scanning calorimetry (DSC) was performed using a Q1000 DSC (TA Instruments). The heating/cooling rate was 10 °C/min, and the nitrogen purge rate was 50 mL/min.

Isothermal TGA study of the graft copolymer at 140 °C under inert atmosphere reveals a weight loss of less than 2% over 50 hours (Figure 5.15).

However, the graft copolymer shows discoloration after long exposure to elevated temperatures (Figure 5.16 inset). FTIR analysis of the graft copolymer before and after heating reveals cleavage of different bonds within the polymer structure.

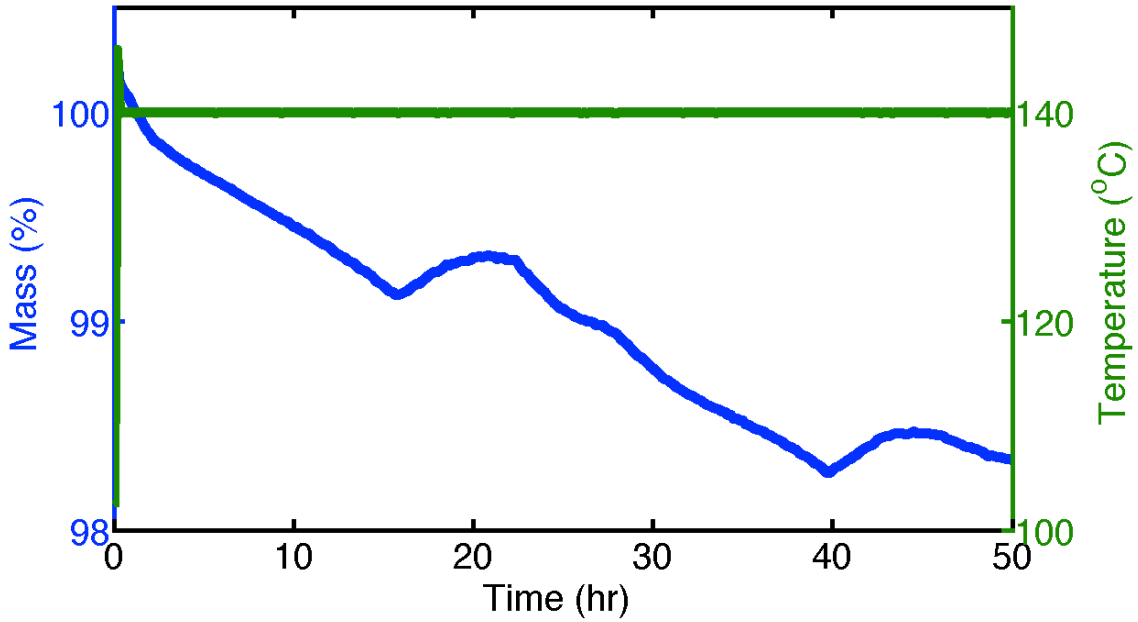

Figure 5.15 Isothermal TGA of graft copolymer at 140 °C

The most significant changes upon heating are the decreases in the symmetric and asymmetric stretching modes of C–H in the methyl CH_3 (peaks between 2800 and 3000 cm^{-1}) and the stretching mode of the carbonyl (C=O) groups (~ 1730 cm^{-1}), both of which are associated with the methacrylate backbone. Decays are also observed in O–Si–O (from the PDMS sidechain), C–O–C, and C–H in CH_2 (from the POEM sidechain). Si–CH_3 remains stable during heating [35, 57, 126].

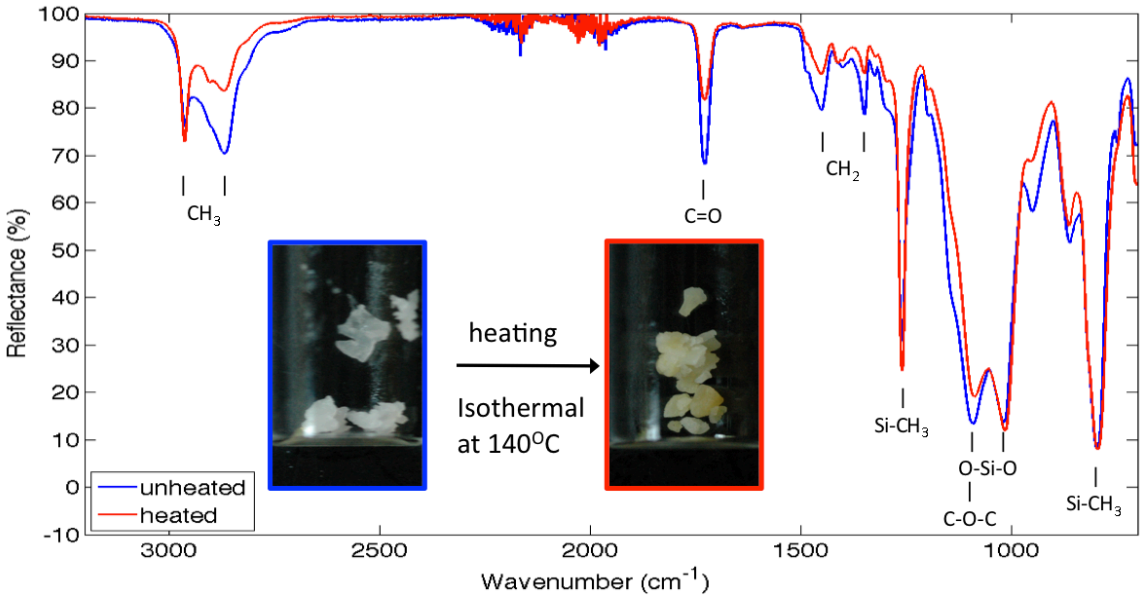

Figure 5.16 FTIR spectra of unheated and heated (140 °C) graft copolymer. The graft copolymer shows discoloration after heating (inset) [103]

Despite the potential bond cleavages in the PDMS domain and the backbone after prolonged heating, both the undoped graft copolymer (GC) and the doped graft copolymer electrolyte (GCE) are stable and do not undergo additional phase transformations or decomposition reactions above 60 °C, as evident in the DSC heating curves shown in Figure 5.17 (the features are the same as those of Figure 3.16 in Chapter 3).

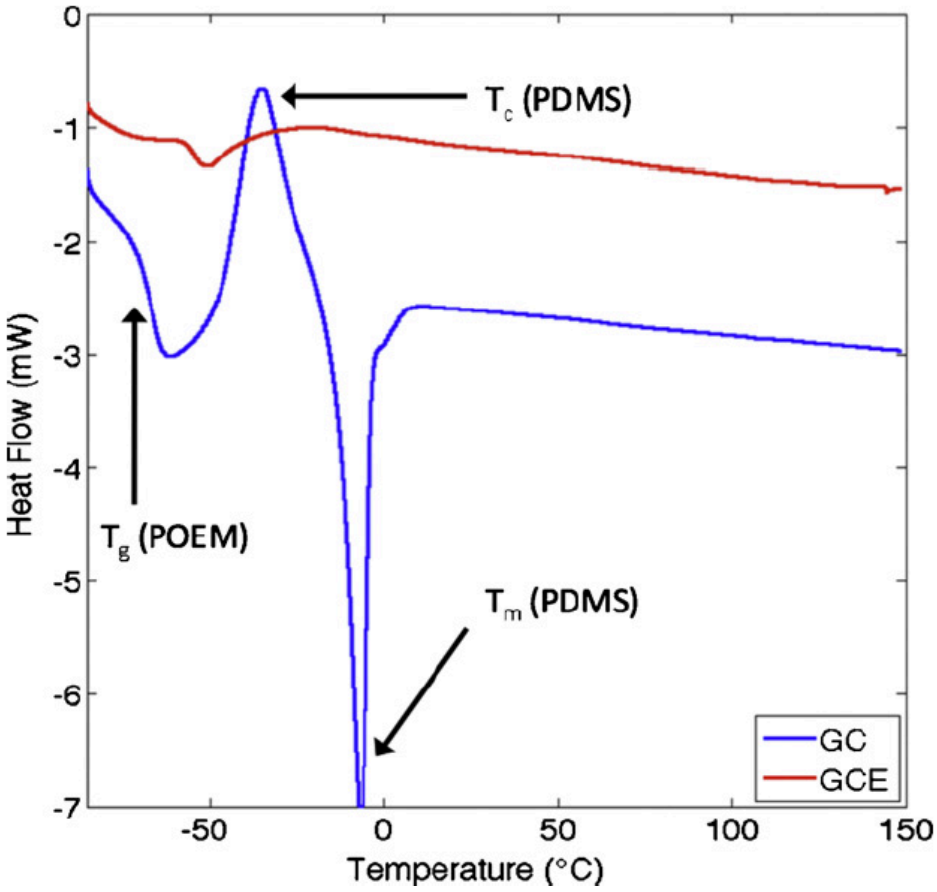

Figure 5.17 DSC spectra of undoped graft copolymer and doped graft copolymer electrolyte

5.3.6 Full Cell EIS Study at Different Temperatures

EIS was used to study changes in the resistance of the various cell components and to evaluate their dependence on cycling and temperature. Figure 5.18a shows the Nyquist plot of a fully discharged $LiFePO_4$/GCE/Li cell and the corresponding equivalent circuit model (ECM) used for EIS analysis (inset in Figure 5.18a). At the highest frequency, a non-zero x-axis intercept indicates the presence of solution resistance, or resistance through the bulk GCE (R_{BULK}), and is represented by a resistor in the ECM. In the high frequency region, a CPE behavior, or several

overlapping semicircles associated with lithium-ion transport through a multilayered passivation film (solid electrolyte interphase) is observed (R_{SEI}). The multilayer characteristics of the passivation film are represented by multiple R||C parallel circuits in series, akin to the Voight model. At medium and low frequencies, the impedance contributions result primarily from the charge-transfer resistance (R_{CT}) and double-layer capacitance (C_{DL}) at the electrode-electrolyte interface, as well as solid-state diffusion through the active electrode materials (Warburg element) [73, 127-129].

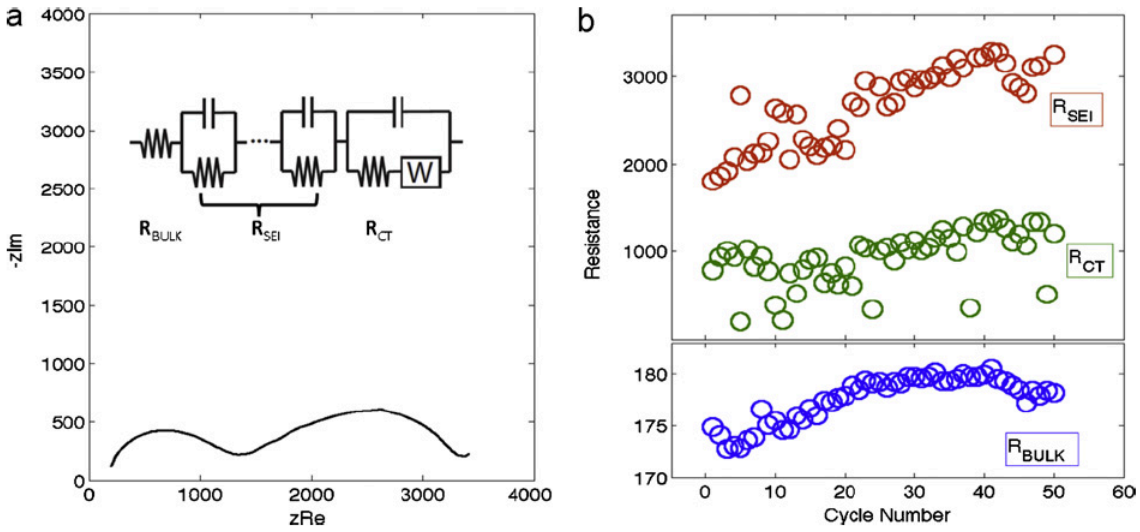

Figure 5.18 Typical EIS spectrum for $LiFePO_4$/GCE/Li (a) and equivalent circuit model (a inset). Evolution of various impedance components during room temperature cycling (b) [103]

In order to analyze changes in the impedance of $LiFePO_4$/GCE/Li cells upon cycling, EIS was performed after each cycle (fully discharged state) for 50 cycles at room temperature, and the parameters extracted from the fitting program were plotted in Figure 5.18b. We observe that R_{BULK} increases in the early cycles but

quickly stabilizes, suggesting no or little changes in the GCE during long cycling. Similarly, R_{CT} remains relatively constant upon cycling, revealing a high mechanical stability of the electrode materials. In the case of R_{SEI}, 5 R||C elements are used to fit the interfacial passivation film and the sum of their resistances is plotted. A total of 14 circuit elements are used in the fitting. We observe a steady increase in R_{SEI}, indicating an unimpeded growth of the passivation film. As illustrated in Figure 18b, the overall cell resistance is dominated by R_{SEI} and R_{CT}, suggesting that the performance-limiting factor is not the electrolyte but the electrode-electrolyte interface. Future work on lithium polymer batteries should therefore focus not only on optimizing the conductivity of the polymer electrolyte, but also on modifying the electrode-electrolyte interface to decrease the interfacial impedance.

In Figure 5.19, EIS was performed on discharge $LiFePO_4$/GCE/Li cells after room temperature conditioning at various elevated temperatures. Since R_{BULK} (Figure 5.19a) is simply the resistance of the pure GCE, its temperature dependence agrees with the VTF behavior typical for polymer conduction in the amorphous phase. However, the interfacial impedance R_{SEI} goes through a minimum, decreasing up to 80 °C and then increasing above 100 °C (Figure 5.19b). This is consistent with changes in the reaction selectivity in the passivation film, causing the film to be more resistance to lithium transport, and leading to discharge capacity fade observed in high temperature isothermal cycling (Figures 5.5 to 5.9) [39, 41, 50, 61, 83, 126, 130-137].

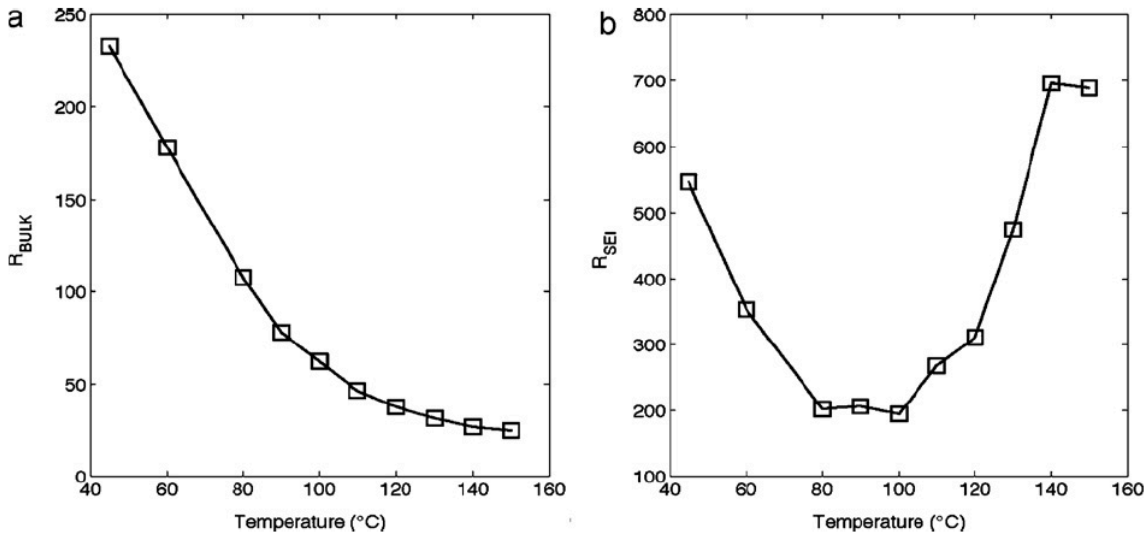

Figure 5.19 Impedance through bulk electrolyte (a) and across interfacial layers (b) as function of increasing temperature [103]

In this chapter, we show for the first time that lithium batteries can be safely operated over a wide temperature range, reaching temperatures up to 200 °C, and even above the melting temperature of lithium, all without the need for pressure housing or other protective measures. Since both the cathode and the graft copolymer electrolyte are shown to be stable up to 300 °C, it is most likely the anode that dictates the current performance limitations at high temperatures. Indeed, at elevated temperatures (> 120 °C) metallic lithium becomes extremely reactive, leading to the observed capacity fade. Switching to a more temperature-stable anode, such as graphite or a lithium alloy, may further increase the upper temperature limit of operation. However, a trade-off between energy density, cycle life, and temperature stability must be made since these alternative anode materials each exhibit lower capacities and/or experience significant volume changes that limit the cycle life.

The physical model of lithium polymer batteries is complicated by the presence of an interfacial passivation film on the anode, not to mention by diffusion and transport processes within the bulk electrolyte and electrodes. While EIS can be used to differentiate between the various components, future studies using in situ Raman spectroscopy, FTIR, and electron microscopy techniques will be required to identify the molecular species involved, and to validate the assumptions made from EIS data. Both room and elevated temperature EIS data presented in this chapter indicate that the dominate performance-limiting factor is not associated with the electrolyte or the electrodes, but with the electrolyte-electrode interface. Understanding these interfacial phenomena will be key to the development of safe, high energy density, polymer-based solid-state lithium batteries.

In the next chapter, symmetric cell EIS will be used to further examine the properties of the anode-electrolyte interface, and their dependence on temperature.

6. Anode-Electrolyte Interface

In the previous chapter, full cell EIS was used to study the properties of the electrode-electrolyte interface at elevated temperatures. However, with full cell EIS, it is difficult to distinguish if the contribution came from the cathode-electrolyte or anode-electrolyte interface. Since the thermal stability and cycling capacity fade of the cells are limited by the lithium metal and its passivation film, we are most interested in the anode-electrolyte interface. In this chapter, we use symmetric cell (Li/GCE/Li) EIS to study the anode-electrolyte interface as a function of cycling and at elevated temperature [39, 132].

6.1 Experimental

Symmetric cells with lithium metal discs as both the working and counter electrodes, and dry solid polymer electrolyte in between were prepared and sealed inside CR2032 coin cells for testing (Figure 6.1).

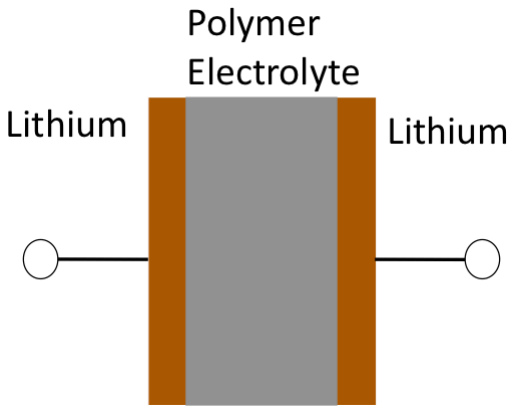

Figure 6.1 Li/GCE/LI symmetric cell

The symmetric cells were first "conditioned" by charging and discharging the cells for 5 cycles at room temperature to allow for the formation of passivation film on lithium metal and the improvement of interfacial contact such as the filling of voids between the two solid surfaces (note the passivation film is formed during both charge and discharge for the symmetric cells). Then square wave galvanostatic cycling and EIS tests at intervals were performed from room temperature up to 200 °C. The measurement sequence at each temperature was the following [36, 41, 74]:

1. Charge at 60 μA for 10 hours
2. EIS scan at OCV from 10 μHz to 1 MHz
3. Discharge at 60 μA for 10 hours
4. EIS scan at OCV from 10 μHz to 1 MHz
5. Loops back to step 1

This sequence was repeated and the Nyquist plot from each EIS scan was recorded and simulated to extract the important parameters.

A typical Nyquist plot for the Li/GCE/Li symmetric cell is shown in Figure 6.2. The highest frequency component (>10^5 Hz), the x-intercept is related to ion transport within the bulk electrolyte and this component decreases as temperature increases following a VTF behavior. The medium high frequency (10^2 to 10^5 Hz) semicircle is related to the formation of surface layers at the anode-electrolyte interface, involving lithium ion transport through the passivation film. The medium frequency (10^{-1} to 10^2 Hz) semicircle is associated with charge transfer. The low frequency (10^{-5} to 10^{-2} Hz) feature is associated with Warburg impedance, characteristic of the transport of charged particles in the lithium electrodes [72, 79].

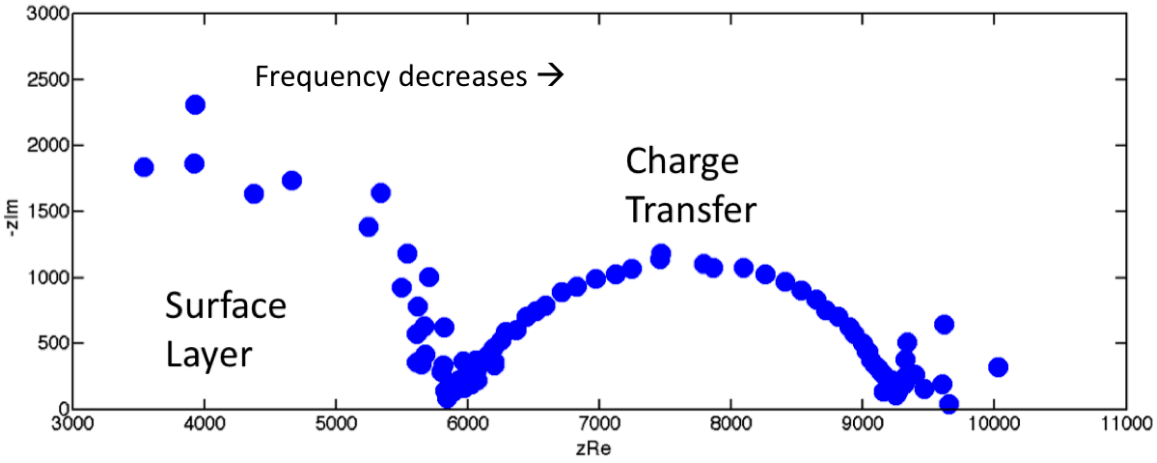

Figure 6.2 Sample Nyquist plot for the Li/GCE/Li symmetric cell

The corresponding equivalent circuit model used to fit the Nyquist plot in Figure 6.2 is shown in Figure 6.3, where R_{sf} is the surface layer resistance, and R_{ct} is the charge transfer resistance. These two values were extracted from the simulated results at different temperatures and after each charge and discharge.

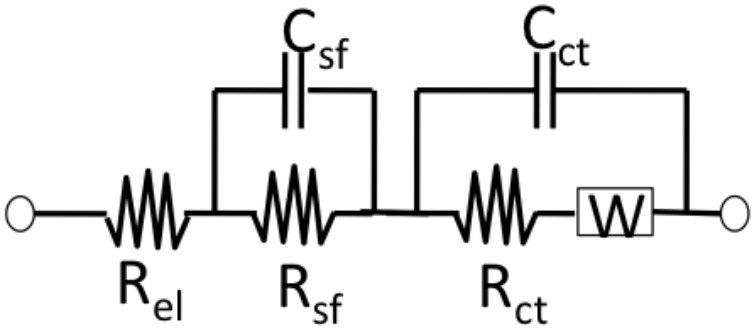

Figure 6.3 Equivalent circuit model used to fit the Nyquist plot

6.2 Results and Discussion

6.2.1 Room Temperature to 120 °C

The Nyquist plots from room temperature to 120 °C are listed in Figure 6.4, where although the scales are different due to the significantly different impedance

values at different temperatures, the features are consistent with those in Figure 6.2, two semicircles for the surface layer and charge transfer components.

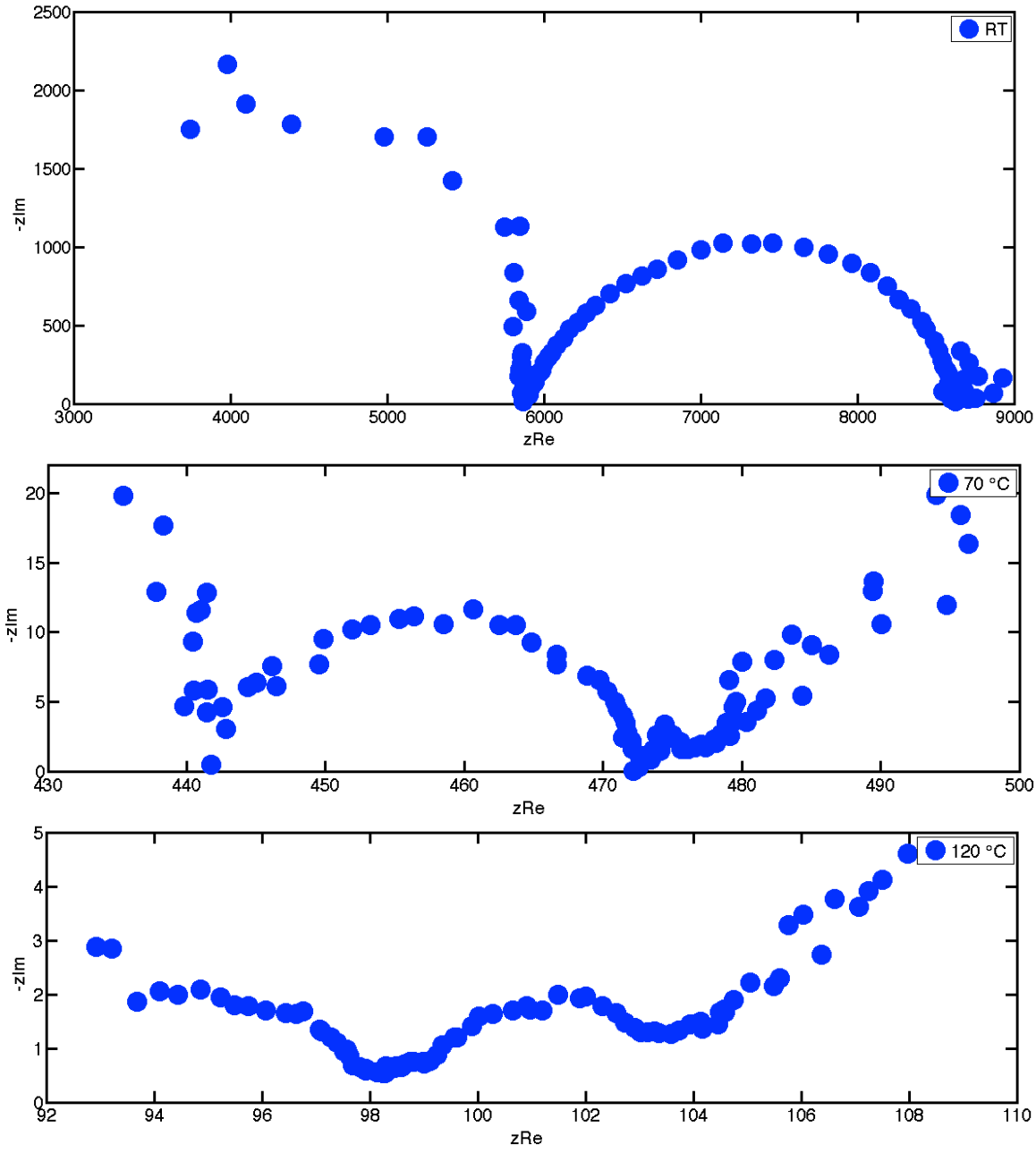

Figure 6.4 Nyquist plots from room temperature to 120 °C

Both R_{sf} and R_{ct} are plotted as functions of cycling for different temperatures (Figure 6.5 and 6.6), and are shown to be stable with cycling [138-144].

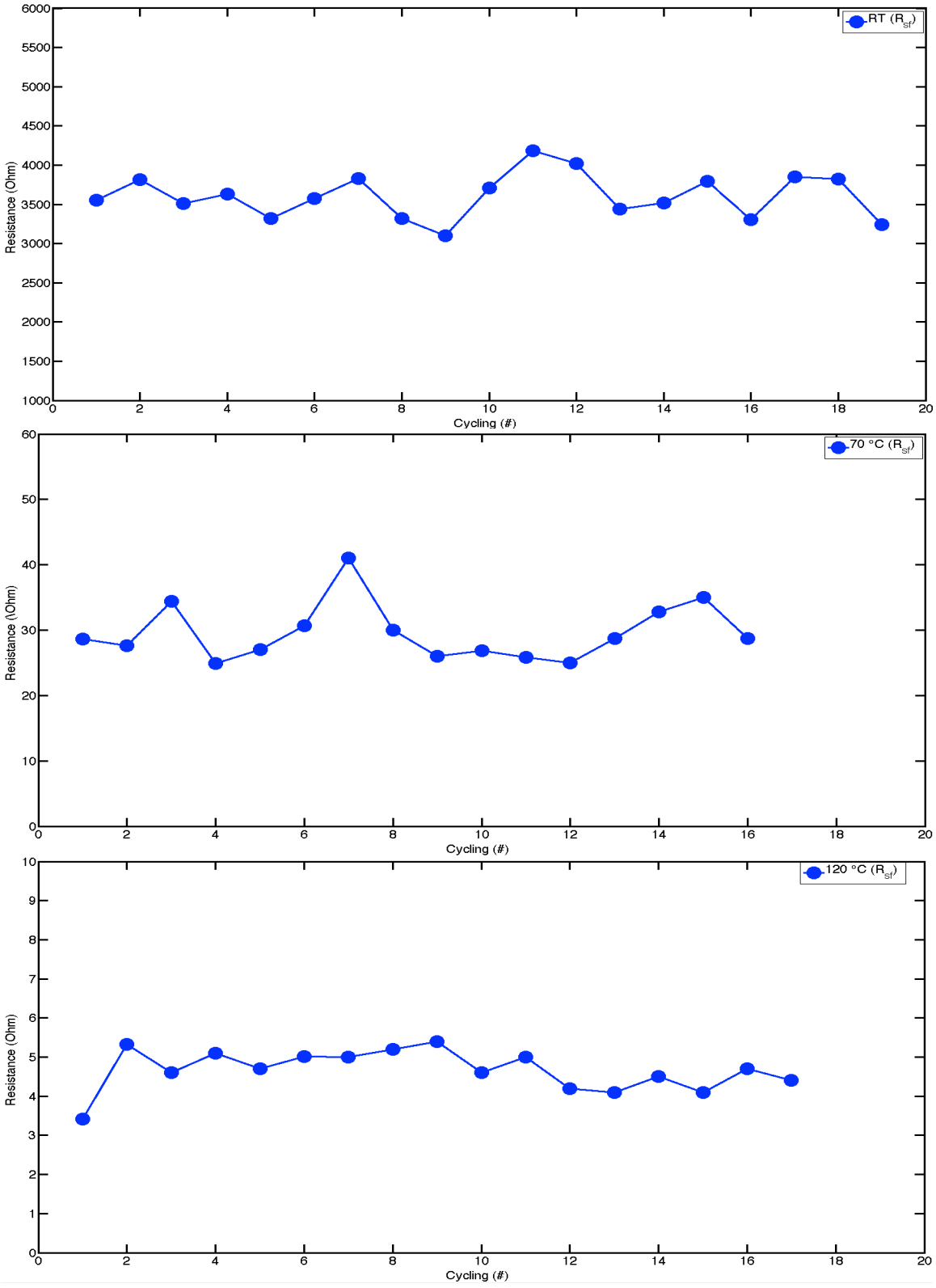

Figure 6.5 Surface layer resistance (R_{sf}) from room temperature to 120 °C

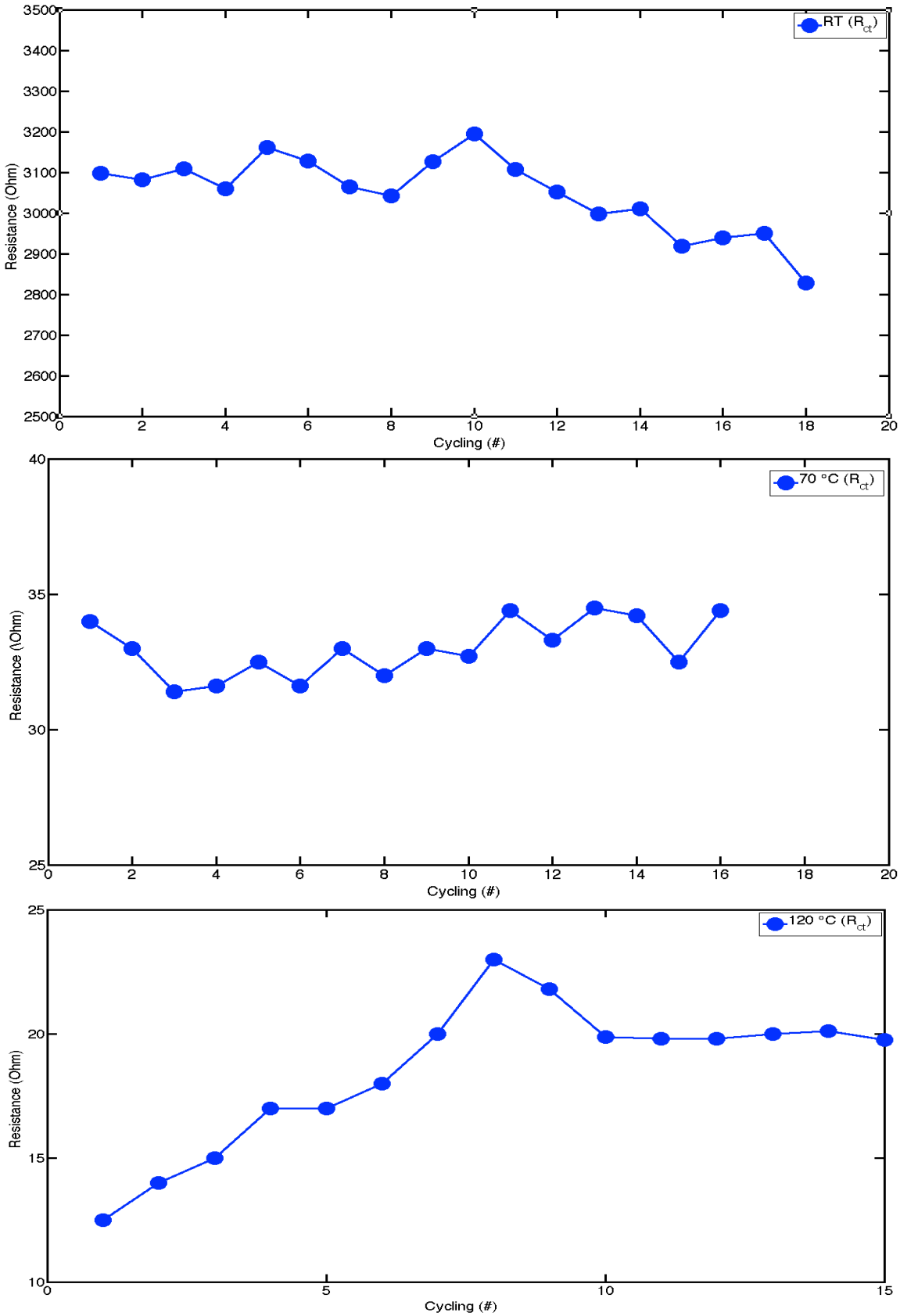

Figure 6.6 Charge transfer resistance (R_{ct}) from room temperature to 120 °C

In Figure 6.6, R_{ct} at 120 °C increases with cycling, indicating that long heating increases the charge transfer impedance, consistent with Figure 5.19b in Chapter 5. Both R_{sl} and R_{ct} are plotted as functions of increasing temperature in Figure 6.7, showing VTF behavior characteristic of ion transport through a polymeric film.

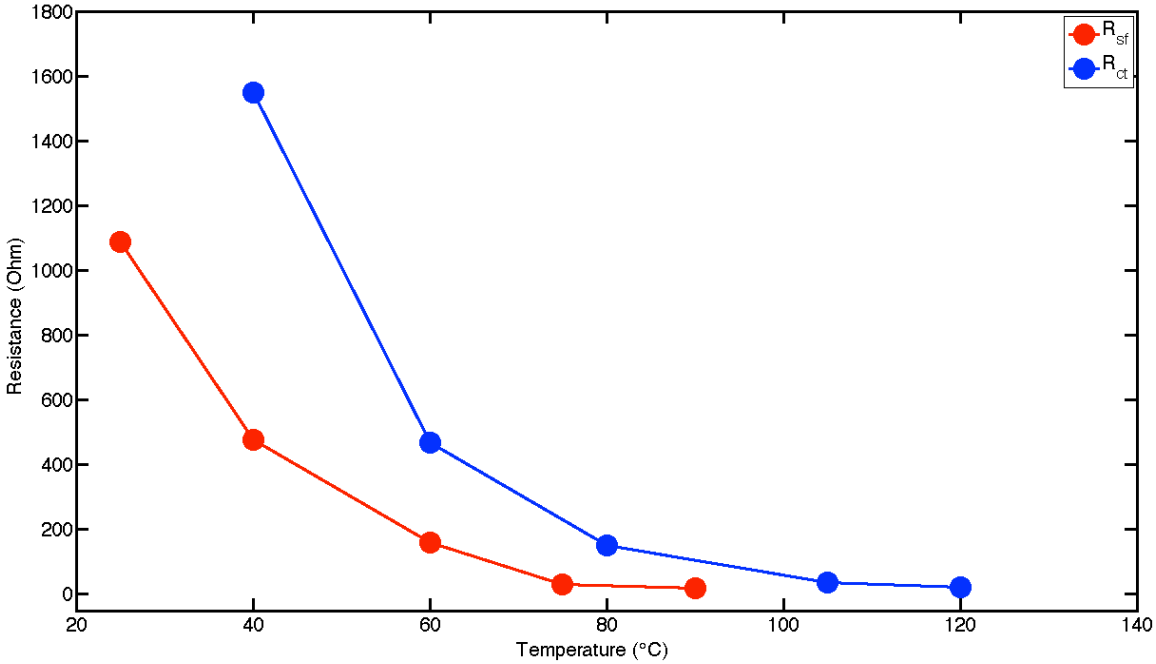

Figure 6.7 Surface layer (R_{sl}) and charge transfer (R_{ct}) resistances as functions of temperature

6.2.2 Extremely High Temperatures (140 °C to 200 °C)

At higher temperatures from 140 °C to 200 °C, all impedance components continue to decrease as expected, but the Nyquist plots have significantly different features (shown in Figure 6.8). The surface layer semicircle at high frequency disappears (at the lower end of 140 °C, we can still observe a weak semicircle associated with the surface layer, but it is unstable and not consistently reproducible for different cells; and at higher temperatures, this semicircle

completely disappears), and only the charge transfer semicircle and Warburg diffusion features remain [145].

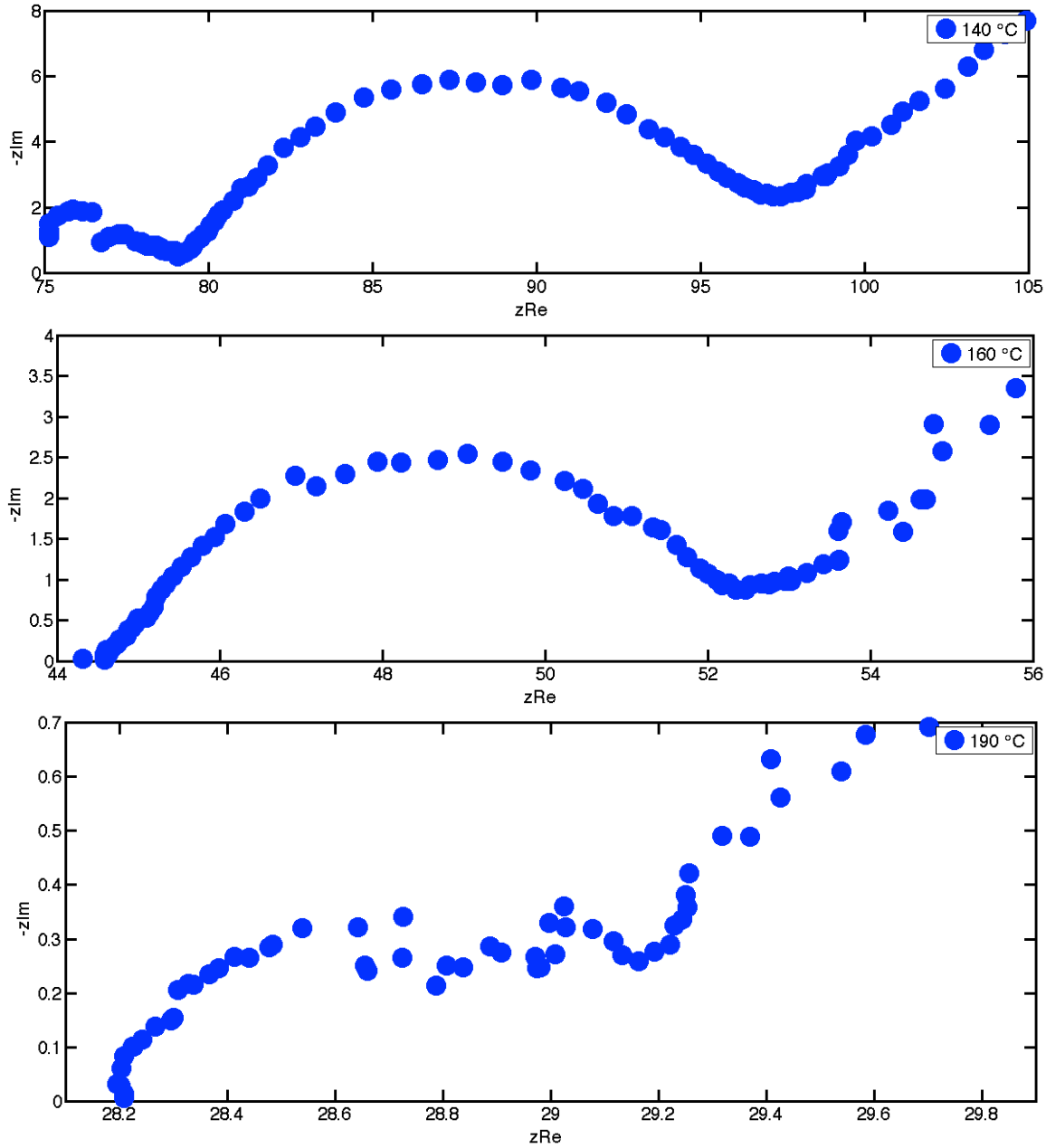

Figure 6.8 Nyquist plots from 140 °C to 200 °C

The corresponding equivalent circuit model for the new Nyquist plots is shown in Figure 6.9. The R||C parallel circuit associated with high frequency surface layer is eliminated (compared to the model for lower temperatures in Figure 6.3). The physical implication is that at such high temperatures, due to the reactivity of lithium metal, it is no longer possible to form a stable passivation film, and hence the absence of the R_{sl} contribution. However, at high frequencies the polymer electrolyte continues to conduct ions and its resistance R_{el} follows a VTF behavior; and the charge transfer at the interface and Warburg diffusion through lithium metal electrodes both remain relevant at low frequencies [36, 37, 72, 73, 146-150].

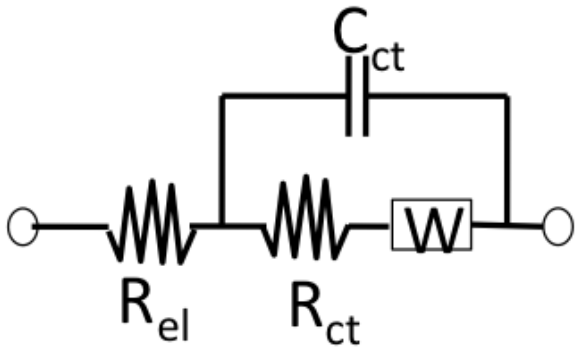

Figure 6.9 Equivalent circuit model for Nyquist plots from 140 °C to 200 °C

The charge transfer resistance across the interface R_{ct} is plotted as a function of cycling for each of the temperatures (shown in Figure 6.10). Interestingly and unlike the R_{ct} at lower temperatures (shown in Figure 6.6), the R_{ct} is seen to steadily increase upon cycling at these extremely high temperatures.

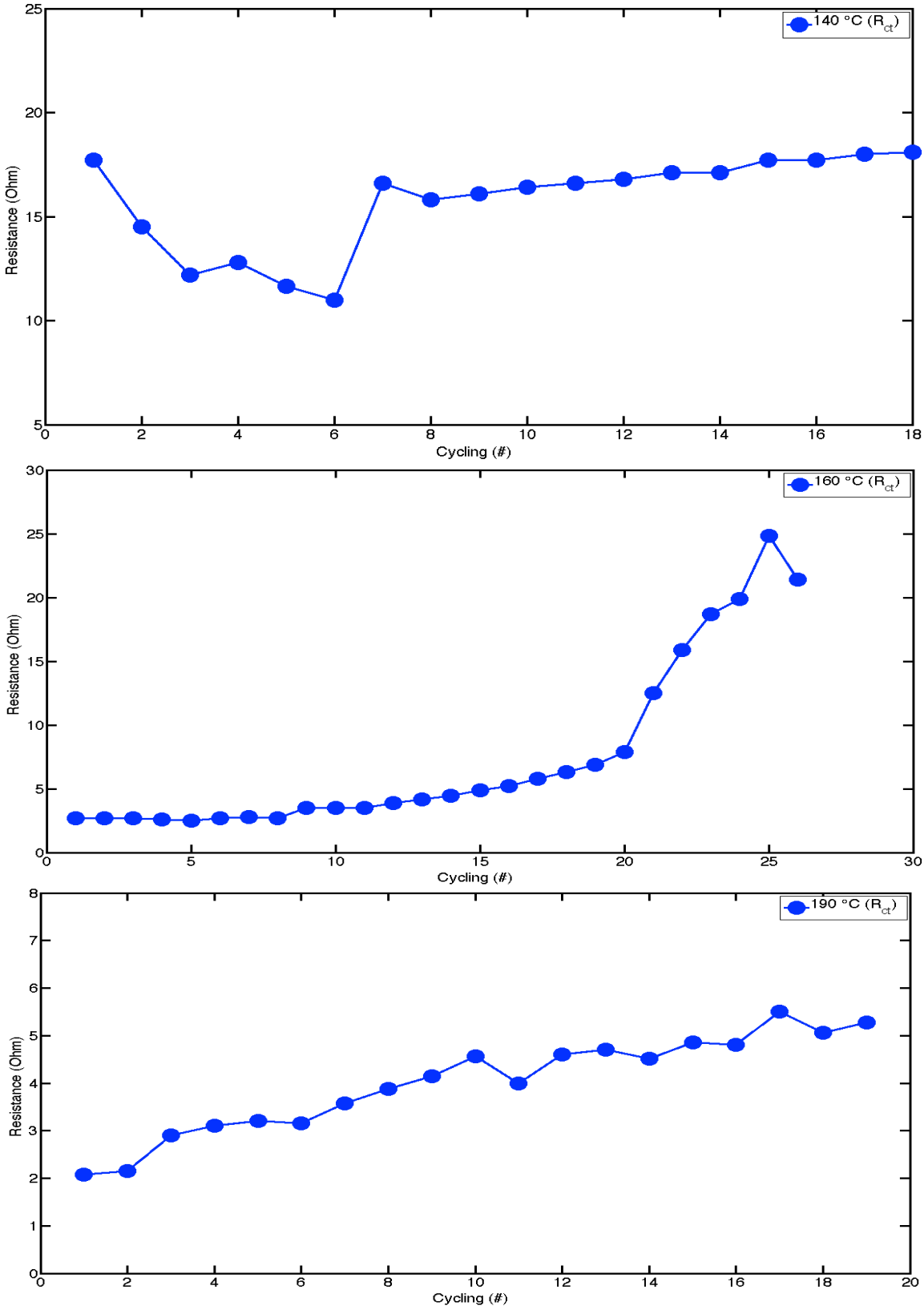

Figure 6.10 Charge transfer resistance (R_{ct}) from 140 °C to 200 °C

6.3 Summary

In Chapter 5, while we demonstrated the ability for the solid polymer lithium battery to cycle up to 200 °C, beyond the melting temperature of lithium metal, we noticed increasing capacity fade at higher temperatures. We hypothesized that it is related to the thermal instability of the passivation film on lithium at such high temperatures. In this chapter, we used EIS and equivalent circuit modeling and confirmed that indeed the passivation film disappeared above 140 °C.

The presence of the passivation film allows the passage of lithium ions but protects the lithium metal by preventing its continuous consumption. When the passivation film is unstable or completely absent (when lithium metal is highly reactive at high temperatures or is molten above its melting point); while charge transfer still occurs at the interface, lithium metal is rapidly consumed and results in rapid capacity fade [38, 39, 41, 135, 151-155]. Figure 6.11 shows a post-cycle lithium disc at 120 °C, and a completely consumed post-cycle lithium disc at 200 °C.

Figure 6.11 Lithium metal after cycling at 120 °C and 200 °C

A stable passivation film is pivotal in determining a battery's cycle life. We found from Chapters 5 and 6 that as temperature increases, the passivation film becomes less stable, and the overall battery cycle life decreases.

7. Dare to Dream: Polymer-Ionic Liquid (PIL) Batteries

The solid polymer lithium battery is not a new concept. The first PEO-based polymer electrolyte was developed in the late 1970s, and several companies tried to commercialize this technology in the early 2000s. The two most meaningful value propositions are enhanced safety and higher energy density (because of the use of lithium metal as the anode). However, its poor room temperature performance (rate capability) has prevented its wide adoption, and limited its use to high temperature applications only (because the rate capability improves dramatically at higher temperatures). Going forward, the room temperature performance of solid polymer lithium batteries must be improved to a level that is at least comparable to that of carbonate liquid electrolyte lithium-ion batteries, while not compromising on safety. The key enabler will come from a class of materials called ionic liquids.

7.1 The Cheetah, the Donkey, and the Horse

The majority of today's rechargeable lithium batteries are lithium-ion. While they have good performance, their carbonate liquid electrolyte is explosive, flammable, and prevents the use of lithium metal as the anode for fear of dendrite formation and thermal runaway. Safety concerns associated with the electrolyte limit the overall energy density and operating temperature (< 60 °C). In certain applications such as electric vehicles, complex engineering solutions including expensive and bulky cooling systems are used to improve the safety at the expense of overall battery pack energy density and cost.

Solid polymer lithium batteries have more than twice the energy density (because the ability of the solid polymer electrolyte to prevent dendrite formation allows the use of lithium metal as the anode), and are inherently much safer. Their high temperature stability eliminates the need for cooling systems. However, because they must be heated to high temperatures (> 60 °C) to achieve practical performance requirements, they need heating systems.

By combining solid polymer with a low melting temperature ionic liquid, we can greatly enhance the room temperature performance, and still maintain the safety and energy density advantages of solid polymer lithium batteries.

	Today's Standard Li-ion (carbonate liquid)	**My PhD Work** Solid Polymer	**The Future** Solid Polymer + Ionic Liquid
Energy Density (Wh/kg)	120	350	350
Safety	Explosive	Safe	Safe
Temperature Range	−20 °C to 60 °C	60 °C to 200 °C	−20 °C to 220 °C
Cooling/heating	Cooling	Heating	Neither
Performance	Good	Poor	Good

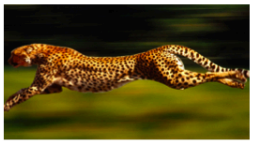

Figure 7.1 The cheetah, the donkey, and the horse

If today's lithium-ion batteries can be compared to a cheetah, fast but dangerous, and the solid polymer lithium batteries can be compared to a donkey, safe but slow, then this new polymer ionic liquid (PIL) lithium battery is like a horse, safe and fast. For thousands of years, the horse was safe enough to be used as a transportation tool, and fast enough to be ridden to battlefields (Figure 7.1).

7.2 Composite Electrolyte (Polymer + Ionic Liquid)

Certain room temperature ionic liquids (RTIL) have high room temperature conductivities, nearly 1,000 times higher than that of solid polymer, and can be comparable to or even higher than that of carbonate liquids (some of the most conductive RTILs such as ethyl-methylimidazolium dicyanamide have room temperature conductivities around 27 mS/cm), and the conductivity for ethyl-methylimidazolium bis(trifluoromethanesulfonyl)imide (EMIm/TFSI) is shown in Figure 7.2. They have also been shown to have wide electrochemical window of more than 5 V, and high flash point above 250 °C [43, 48, 50, 156-161].

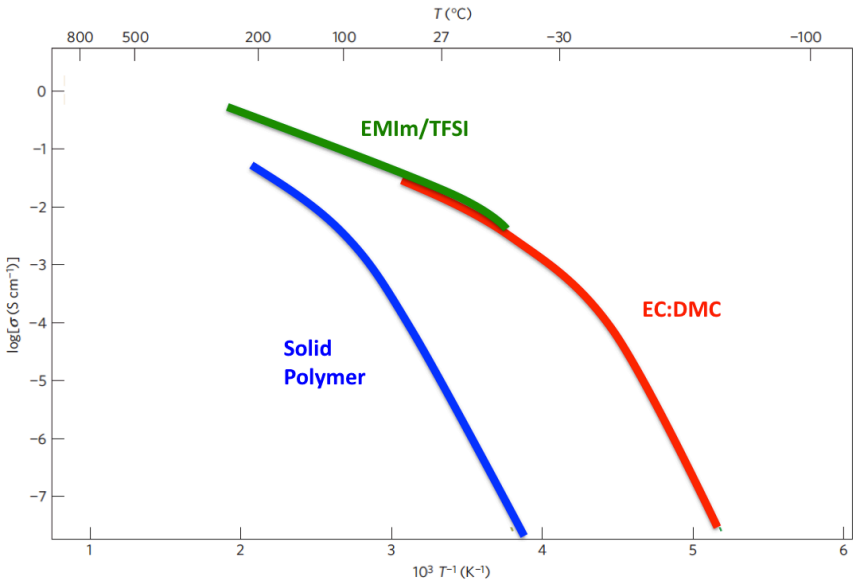

Figure 7.2 Conductivities of solid polymer, ionic liquid, and carbonate liquid

It has also been shown that by mixing low molecular weight polymers such as poly(ethylene glycol) dimethyl ether (PEGDME) with lithium salt and ionic liquid, the conductivity can be improved by reducing the viscosity and increasing lithium ion solvation. In the future, we can use this composite electrolyte to replace the solid

polymer electrolyte and maintain the safety and wide temperature performance characteristics [43, 49, 50, 161, 162].

7.3 Solid Polymer Passivation Film on Lithium Metal Anode

While the polymer ionic liquid (PIL) composite electrolyte improves the performance and safety of the battery, it cannot prevent dendrite formation on lithium metal. To maximize the energy density of the battery, the anode must use lithium metal, and the solid graft copolymer electrolyte (GCE) can be used as a passivation film on lithium. In the future, rather using the GCE as the full electrolyte, we can deposit a thin layer of GCE on lithium to suppress dendrites.

7.4 Cathode-Electrolyte Wetting

The PEGDME and ionic liquid mixture electrolyte is more viscous than carbonate liquid, and difficult to fully wet or penetrate the cathode matrix. Hence the GCE still needs to be used as the cathode binder, and we also need better soaking techniques such as diluting the PEGDME and ionic liquid mixture with an organic solvent such as THF or DMC to improve the wetting and then evaporate the organic solvent. Another approach is to chemically bond the GCE binder with the ionic liquid mixture.

7.5 Printable and Flexible Battery

The ionic liquid and PEGDME mixture electrolyte can be combined with the solid GCE to form a gel, enabling the entire battery to be roll-to-roll printed.

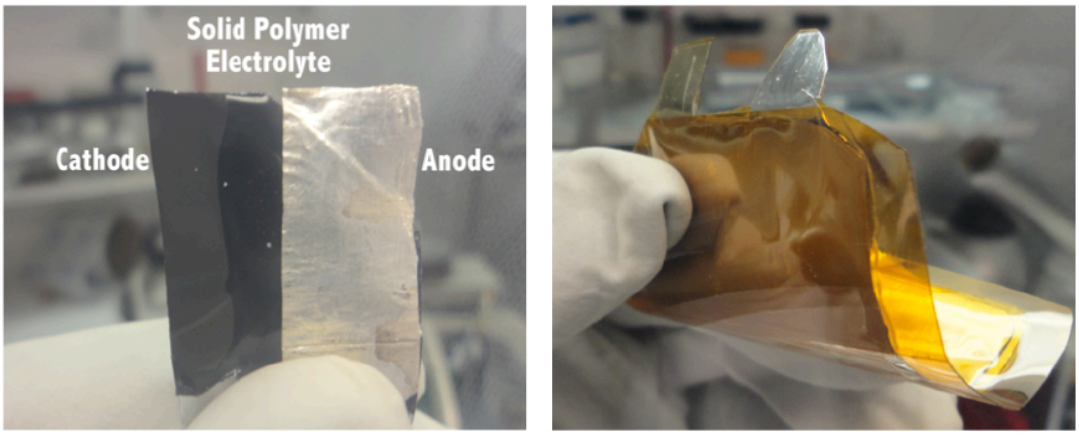

Figure 7.3 Printable and flexible battery

The printed three-layer battery is suitable for prismatic form factor, which has 30% higher packing density than cylindrical form factor (shown in Figure 7.3).

7.6 The Dream Battery

Finally if we combine the suggestions in sections 7.2 to 7.5, we have a recipe for the dream battery (shown in Figure 7.4).

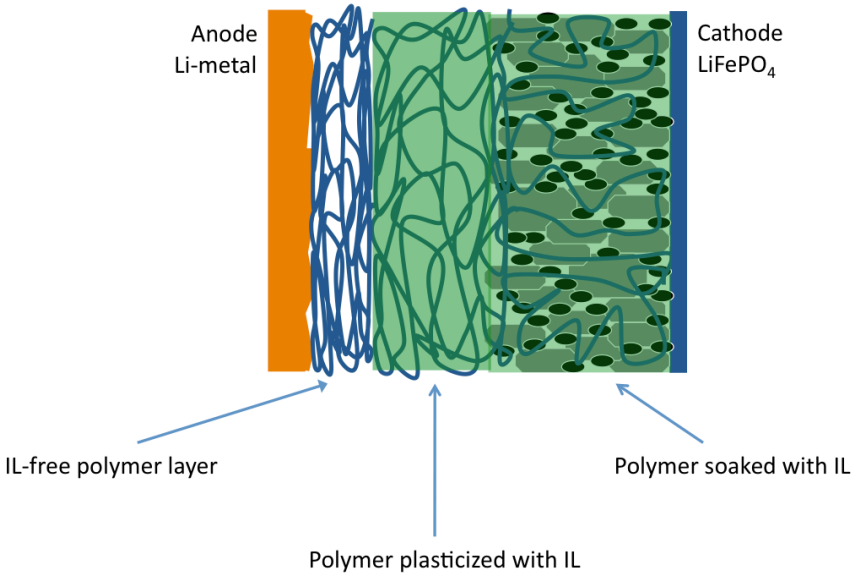

Figure 7.4 The dream battery, polymer ionic liquid (PIL) lithium battery

The PEGDME and ionic liquid mixture electrolyte (section 7.2) and better cathode-electrolyte wetting (section 7.4) allow the battery to be safe and have good performance. And the use of the GCE as the passivation film on lithium metal (section 7.3) allows lithium metal to be used as the anode without worrying about dendrite formation and gives the overall battery more than twice the energy density of a conventional lithium-ion battery. The ability to print the entire battery (section 7.5) allows the battery to be potentially manufactured at a low cost and into a high packing density form factor.

This dream battery can deliver four important value propositions: safety, wide temperature operation, high energy density, and low cost.

Contributions of Dissertation

The goal of this research was to study the solid polymer lithium battery, with emphasis on its performance at elevated temperatures and the phenomena occurring at its electrode-electrolyte interfaces. This has been accomplished using a combination of electrochemical, mass spectroscopy, and electron microscopy techniques.

Polymer Electrolyte

It has been demonstrated that the relationship between the polymer electrolyte conductivity and its segmental motion indeed agreed with the VTF equation. Based on the graft copolymer architecture, it was shown that POEA-g-PDMS has a T_g that is 5 °C lower than that of POEM-g-PDMS, and a conductivity that is 10 times higher, confirming that more flexible segmental motion translates to higher conductivity.

It has also been demonstrated that when doped with LiTFSI, the GCE (POEA-g-PDMS) has a conductivity of 10^{-4} S/cm at room temperature and more than 10^{-2} S/cm at 200 °C. In addition, DSC results showed that the salt predominantly interacted with the POEA domain.

Cathode-Electrolyte Interface

It has been demonstrated that by using the GCE as both the electrolyte and the cathode binder, the rate capability can be improved dramatically.

Full cells with $LiFePO_4$ as the cathode active materials and lithium metal as the anode were assembled and tested, and demonstrated good cycling and high specific capacity close to the practical value. A new doctor blading technique was developed to synthesize the cathode film such that the film did not delaminate from the aluminum current collector, and there was good contact at the solid electrolyte-solid electrode interfaces.

EIS was used to demonstrate that cells with higher conductivity binder (POEA-g-PDMS) had lower cathode-electrolyte interfacial impedance than with lower conductivity binder (POEM-g-PDMS). SEM and TEM were used to illustrate the surface coating of the $LiFePO_4$ particles by the GCE.

High Temperature Performance

The biggest contribution of the thesis is the demonstration of the performance of the solid polymer lithium battery from room temperature up to 200 °C, above the melting temperature of lithium metal. Before this work, the highest reported temperature for a rechargeable lithium battery was 120 °C, but this thesis demonstrated the passage of current between a solid polymer electrolyte and a liquid metal anode.

Both isothermal and thermal cycling under galvanostatic conditions up to 200 °C were demonstrated. TGA results demonstrated the isothermal stability of the GCE at elevated temperatures, despite minor bond cleavages associated with the backbone shown by FTIR results.

The rate capability of the entire battery was shown to improve dramatically at elevated temperatures. In fact, the rate capability of the GCE cells above 60 °C was comparable to that of the commercial liquid electrolyte LP30 cell at room temperature. Full cell EIS modeling was performed to study the various impedance contributors and their cycling and temperature dependences.

The ability of the solid polymer electrolyte to perform at elevated temperatures was demonstrated. While the reactivity of lithium metal and the instability of the passivation film at elevated temperatures limited the overall battery performance, the anode can be replaced with a more thermally stable material such as graphite or lithium alloy, it was not investigated here because it was not the goal.

Anode-Electrolyte Interface

EIS was performed on symmetric cells (Li/GCE/Li) to study the anode-electrolyte interfacial impedance and its dependence on high temperature cycling. It confirmed our earlier hypothesis that the fast capacity fade near the melting temperature of lithium was due to the reactivity of lithium metal and the disappearance of the passivation film.

The “Dream” Battery

A new electrolyte material consisting of solid polymer and ionic liquid, and a new battery design were proposed. This “dream” battery has the potential to maintain the safety and energy density advantages of the solid polymer lithium

battery and gain a power boost in its room temperature performance. This “dream” battery will transform the way people perceive rechargeable lithium batteries, and the solid polymer electrolyte will be a key enabler.

While the solid polymer lithium battery developed in this work was by no means a perfect battery, it served as a platform to understand the importance of the various components, and their effect on the battery impedance, cycle life, safety, energy density and performance. This understanding led to the ongoing pursuit of the “dream” battery. While the majority of the lithium battery community focuses on developing incrementally better cathode materials, the “dream” battery proposed in this thesis will cause a step function disruption. It is also adaptive and flexible enough that it will be relevant for as long as lithium battery remains relevant. With the worldwide growing consumerism and growing energy demand, portable and rechargeable lithium batteries will remain relevant for many years to come.

References

[1] P. G. Bruce *et al.*, Nature Materials **11** (2012).
[2] J. Tarascon, and M. Armand, Nature **414**, 359 (2001).
[3] B. Scrosati, J. Hassoun, and Y. Sun, Energy & Environment Science **4**, 3287 (2011).
[4] L. Ji *et al.*, Energy & Environment Science **4**, 2682 (2011).
[5] G. Jeong *et al.*, Energy & Environment Science **4**, 1986 (2011).
[6] J. B. Goodenough, and Y. Kim, Journal of Power Sources **196**, 6688 (2011).
[7] J. B. Goodenough, and Y. Kim, Chemistry of Materials **22**, 587 (2010).
[8] V. Etacheri *et al.*, Energy & Environment Science **4**, 3243 (2011).
[9] R. D. Deshpande *et al.*, Journal of the Electrochemical Society **158**, A845 (2011).
[10] M. Park *et al.*, Nano Letters **9**, 3844 (2009).
[11] L. Hu *et al.*, ACS Nano **4**, 5843 (2010).
[12] L. Hu, H. Wu, and Y. Cui, Applied Physics Letters **96**, 183502 (2010).
[13] L. Hu *et al.*, PNAS **106**, 21490 (2009).
[14] L. Cui *et al.*, Journal of the Electrochemical Society **158**, A592 (2011).
[15] C. Chan *et al.*, Journal of Power Sources **189**, 34 (2009).
[16] C. Chan *et al.*, Nature Nanotechnology **3**, 31 (2008).
[17] A. Armstrong *et al.*
[18] A. Hightower *et al.*, Applied Physics Letters **77**, 238 (2000).
[19] B. L. Ellis, K. Lee, and L. Nazar, Chemistry of Materials **22**, 691 (2010).
[20] J. W. Fergus, Journal of Power Sources **195**, 939 (2010).
[21] H. Zhou *et al.*, Chemical Materials **23**, 293 (2011).
[22] Q. Zhang *et al.*, Journal of the Electrochemical Society **158**, A443 (2011).
[23] A. Padhi, K. Nanjundaswamy, and J. B. Goodenough, Journal of the Electrochemical Society **144**, 1188 (1997).
[24] L. Yuan *et al.*, Energy & Environment Science **4**, 269 (2011).
[25] S. Chung, J. Bloking, and Y. Chiang, Nature Materials **1** (2002).
[26] K. Zaghib *et al.*, Electrochimica Acta **50**, 263 (2004).
[27] Y. Wang, P. He, and H. Zhou, Energy & Environment Science **4**, 805 (2010).
[28] P. G. Bruce, B. Scrosati, and J. Tarason, Angewandte Chemie **47**, 2930 (2008).
[29] N. Choi *et al.*, Journal of Materials Chemistry **21**, 9825 (2011).
[30] S. Chung, Y. Kim, and S. Choi, Advanced Functional Materials **20**, 4219 (2010).
[31] D. Aurbach *et al.*, Electrochimica Acta **45**, 1135 (1999).
[32] D. Aurbach, Mikhail D. Levi, and E. Levi, Solid State Ionics **179**, 742 (2008).
[33] D. Aurbach *et al.*, Journal of Power Sources **81-82**, 95 (1999).
[34] D. Aurbach *et al.*, Electrochimica Acta **45**, 67 (1999).
[35] O. Chusid *et al.*, Journal of Power Sources **97-98**, 632 (2001).
[36] P. Howlett *et al.*, Advanced Engineering Materials **11**, 1044 (2009).
[37] I. Ismail *et al.*, Electrochimica Acta **46**, 1595 (2001).
[38] R. Mason *et al.*, Solid State Ionics **118**, 129 (1999).
[39] N. Munishandraiah, L. G. Scanlon, and R. A. Marsh, Journal of Power Sources **72**, 203 (1998).
[40] E. Peled *et al.*, Electrochimica Acta **40**, 2197 (1995).

[41] G. Pistoia, A. Antonini, and G. Wang, Journal of Power Sources **58**, 139 (1995).
[42] C. Wessells *et al.*, Electrochemical and Solid-State Letters **13**, A59 (2010).
[43] G. B. Appetecchi *et al.*, Journal of Power Sources **196**, 6703 (2011).
[44] A. Guerfi *et al.*, Journal of Power Sources **175**, 866 (2008).
[45] M. Kunze *et al.*, Advanced Energy Materials **1**, 274 (2011).
[46] M. Nadherna *et al.*, Journal of Power Sources **196**, 7700 (2011).
[47] S. P. Ong *et al.*, Chemistry of Materials **23**, 2979 (2011).
[48] S. Seki *et al.*, Journal of the Electrochemical Society **154**, A173 (2007).
[49] A. Tsurumaki, J. Kagimoto, and H. Ohno, Polymer Advanced Technology **22**, 1223 (2011).
[50] J. Shin, W. A. Henderson, and S. Passerini, Journal of the Electrochemical Society **152**, A978 (2005).
[51] N. Kamaya *et al.*, Nature Materials **10**, 682 (2011).
[52] Z. Gadjourova *et al.*, Nature **412**, 520 (2001).
[53] F. Croce *et al.*, Nature **394**, 456 (1998).
[54] A. Christie *et al.*, nature **433**, 50 (2005).
[55] J. Chen *et al.*, Chemical Materials **19**, 3595 (2007).
[56] O. Buriez *et al.*, Journal of Power Sources **89**, 149 (2000).
[57] G. B. Appetecchi *et al.*, Journal of the Electrochemical Society **148**, A1171 (2001).
[58] K. M. Abraham, and Z. Jiang, Journal of Electrochemical Society **144**, L136 (1997).
[59] Y. Lin *et al.*, Nature **434**, 55 (2005).
[60] G. Mao *et al.*, Nature **405**, 163 (2000).
[61] B. Sandner *et al.*, Polymer Bulletin **28**, 355 (1992).
[62] P. P. Soo *et al.*, Journal of the Electrochemical Society **146**, 32 (1999).
[63] W.-S. Young, and T. H. Epps, Macromolecules **42**, 2672 (2009).
[64] Z. Zhang *et al.*, Macromolecules **36**, 9176 (2003).
[65] M. Yoshizawa *et al.*, Solid State Ionics **154-155**, 779 (2002).
[66] H. Wu, and C. D. Wick, Macromolecules **43**, 3502 (2010).
[67] C. Walker, and M. Salomon, Journal of Electrochemical Society **140**, 3409 (1993).
[68] C. Daniels, and J. Besenhard, Handbook of Battery Materials (2011).
[69] A. J. Bard, and L. R. Faulkner, ELECTROCHEMICAL METHODS (2001).
[70] J. Newman, and K. Thomas-Alyea, Electrochemical Systems (2004).
[71] C. Zu, and H. Li, Energy & Environment Science **4**, 2614 (2011).
[72] P. Balbuena, and Y. Wang, Lithium-ion Batteries: Solid-Electrolyte Interphase (2004).
[73] G. B. Appetecchi, S. Scaccia, and S. Passerini, Journal of the Electrochemical Society **147**, 4448 (2000).
[74] P. G. Bruce, and F. Krok, Solid State Ionics **36**, 171 (1989).
[75] R. Huggins, Energy Storage (2010).
[76] S. Lee *et al.*, Chemistry of Materials **23**, 2685 (2011).
[77] P. Lightfoot, M. A. Mehta, and P. G. Bruce, Science **262**, 883 (1993).
[78] J. B. Kerr *et al.*, Electrochimica Acta **48**, 2305 (2003).

[79] R. Bouchet, S. Lascaud, and M. Rosso, Journal of the Electrochemical Society **150**, A1385 (2003).
[80] S. C. Mui *et al.*, Journal of the Electrochemical Society **149**, A1610 (2002).
[81] P. Reale, S. Panero, and B. Scrosati, Journal of the Electrochemical Society **152**, A1949 (2005).
[82] P. Sakellariou, M. H. Abraham, and G. S. Whiting, Colloid Polymer Science **272**, 872 (1994).
[83] T. Shodai *et al.*, Journal of Electrochemical Society **141**, 2978 (1994).
[84] P. G. Bruce, Solid State Electrochemistry (1997).
[85] G. Nazri, and G. Pistoia, Lithium Batteries: Science and Technology (2009).
[86] C. Zhang *et al.*, Nature Materials **8**, 580 (2009).
[87] G. S. Fulcher, Journal of American Chemical Society **8**, 339 (1025).
[88] H. Vogel, Physics. Z **22**, 645 (1921).
[89] G. Tammann, and G. Hesse, Z. Anorg. Allg. Chem. **156**, 245 (1926).
[90] R. C. Agrawal, and G. P. Pandey, Journal of Physics D: Applied Physics **41**, 1 (2008).
[91] M. A. Hickner, Materials Today **13**, 34 (2010).
[92] A. Ghosh, Journal of the Electrochemical Society **157**, A846 (2010).
[93] E. A. Olivetti *et al.*, Chemical Materials **18**, 2828 (2006).
[94] D. R. Sadoway, Journal of Power Sources **129**, 1 (2004).
[95] D. R. Sadoway *et al.*, Journal of Power Sources **97-98**, 621 (2001).
[96] P. E. Trapa *et al.*, Journal of the Electrochemical Society **153**, A1098 (2006).
[97] P. E. Trapa *et al.*, Journal of the Electrochemical Society **152**, A1 (2005).
[98] R. B. Michnick, K. G. Rhoads, and D. R. Sadoway, Journal of the Electrochemical Society **144**, 2392 (1997).
[99] M. Orazem, and B. Tribollet, (2008).
[100] S. Analytical, An Introduction to Electrochemical Impedance Measurement
[101] M. Marzantowiz, J. R. Dygas, and F. Krok, Electrochimica Acta **53**, 7417 (2008).
[102] P. L. Moss *et al.*, Journal of Power Sources **189**, 66 (2009).
[103] Q. Hu *et al.*, Journal of Power Sources **196**, 5604 (2011).
[104] C. Delmas *et al.*, Nature Materials **7**, 665 (2008).
[105] K. Hanai *et al.*, Journal of Power Sources **196**, 6756 (2011).
[106] L. Laffont *et al.*, Chemical Materials **18**, 5520 (2006).
[107] R. Malik, F. Zhou, and G. Ceder, Nature materials **10**, 587 (2011).
[108] J. Wang, and X. Sun, Energy & Environment Science **5**, 5163 (2012).
[109] G. Chen, X. Song, and T. Richardson, Electrochemical and Solid-State Letters **9**, A295 (2006).
[110] C. Delacourt *et al.*, Electrochemical and Solid-State Letters **9**, A352 (2006).
[111] A. Fedrokova *et al.*, Journal of Power Sources **195**, 3907 (2010).
[112] L. Wang *et al.*, Physical Review B **76**, 165435 (2007).
[113] Y. Wang *et al.*, Angewandte Chemie **47**, 7461 (2008).
[114] K. Zaghib *et al.*, Journal of Power Sources **195**, 8280 (2010).
[115] A. Andersson *et al.*, Electrochemical and Solid-State Letters **3**, 66 (2000).
[116] B. Rao, B. Silbernagel, and J. Jacobson, Journal of Power Sources **3**, 59 (1978).

[117] T. Zheng, A. S. Gozdz, and G. G. Amatucci, Journal of the Electrochemical Society **146**, 4014 (1999).
[118] D. Munoz-Rojas *et al.*, Electrochemistry Communications **9**, 708 (2007).
[119] M. D. Levi *et al.*, Journal of Power Sources **119-121**, 538 (2003).
[120] T. Shodai *et al.*, Journal of Electrochemical Society **141**, 2978 (1994).
[121] S. J. Clarson, and J. A. Semlyen, Polymer **27**, 91 (1985).
[122] M. Jain *et al.*, Journal of the Electrochemical Society **146**, 4023 (1999).
[123] M. Ganesan, Electrochemistry Communications **9**, 1980 (2007).
[124] F. Mestre-Aizpurua *et al.*, Journal of Applied Electrochemistry **40**, 1365 (2010).
[125] D. Arumugam, and G. Kalaignan, Thin Solid Films **520**, 338 (2011).
[126] A. R. Polu, and R. Kumar, E-Journal of Chemistry **8**, 347 (2011).
[127] G. B. Appetecchi *et al.*, Journal of Electrochemical Society **145**, 4126 (1998).
[128] Z. Bakenov, M. Nakayama, and M. Wakihara, Electrochemical and Solid-State Letters **10**, A208 (2007).
[129] R. S. Baldwin, (2007).
[130] A. Selvaggi, F. Croce, and B. Srosati, Journal of Power Sources **32**, 389 (1990).
[131] C.-W. Wang, and A. M. Sastry, Journal of the Electrochemical Society **154**, A1035 (2007).
[132] A. Teyssot *et al.*, Solid State Ionics **177**, 141 (2006).
[133] H. H. Sumathipala *et al.*, Journal of Applied Electrochemistry **38**, 39 (2008).
[134] A. M. Stephan, and K. S. Nahm, Polymer **47**, 5952 (2006).
[135] C. A. C. Sequeira, and A. Hooper, Solid State Ionics **9 & 10**, 1131 (1983).
[136] P. P. Prosini *et al.*, Journal of Power Sources **99**, 1 (2001).
[137] S. Ong *et al.*, Electrochemistry Communications **12**, 427 (2010).
[138] D. Aurbach, and A. Zaban, Journal of Electroanalytical Chemistry **348**, 155 (1993).
[139] D. Aurbach, and A. Zaban, Journal of Electroanalytical Chemistry **367**, 15 (1994).
[140] P. Agarwal, and M. E. Orazem, Journal of the Electrochemical Society **139**, 1917 (1992).
[141] M. Hiratani, K. Miyauchi, and T. Kudo, Solid State Ionics **28-30**, 1431 (1988).
[142] M. E. Orazem, P. Aganval, and L. H. Garcia-Rubio, Journal of Electroanalytical Chemistry **378**, 51 (1994).
[143] S.S. Zhang, K. Xu, and T. R. Jow, Electrochimica Acta **51**, 1636 (2006).
[144] A. Zaban, E. Zinigrad, and D. Aurbach, Journal of Physical Chemistry **100**, 3089 (1996).
[145] M. Watanabe *et al.*, Journal of Power Sources **81-82**, 786 (1999).
[146] K. Abraham, and M. Alamgir, Chemistry of Materials **3**, 339 (1991).
[147] G. B. Appetecchi *et al.*, Journal of Power Sources **101**, 42 (2001).
[148] G. B. Appetecchi *et al.*, Journal of Power Sources **114**, 105 (2003).
[149] M. L. Granvalet-Mancini, and D. Teeters, Journal of Power Sources **97-98**, 624 (2001).
[150] J. B. Kerr, slides (2009).
[151] J. Lee *et al.*, Advanced Energy Materials **1**, 34 (2011).
[152] A. Lisowska-Oleksiak, Solid State Ionics **119**, 205 (1999).

[153] P. Novak, and P. Podhajecky, Journal of Power Sources **35**, 235 (1991).
[154] P. Ribiere *et al.*, Energy & Environment Science **5**, 5271 (2012).
[155] J. F. Snyder, R. H. Carter, and E. D. Wetzel, Chemical Materials **19**, 3793 (2007).
[156] S. Chaurasia, R. Singh, and S. Chandra, Solid State Ionics **183**, 32 (2011).
[157] J. Hallett, and T. Welton, Chemical Reviews **111**, 3508 (2011).
[158] W. Henderson, ILEET Presentation (2011).
[159] J. Shin, W. Henderson, and S. Passerini, Electrochemistry Communications **5**, 1016 (2003).
[160] T. Welton, Chemical Reviews **99**, 2071 (1999).
[161] H. Yang *et al.*, Electrochimica Acta **56**, 6271 (2011).
[162] H. Tokuda *et al.*, Journal of Physical Chemistry B **109**, 6103 (2005).